DOE/ER/45151--T1

DOE/ER/45151--T1

DE93 001701

Final Report

"Microscopic Physical and Chemical Properties of Graphite Intercalation Compounds"

Submitted to:

United States Department of Energy

Office of Basic Energy Sciences

for the period 8/1/84 to 7/31/85

Grant # DE-FG05-84ER45151

DISCLAIMER

This report was prepared as an account of work sponsored by an agency of the United States Government. Neither the United States Government nor any agency thereof, nor any of their employees, makes any warranty, express or implied, or assumes any legal liability or responsibility for the accuracy, completeness, or usefulness of any information, apparatus, product, or process disclosed, or represents that its use would not infringe privately owned rights. Reference herein to any specific commercial product, process, or service by trade name, trademark, manufacturer, or otherwise does not necessarily constitute or imply its endorsement, recommendation, or favoring by the United States Government or any agency thereof. The views and opinions of authors expressed herein do not necessarily state or reflect those of the United States Government or any agency thereof.

Prepared by: Peter C. Eklund Date 24 Aug. 1992

Professor Peter C. Eklund
Department of Physics and Astronomy
University of Kentucky
Lexington, KY 40506

MASTER

DISTRIBUTION OF THIS DOCUMENT IS UNLIMITED

Overview

The following report summarizes our activity in DOE grant # DE-FG05-84ER45151, "Microscopic Physical and Chemical Properties of Graphite Intercalation Compounds" for the period 8/1/84 to 7/31/85. Optical spectroscopy (Raman, FTIR and Reflection) was used to study a variety of acceptor- and donor-type compounds synthesized in out laboratory to determine the microscopic models consistent with the spectrocsopic results.

The general finding here is that the electrical conduction properties of these compounds can be understood on the basis that the intercalation of atomic and/or molecular species between the host graphite layers either raises or lowers the Fermi level (E_F) in a graphitic band structure. This movement of E_F is accomplished via a charge transfer of electrons from the intercalate layers to the graphitic layers (donor compounds), or vice versa (acceptor compounds). Furthermore, the band structure must be modified to take into account the layers of charge that occur as a result of the charge transfer. This charge layering introduces additional bands of states near E_F, which we discuss below. Charge-transfer also induces a perturbation of the graphitic normal mode frequencies which can be understood as the result of a contraction (acceptor compounds) or expansion (donor compounds) of the intralayer C-C bonds. Ab-initio calculations support this view and are in reasonable agreement with the experimental data.

Effects of Charge Transfer on the Optical Properties of Graphite Intercalation Compounds

In this chapter, we review the effects of charge transfer on the optical properties of graphite intercalation compounds (GICs) [4.1]. The principal optical techniques used to study charge transfer and its effects on the electronic and phonon properties of GICs have been reflectance spectroscopy and Raman scattering. Several reviews of Raman scattering [4.2] and the optical properties [4.3, 4] of GICs have appeared in the past few years.

Graphite intercalation compounds are quasi-two-dimensional metals whose highly anisotropic electrical and thermal properties stem from the anisotropic properties of graphite itself. Pristine graphite is a semimetal with small hole and electron pockets that lie along the H-K-H axes in the six corners of a hexagonal Brillouin zone [4.1]. The intercalation of foreign atoms or molecules to form a stage-n compound, where n refers to the number of carbon (C) layers between periodically placed intercalate (I) layers, is accompanied by a substantial transfer of charge between these two types of layers, leaving the hexagonal intralayer arrangement of the carbon atoms intact. With increasing charge transferred to the C layers, the small electron and hole pockets found in pristine graphite evolve into larger cylinders that eventually exhibit trigonal warping. The cylindrical surfaces of a low charge transfer stage-2 GIC are shown schematically in Fig. 4.1.

Of course, charge neutrality demands that an equal and opposite net charge resides in the C and I layers. For stage $n > 2$ compounds, two types of C layers are possible: C layers that lie adjacent to an intercalant layer, termed bounding carbon layers (C_b), and C layers that lie between other C layers, termed interior carbon layers (C_i). Experiment and theory have shown that most of the net layer charge in the C layers resides in the C_b layers. This uneven c-axis distribution of layer charge removes degeneracies in the graphitic intralayer phonons, and new "interior" and "bounding" layer mode frequencies are observed [4.1, 2]. Furthermore, the uneven net layer charge distribution results in n conduction and n valence graphitic π bands in a stage n compound [4.1–4]. Optical data can be used with other experimental results – (e.g., Shubnikov de Haas (SdH), nuclear magnetic resonance (NMR), Pauli spin susceptibility) – to determine parameter values for electron energy band models. Once the parameter values are known, the net layer charge on the C_i and C_b layers can then be evaluated from the band models.

If electrons are "donated" by the I layers to the C layers, the Fermi level, E_F, is raised in the carbon p_z (or π) bands, and the GIC is termed a "donor-type"

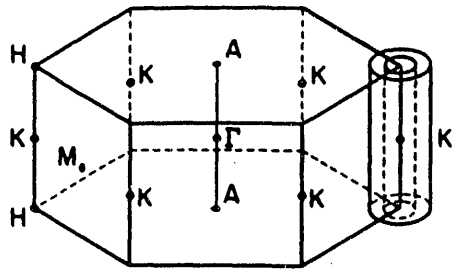

Fig. 4.1. Graphitic Brillouin zone: concentric cylinders represent the Fermi surface of a stage-2 GIC at low charge transfer

compound. If, on the other hand, electrons are transferred from the C layers and "accepted" by the I layers, an "acceptor"-type GIC is formed. X-ray and neutron scattering experiments have shown directly that increasing charge transfer is accompanied by a measurable expansion (donor-type GICs) or contraction (acceptor-type GICs) in the in-plane C–C bond length, as well as a contraction in the thickness of the three-layer C_b–I–C_b sandwich.

In Sect. 4.1 we discuss experimental considerations pertinent to Raman scattering and reflectance spectroscopy in GICs, and describe the safe handling of air-sensitive samples for optical study. In Sect. 4.2 we indicate the relationship between the optical reflectance, the dielectric constant, and the electron energy band structure in GICs. We discuss the process for the Kramers-Kronig determination of the GIC (basal plane) dielectric function using "density-scaled graphite". In Sect. 4.3 we review results of optical studies on donor and acceptor (binary and ternary) GICs that have led to values for the charge transferred to the carbon layers, or the effects of charge transfer on the optical-phonon frequencies. Finally, in Sect. 4.4 we present a summary of the optical determination of charge transfer, and offer directions for future research.

4.1 Experimental Considerations

4.1.1 Optical Measurement of Air-Sensitive Compounds

Most GICs are moderately to very air sensitive, although there are a few noteworthy exceptions (i.e., graphite-$SbCl_5$ [4.5], graphite-$CsBi_x$ [4.6], and graphite-F [4.7]). Therefore, for most GICs, considerable care is required in handling samples to prevent changes in composition before the actual measurements. This is particularly true when carrying out short-probe-depth experiments. Almost all the optical data presented here were taken on the *c* face of the GIC, where a typical skin depth for the incident radiation is $\sim$ 1000 Å. Changes in composition at this depth can occur, in some cases, in a matter of seconds under ambient conditions. In this section we discuss briefly methods for handling samples before optical measurement. Various methods to prepare GICs have been reviewed by *Hérold* [4.8a] and *Eklund* [4.8b].

Often the best way to obtain the optical spectrum of an air-sensitive GIC is to do so without removing the sample from the intercalation chamber (or

reactor). If this approach is chosen, care must be taken during synthesis not to precipitate, sublime, or condense reactant onto the sample surface. This can occur, for example, in a two-zone reaction [4.8] when the zone temperatures of the sample (T_s) and the reactant (T_r) are such that $T_s \leqslant T_r$. Caution must also be taken to ensure that the optical window is not clouded by the intercalation reaction.

Quartz or Pyrex windows – the latter being sufficient for Raman scattering, and the former for reflectance studies over the range 0.5–6 eV – can be fused onto glass reactors. Figure 4.2 shows a convenient optical cell used for both reflectance and Raman scattering. It employs quartz or Pyrex rectangular cross-section glass tubing near the sample (7 × 3 mm inside dimensions, 1/2 mm wall). The sample shown in the figure is a $\sim 6 \times 8 \times 0.5$ mm^3 slab of synthetic, highly oriented pyrolitic graphite (HOPG; Union Carbide). The slab is cut to fit in the diagonal of the tubing as shown, and stainless steel clips can also be used to keep the sample from shifting. A constriction is shown at "C" about 4–5 cm from the sample. It can be sealed off with a torch, thereby separating a small, sealed cell for experiments. If low-temperature measurements are necessary, He gas can be diffused through the walls of this cell (after sealing it off) to promote heat transfer between the sample and cell walls.

If it is necessary to transfer a GIC from the reactor to a different cell for optical study, this should be done under vacuum or in a very dry, inert-atmosphere glove box. Even in a fairly dry ($\sim$ 5–10 ppm O_2/H_2O) He-atmosphere glove box, a gold-colored stage-1 alkali-metal GIC turns blue in several seconds, indicating the formation of stage-2 or higher compounds in the optical skin depth. These GICs are perhaps best transferred under vacuum. We have sometimes used a small vacuum chamber, equipped with a hammer to break open glass reaction ampoules, and transferred very sensitive samples under

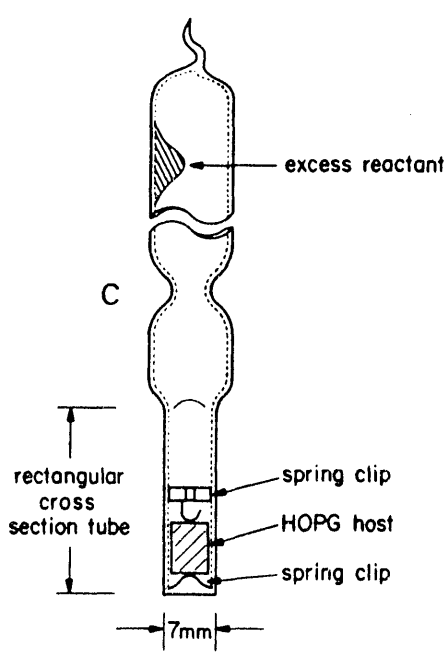

Fig. 4.2. Glass cell suitable for optical studies of air-sensitive GICs

vacuum to a second glass ampoule that could then be sealed with a torch and used as an optical cell.

However, not all GICs need to be handled this carefully. Stage-2 alkali-metal GICs, for example, have been found to transfer quite well in a dry (< 5 ppm O_2/H_2O) He glove box. For mid-infrared optical measurements (2–15 microns) requiring salt or sapphire windows, we have transferred GIC samples in a He glove box to a small, stainless-steel optical cell equipped with a 3/4 l/s ion pump and valve. The cell is removed and evacuated on a diffusion pump station. The ion pump is then started and maintains a vacuum of 10^{-5}–10^{-6} Torr.

Usually it is important to determine the stage index of the sample under optical study. Traditionally, the stage index is determined from (001) X-ray diffraction. Mo K_α radiation easily penetrates 0.5 mm thick glass ampoule walls. The X-ray probe depth is $\sim$ 20–50 microns, which is much larger than the optical skin depth. Several samples are usually studied to ensure that the optical spectrum is properly identified with the correct stage index.

Raman scattering experiments probe approximately the same depth as reflectance measurements. Thus the same care used in handling samples for reflectance studies is needed in Raman scattering experiments. However, Raman scattering studies benefit from the fact that the Raman-active carbon intralayer phonons are stage-specific [4.2]. Raman scattering has, therefore, become a commonly used tool for determining the stage index of samples studied in reflectance. The technique is particularly useful in identifying low-stage-index $n \leqslant 3$ compounds, where the stage dependence of the graphitic intralayer $\sim 1600\ \mathrm{cm}^{-1}$ phonons is the strongest [4.1.2].

4.1.2 Optical Reflectance Spectroscopy

Reflectance spectra with the radiation incident at near-normal incidence to the c axis have been used with electron energy band models to determine the in-plane dielectric function, the charge transfer between C and I layers, and the distribution of net c-axis charge among the C_i and C_b layers. Most optical studies have been made on samples prepared from HOPG [4.9] – a polycrystalline synthetic graphite – because large samples with reasonably smooth surfaces can be obtained (typical dimensions $5 \times 5 \times 1\ \mathrm{mm}^3$). The c axes of the $\sim 1\ \mu\mathrm{m}$ diameter crystallites in HOPG are aligned to better than 1 degree, so it is a suitable host for basal (a-b) plane (or c-face) optical studies of GICs. HOPG can be readily cleaved parallel to the basal plane using transparent tape. With some difficulty, a faces can be prepared [4.10] by careful polishing, followed by ion sputtering of the polished surface to remove surface damage. The HOPG host may then be reacted to study the c-axis dielectric constant. Only a few such studies have been carried out to date. Thin single crystals of graphite are also available, but they are small (typically $\sim 1 \times 1\ \mathrm{mm}^2$), and difficult to hold in place in the optical cell.

Care must be taken to collect most, if not all, of the light reflected from the GIC, if quantitative reflectance results are required. Generally speaking, the effect of surface roughness (incurred during GIC synthesis) on the optical

spectrum can be accounted for, if necessary, by multiplying R by a wavelength independent scale factor $\beta \sim 1$. This procedure is possible because the surface roughness usually has a scale that is large compared with the wavelength of the incident light. However, the reflectance spectrum (i.e., $R \rightarrow \beta R$) should be scaled carefully and, in connection with the Drude analysis of the reflectance spectrum, an additional fitting parameter β is introduced to the three (ε_∞, ω_p, τ; Sect. 4.2.1) normally used in this analysis. Other forms of graphite, such as Grafoil (Union Carbide) exhibit a surface roughness on a shorter length scale, which introduces a wavelength-dependent correction factor to R (Sect. 4.3.1b).

4.1.3 Raman Spectroscopy

For the most part, c-face Raman scattering studies of GICs have been carried out to obtain information about the intercalate-perturbed modes involving intralayer displacement of the carbon atoms [4.1.2]. Only in a few cases have intercalant modes been observed, and probably their detection resulted from a resonantly enhanced scattering cross section. The difficulty in seeing the potentially very interesting intercalate modes stems from both the 1000 Å skin depth that reduces the size of the scattering volume, and the fact that the intercalated atoms or molecules are diluted in concentration by the carbon layers. A few Raman scattering studies have been reported with the laser radiation incident on an a face of the GIC, where the a face was prepared by tearing open HOPG under tension applied parallel to the basal plane [4.11]. The a face affords the possibility of studying interlayer modes, when the radiation is polarized parallel to the c axis.

Raman scattering on opaque materials in general, and on GICs in particular, can best be carried out in the Brewster-angle backscattering geometry [4.2]. For c-face studies, the incident beam strikes the c face of the GIC at an angle $\sim 45°$ with respect to the c axis, with the electric field polarized in the plane of incidence. This angle is close enough to the pseudo Brewster angle to approximately minimize the reflection coefficient for the incident radiation. The Raman scattered light is collected at normal incidence to the c face.

GICs have been found to decompose or change stage during Raman scattering experiments because of laser heating. Low powers ($\sim$ 100 mW or less) and a cylindrical lens are therefore used to reduce the power density on the sample.

4.2 Deducing Charge Transfer from Optical Studies

4.2.1 The Relationship Between the Optical Reflectance, Dielectric Function, and Electronic Band Structure of GICs

Most reflectance studies on GICs have been carried out at near-normal incidence to the c face. The quantity measured is the intensity ratio $R = |E_r/E_i|^2$, where E_i and E_r are the incident and reflected electric fields perpendicular to the

c axis. Then $R(\omega)$ is governed by the basal (i.e., a-b) plane dielectric function $\varepsilon_\perp$, which is related to the reflectivity r by the usual expression [Ref. 4.12, p. 232]

$$r = \frac{E_r}{E_i} = \varrho e^{i\theta} = \frac{1 - \sqrt{\varepsilon_\perp}}{1 + \sqrt{\varepsilon_\perp}}, \tag{4.1}$$

where ϱ and θ are the reflectivity amplitude and phase shift, respectively.

In a solid, the dielectric function $\varepsilon(\omega) = \varepsilon_1(\omega) + i\varepsilon_2(\omega)$ can be represented as a sum of three terms:

$$\varepsilon(\omega) = \varepsilon_{\text{free}}(\omega) + \varepsilon_{\text{inter}}(\omega) + \varepsilon_{\text{phonon}}(\omega), \tag{4.2}$$

where $\varepsilon_{\text{free}}(\omega)$, $\varepsilon_{\text{inter}}(\omega)$, and $\varepsilon_{\text{phonon}}(\omega)$ refer to contributions from free carriers, interband transitions, and infrared-active phonons. The real and imaginary parts of $\varepsilon(\omega)$ are associated with dispersion and absorption, respectively. In the Drude approximation, the free-carrier term is written as [Ref. 4.12, p. 53].

$$\varepsilon_{\text{free}}(\omega) = \varepsilon_\infty - \frac{\omega_p^2}{\omega(\omega + i/\tau)}, \tag{4.3}$$

where ε_∞, ω_p, and τ are, respectively, the core dielectric constant, plasma frequency, and carrier lifetime. The interband contribution from vertical (i.e., k-conserving transitions is given by [4.12, p. 114]

$$\varepsilon_{\text{inter}}(\omega) = \frac{e^2h^2}{m^2\omega^2} \int_s \frac{|\boldsymbol{n} \cdot \boldsymbol{M}_{ss'}(\boldsymbol{k})|}{|\nabla_k [E_{s'}(\boldsymbol{k}) - E_s(\boldsymbol{k})]|} \, dS . \tag{4.4}$$

The integration is over the k-space surface $S(\boldsymbol{n} \perp S)$ defined by $\{E_{s'}(\boldsymbol{k}) - E_s(\boldsymbol{k})\} = \hbar\omega$, where ω is the photon frequency.

In a stage-n GIC, the low-energy ($\omega < 3$ eV) interband transitions between valence (v or π) and conduction (c or π^*) bands are of two principal types: $v \to v$ and $v \to c$. These bands are centered at the K point and are shown schematically in Fig. 4.3a, b for stage-1 and stage-2 donor compounds; k represents the in-plane wave vector measured relative to the K point (Fig. 4.1) in a graphitic

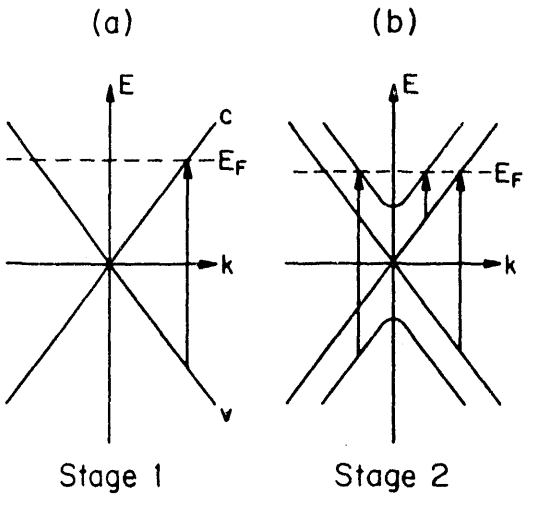

Fig. 4.3. Stage-1(**a**) and stage-2(**b**) energy bands near the K point in a graphitic Brillouin zone. The radial wave vector k is measured from the K point and refers to the momentum in the basal plane

Brillouin zone. The vertical arrows in the figure indicate the strongest interband transitions, as first found by *Blinowski* et al. [4.13]. Structure in the optical spectrum of stage $n > 1$ GICs associated with $v \rightarrow v$ transitions (acceptor-type) or $c \rightarrow c$ transitions (donor-type) have been found to be reasonably sharp, indicating that these energy bands are nearly parallel over a considerable volume of k space. In the case illustrated in the figure, $v \rightarrow c$ absorption exhibits a threshold energy $E_T \sim 2E_F$; i.e., the strongest transitions occur between bands of near mirror symmetry [4.13]. Figure 4.1 shows a schematic two-dimensional Fermi surface for the stage-2 π-band model of Fig. 4.3b. A pair of concentric cylinders is located at each K point, with the cylinder axes parallel to the c axis. For large enough charge transfer, the cylinders will eventually exhibit trigonal warping [4.4]. The π- or π^*-band contribution to $\varepsilon_{\text{free}}(\omega)$ comes from the response of graphitic carriers in these cylinders – which are two-dimensional holes (electrons) in acceptor-type (donor-type) compounds. However, other carrier pockets may also contribute to the free-carrier response. For example, in stage-1 binary donor GICs (Sect. 4.3.1a), a three-dimensional piece of the Fermi surface located at the Γ point has also been proposed to contribute to $\varepsilon_{\text{free}}(\omega)$.

The principal contribution to $\varepsilon_{\text{phonon}}(\omega)$ in GICs is from zone-center transverse-optical (TO) phonons whose contribution can be represented by a sum of Lorentz oscillators [4.14]:

$$\varepsilon_{\text{phonon}}(\omega) = \sum_{j=1}^{N} \frac{\Omega_j^2}{(\omega_{\text{TO},j}^2 - \omega^2) - i\gamma_j\omega} , \tag{4.5}$$

where $\omega_{\text{TO},j}$, γ_j, and Ω_j are the frequency, damping, and strength of the jth TO ($q = 0$) phonon.

To determine the values of the parameters included in the model dielectric function (4.2–5), we can either fit a reflectance calculated from a model dielectric function to the R data or fit the model dielectric function itself directly to $\varepsilon_1, \varepsilon_2$ data obtained from a Kramers-Kronig (KK) analysis of the R data. In a KK analysis, the reflectivity phase shift θ is calculated, and (4.1) is inverted to obtain the experimental values for $\varepsilon_1, \varepsilon_2$. The KK phase integral is given by the usual expression [4.15]

$$\theta = -\frac{\omega}{\pi} \mathscr{P} \int_0^\infty \frac{\ln[R(\omega')/R(\omega)]}{\omega'^2 - \omega^2} d\omega' , \tag{4.6}$$

where $\mathscr{P}$ denotes the principal value. Although the $R(\omega)$ data is obtained in a limited frequency range, the phase θ may still be calculated approximately by extrapolating the reflectance to higher and lower frequencies. Consistent with the metallic character of GICs, $R(\omega)$ is extended to lower frequencies according to the Drude model (4.3). For frequencies $\omega > 8$ eV, an approximate reflectance for the GIC can be generated according to the model dielectric function given by *Eklund* et al. [4.4]:

$$\varepsilon_{\text{DSG}}(\omega) = 1 + \frac{3.35n}{l_c(\text{Å})} [\varepsilon_G(\omega) - 1] , \tag{4.7}$$

where ε_G is the experimental, in-plane dielectric function of pristine graphite obtained by *Taft* and *Phillip* [4.16], n is the stage index, l_c is the spacing between successive intercalate layers, and 3.35 Å is the distance between C layers in graphite. The physical basis for this approximation to the high-energy dielectric function of a GIC, referred to as "density-scaled graphite" (DSG) [4.4], is summarized by three key points:

(1) The GIC is mostly graphitic carbon.

(2) For $\omega > 8$ eV, $\varepsilon_G(\omega)$ is dominated by the contribution from σ electrons.

(3) The character of the σ band is determined primarily by very strong C–C intralayer interactions (i.e., σ bonds) that are largely unaffected by intercalation (i.e., the hexagonal C network is preserved).

Thus the high frequency $\varepsilon(\omega)$ for the GIC should be similar to $\varepsilon_G(\omega)$, but scaled according to the number of carbon layers per unit distance along the c axis of the GIC.

For comparison, Fig. 4.4 shows $\varepsilon_2(\omega)$ data for LiC_6, KC_8, and $KHgC_4$ (solid lines) calculated according to the DSG model (dotted line) by *Fischer* et al. [4.17]. Above 8 eV, the agreement between the DSG appproximation and the data is good. Note, however, that the peak at ~ 5 eV in these donor compounds, associated with transitions between π bands near the M point in a graphitic Brillouin zone, is not well described by the DSG model. This disagreement near 5 eV indicates intercalate-induced changes in π-band dispersion near the M point – i.e., π-band hybridization with intercalate states – and/or an intercalate layer contribution to ε_{inter} in this frequency range.

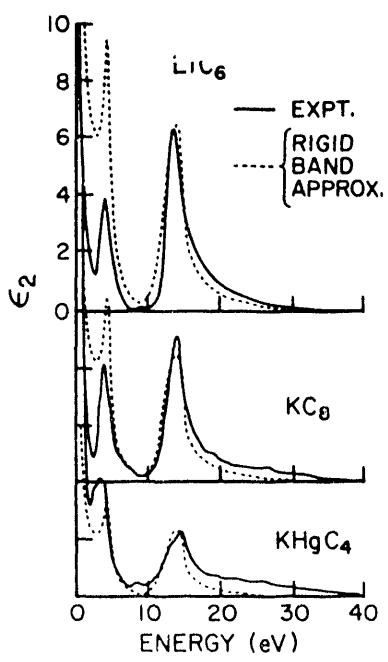

Fig. 4.4. Kramers-Kronig derived values of $\varepsilon_2(\omega)$ for LiC_6, KC_8, and $KHgC_4$ (solid line). The dashed lines represent values calculated according to (4.7) [4.17]

4.2.2 Electronic Band Structure Models

In chap. 2 *Holzwarth* reviews in detail electron energy band calculations in GICs. In the following three sections, we briefly discuss three models that have been used to analyze quantitatively charge transfer and the dielectric response of GICs.

(a) The *K*-Point Tight-Binding Model of Blinowski and Rigaux

Blinowski et al. [4.13] developed an early tight-binding band model (referred to here as the BR model) for stage-1 and stage-2 GICs that has been used extensively for the analysis of electrical transport, magnetic susceptibility, NMR, and optical data. Using proper values for the model band parameters (γ_0 and γ_1), good agreement with optical data can be obtained, provided the charge transfer is not too high. In the BR model, an n-stage compound is viewed as a collection of uncoupled subsystems consisting of n graphite layers bounded by intercalate (I) layers, where the I layers are viewed as a structureless, uniformly charged sheet. The BR model does not consider C-layer interaction across an I layer, and thus it is two dimensional. Considering the lowest order intralayer (γ_0) and interlayer (γ_1) C–C transfer integrals, *Blinowski* et al. [4.13] obtained analytic expressions for the stage-1 and stage-2 π-band dispersion near the K point (Figs. 3a, b) in a graphitic Brillouin zone. Because of the relatively simple analytic form obtained for the band dispersion, which stems from ignoring all higher-order C–C transfer integrals, useful analytic expressions can be derived for many physical quantities. In the BR model, the carbon π-band dispersion is given in terms of the nearest-neighbor C–C intralayer (γ_0) and interlayer (γ_1) transfer integrals by [4.13]

$$\text{Stage 1:} \quad E(k) = \pm \tfrac{3}{2}\gamma_0 bk \,, \tag{4.8a}$$

$$\text{Stage 2:} \quad E(k) = \pm \tfrac{1}{2}[\gamma_1 \pm (\gamma_1^2 + 9\gamma_0^2 b^2 k^2)^{1/2}] \,, \tag{4.8b}$$

where the wave vector k is measured relative to the K point, and $b = 1.42$ Å is the intralayer C–C distance. The BR model neglects longer range C–C transfer integrals. Most optical studies of GICs seem to indicate that the BR model parameters should be $\gamma_1 \approx 0.38$ eV and $\gamma_0 \approx 2.8 - 3.0$ eV. We discuss the experimental determination of these values later.

Several other important expressions useful to our purposes here follow from the BR model. For example, charge transfer f_C and the position of the Fermi level E_F are related by

$$\text{Stages 1 and 2:} \quad E_F = \gamma_0 \sqrt{\pi f_C \sqrt{3}} \,, \tag{4.9}$$

where f_C is the net charge per C atom in units of electrons (e) per C atom. Note that the stage-2 relation between f_C and E_F given in the original work [4.13] is incorrect. The "bare" or "unscreened" plasma frequency ω_p in the Drude expression (4.3) is related to the free-carrier concentration N by

$$\omega_p^2 = 4\pi N e^2/m^* \,, \tag{4.10}$$

where m^* refers to the optical mass, and represents the average band mass – i.e., $h^2(\partial^2 E/\partial k^2)^{-1}$ averaged over occupied states. The bare plasma frequency ω_p should not be confused with the screened plasma frequency ω_p^*. In the Drude model, $\omega_p^* = \omega_p/\sqrt{\varepsilon_\infty}$. The screened plasma frequency is usually identified with the lowest energy zero crossing for $\varepsilon_1(\omega)$. Note that ω_p^* is close to the position of the "Drude edge" in $R(\omega)$, where by "Drude edge" we mean the portion of the reflectance curve associated with the rapid decline in reflectance from high values in the infrared region to quite low values (in some cases as low as 1–2%). Calculation of the plasma frequency using the BR-model band dispersion equations (4.8a, b) results in the following dependence on the Fermi energy [4.13]:

$$\text{Stage 1:} \quad \omega_p^2 = \frac{4e^2}{h^2 l_c} E_F \,, \tag{4.11a}$$

$$\text{Stage 2:} \quad \omega_p^2 = \frac{8e^2 E_F}{h^2 l_c}\left(\frac{E_F^2 - \gamma_1^2/2}{E_F^2 - \gamma_1^2/4}\right), \tag{4.11b}$$

where l_c refers to the distance between intercalate layers, and differs in meaning from the same quantity used by *Blinowski* et al. [4.13]. A typical value for the stage-1 graphitic carrier optical mass m^* can be obtained with (4.9, 10, 11a). Using the values $E_F = 0.8$ eV, $\gamma_0 = 3$ eV, and $l_c = 10$Å, we obtain $m^*/m_0 = 0.2$, where m_0 is the free-electron mass. This light carrier mass is responsible for the high in-plane electrical conductivity observed in GICs, despite the fact that the carrier density N is at least a factor of 10 lower than in Cu.

(b) LCAO Model of Holzwarth

Holzwarth [4.18] has considered a π-band model for a stage-n GIC using the method of linear combination of atomic orbitals (LCAO) as developed by *Johnson* and *Dresselhaus* for graphite [4.19]. The assumptions of the *Holzwarth* model (or "H model") regarding the carbon bands in the GIC are similar to those of the BR model discussed above; i.e., the π bands are only weakly perturbed by the insertion of the I layers, and the C layers on either side of an I layer are not coupled (i.e., the model is two dimensional). For stage $n > 2$, the H model does not consider the effects of the I-layer charge on the net C-layer charge in the C_i and C_b layers. Later theoretical work (Chap. 2) has shown these c-axis electrostatic effects to be important: they give rise to charge in the graphitic layers residing primarily in the C_b layers. For stage $n \leqslant 2$, the H and BR models should provide a reasonable description of the carbon π-band contribution to the electronic properties of GICs; the former being more appropriate for higher charge transfer compounds. However, *Holzwarth* [4.18] gives the numerical results for stage-1 compounds only.

The quantitative differences between these two models stem from the neglect in the BR model of more distant intralayer C–C interactions. For increasing Fermi wave vector k_F (measured relative to the K point), the higher-order

interactions considered in the H model (and neglected in the BR model) eventually introduce trigonal warping of the cylindrical Fermi surfaces, and destroy the exact mirror symmetry between the valence (π) and conduction (π^*) bands. *Zhang* et al. [4.20, 21] have considered the differences in the H and BR models that affect the determination of f_c from the π-electron plasma frequency $\omega_{p,\pi}$. Figures 4.5, 6 summarize the H and BR model results for stage 1 GICs. The

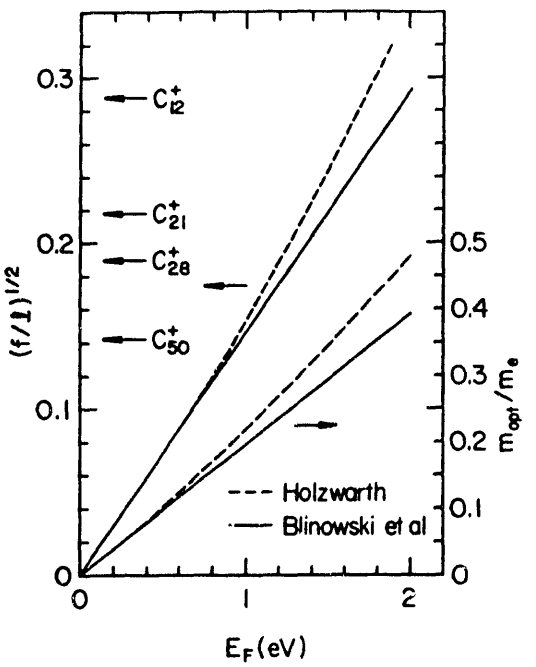

Fig. 4.5. Comparison of results for the stage-1 Holzwarth and Blinowski-Rigaux models for acceptor-type GICs. The quantity (f/l) is equivalent to f_c in the text (γ_0 = 2.9 eV) [4.20]

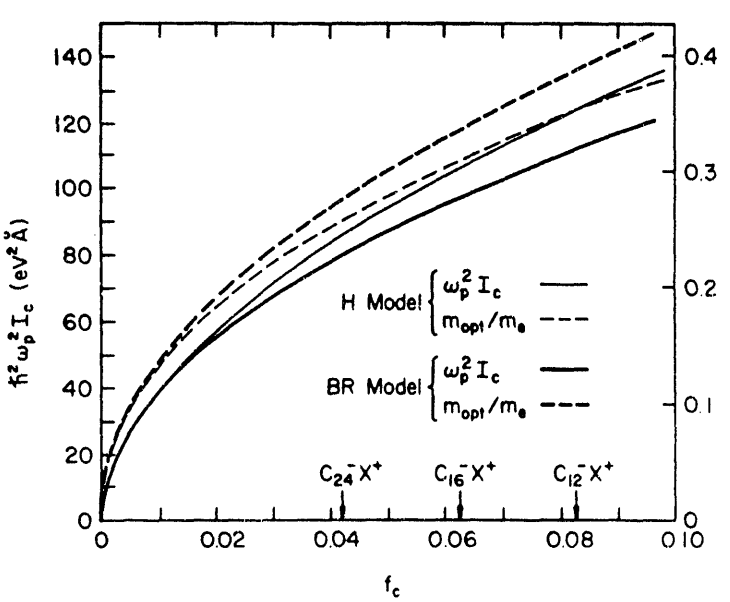

Fig. 4.6. Comparison of the stage-1 Holzwarth (H) and Blinowski-Rigaux (BR) model results for donor-type GICs (γ_0 = 2.9 eV) [4.20]. The quantity I_c is equivalent to I_c in (4.11a, b).

notation C_p^+ (C_p^-) in the figures indicates a charge transfer f_C equivalent to one hole (one electron) per p C atoms, i.e., $f_C = 1/p$. The convergence of the results for the two models at low charge transfer was accomplished [4.20] by setting $\gamma_0 = 2.93$ eV in the BR model.

(c) Tight-Binding Model of Saito and Kamimura

The two-dimensional tight-binding band model of *Saito* and *Kamimura* [4.22] (SK) was also calculated according to the two basic assumptions listed in the previous section for the H and BR models. However, for the stage $n > 2$ compounds, *Saito* and *Kamimura* treated the c-axis charge distribution in a self-consistent way, as explained below. Figure 4.7 shows the C-layer structure of a stage-3 compound, which illustrates the SK band model parameters. The γ_j's are tight-binding transfer integrals between neighboring C atoms in the same and adjacent layers, and δ and δ_j are linear combinations of self-energy integrals from different carbon sites. To determine values for these band parameters for stage $n = 2$–6 KC_{12n}, *Saito* and *Kamimura* carried out a least-squares fit of their tight-binding bands to the self-consistent band structures of *Ohno* and *Kammiura* [4.23], where the value $f_C = 1/12n$ was assumed (i.e., the K 4s band is empty).

To achieve good agreement between their optical results and the SK band model, *Yang* and *Eklund* [4.24] had to adjust two SK parameters. First, to fit the position of observed $c \rightarrow c$ interband structure in the dielectric function at 0.6 eV, they lowered the value of the SK electrostatic parameter δ from 0.46 to 0.3 eV. Second, they found that a k-dependent form for γ_0 was necessary to fit a broad peak observed in $\varepsilon(\omega)$ near 5 eV. This peak is the analog of the 4.6 eV peak in pristine graphite, identified by *Johnson* and *Dresselhaus* [4.19] with transitions between π and π^* bands at the M point. As *Johnson* and *Dresselhaus* pointed out [4.19], for pristine graphite the π–π^* band splitting is approximately $2\gamma_0$, and the second-neighbor C–C interactions (also neglected in the SK model)

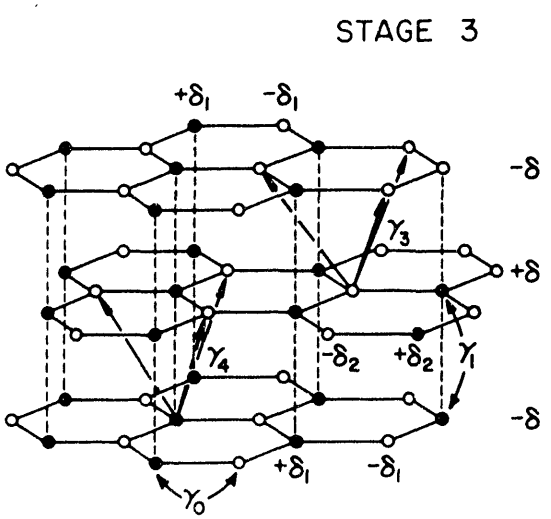

Fig. 4.7. Graphitic carbon structure of a stage-3 compound indicating the tight-binding band parameters for stage $n \geq 3$ GICs [4.22]

make significant contributions to the π-band structure at points far removed from the K-point, leading to "effective" values of $\gamma_0 = 3.2$ eV (K point) and 2.3 eV (M point). Consistent with this observation, *Yang* and *Eklund* [4.24] introduced the following k-dependent form for γ_0:

$$\gamma_0 = \frac{3.0\,\mathrm{eV}}{1 + \chi(\kappa/\kappa_0)}, \tag{4.12}$$

where κ is the length of the wave vector measured relative to the K point, and κ_0 is the wave vector joining K and Γ. A *stage-independent* constant χ in (4.12) was chosen so that $\gamma_0 = 3.0$ eV at the K point and $2\gamma_0 = 4.6$ eV at the M point. Figure 4.8a–c shows the bands resulting from the calculation of *Yang* and *Eklund* [4.24] for KC_{12n} $n = 2, 3, 4$. The vertical arrows in the figure indicate the allowed interband transitions, and the dashed horizontal line indicates the position of E_F consistent with complete charge transfer of one K(4s) electron to

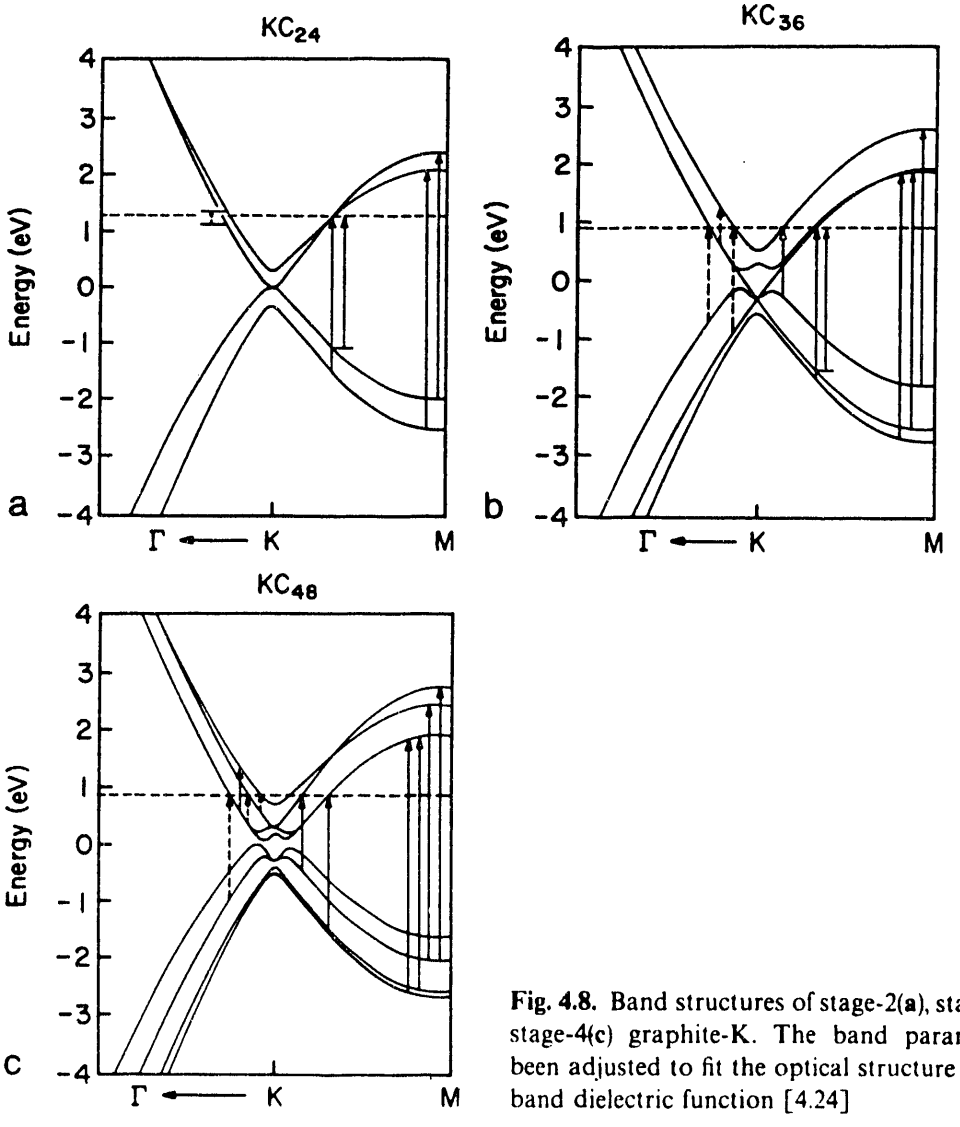

Fig. 4.8. Band structures of stage-2(**a**), stage-3(**b**), and stage-4(**c**) graphite-K. The band parameters have been adjusted to fit the optical structure in the interband dielectric function [4.24]

the C layers. *Yang* and *Eklund* [4.24] have calculated the interband dielectric function for the π bands shown in the figure, including the $\boldsymbol{A} \cdot \boldsymbol{p}$ matrix elements. Their analysis, which leads to values for the net charge distributed to the C_i and C_b layers, is discussed in Sect. 4.3.1a

4.2.3 Charge Transfer and Graphitic Intralayer Phonon Frequencies

In previous contributions to these volumes, *Zabel* [4.25] and *Solin* [4.2] reviewed the lattice dynamics of GICs emphasizing, respectively, the experimental contributions from neutron scattering and optical spectroscopy. Readers are referred to these and previous reviews [4.1, 2]. Here we give a brief introduction to infrared- and Raman-active graphitic intralayer phonons that can be observed optically from experiments on the *c* face, and discuss the theoretical progress in understanding the effects of charge transfer on the respective mode frequencies.

A group-theoretical analysis of the hexagonal structure of pristine graphite (D_{6h}^4 space group) predicts 12 zone-center (i.e., $q = 0$) phonons that transform according to the irreducible representations of the D_{6h}^4 space group [4.26]. Three of these modes are acoustic ($A_{2u} + E_{1u}$), three are infrared-active ($A_{2u} + E_{1u}$), four are Raman-active ($2E_{2g}$), and two are optically silent ($2B_{1g}$). The (E_{1u}, E_{2g}) and (A_{2u}, B_{1g}) symmetry modes involve, respectively, intralayer and interlayer displacements of the carbon atoms.

The frequencies, and sometimes the line shapes, of optically active, graphitic vibrations in GICs are strongly influenced by intercalation through the phenomenon of staging and charge transfer. For stage $n \geqslant 3$, the high-frequency Raman-active E_{2g} singlet observed in graphite at $1582\,\mathrm{cm}^{-1}$ is split into a doublet. The splitting is a consequence of the different net charge per carbon atom on the interior (C_i) and bounding (C_b) layers. The lower (E_{2gi}) and higher (E_{2gb}) frequency components of the doublet have been identified [4.1.2] with intralayer C-atom motion in the C_i and C_b layers, respectively. The frequencies of the E_{2gi} modes have been found to be typically within ~ 5–$10\,\mathrm{cm}^{-1}$ of the E_{2g} mode in pristine graphite, whereas the high-frequency E_{2gb} component has been found to exhibit a frequency ~ 15–$50\,\mathrm{cm}^{-1}$ higher than the E_{2g} mode. Breit-Wigner lineshapes are sometimes observed, indicating a coupling of the intralayer modes to a Raman-active continuum.

Figure 4.9a shows the strong stage dependence for the $\sim 1600\,\mathrm{cm}^{-1}$ E_{2gi} and E_{2gb} modes in the acceptor-type GIC graphite-$FeCl_3$ reported by *Underhill* et al. [4.27]. It shows that the E_{2g} mode in pristine graphite evolves from a singlet (stage $n = \infty$), to a doublet for stage $11 \leqslant n \leqslant 3$, and finally a higher frequency singlet is obtained when interior carbon layers are no longer present (i.e., $n \leqslant 2$). Figure 4.9b shows the IR spectra of *Underhill* et al. [4.27] that show the stage dependence of the E_{1u} modes for graphite-$FeCl_3$ [stage $n = 2, 4, 6, 11$, and ∞ (HOPG)]. The E_{1u} mode lineshape must be analyzed using (4.5) to determine the mode parameters. Note that for stage $n > 2$, independent oscillator contributions to the overall lineshape are not well resolved, indicating that

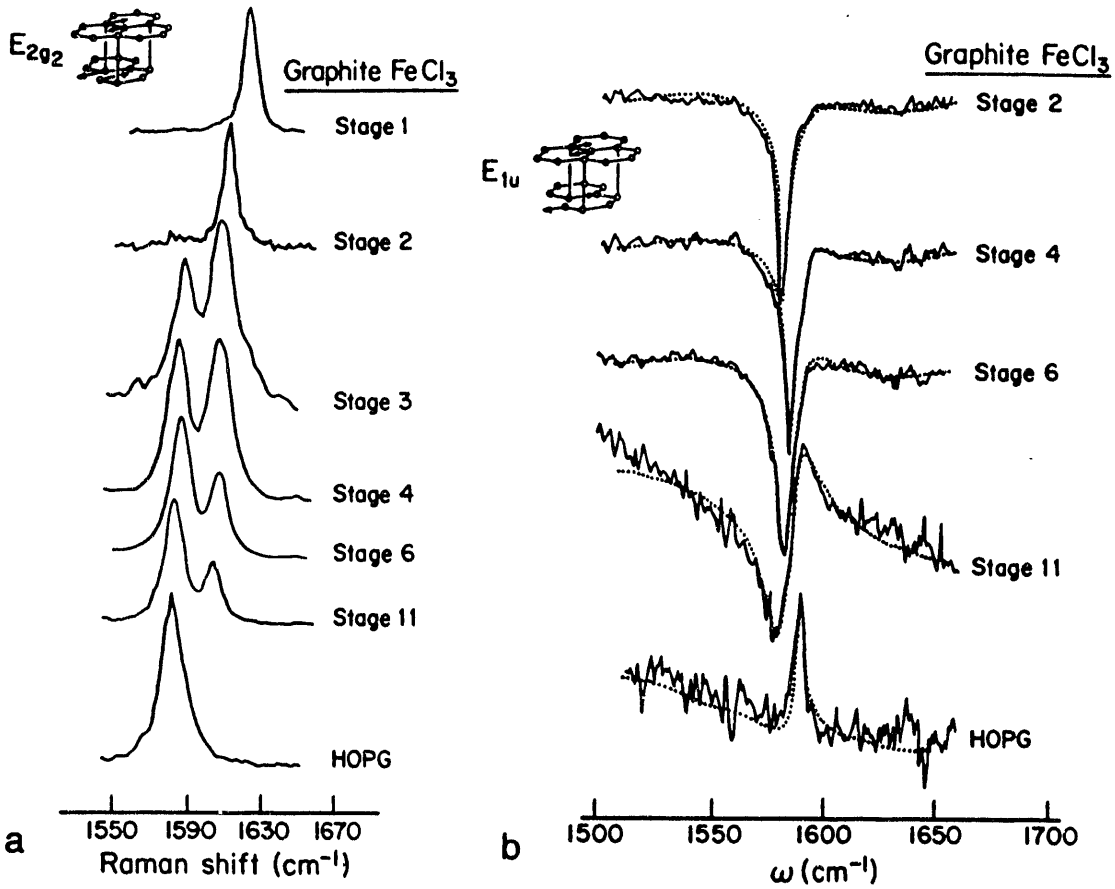

Fig. 4.9. High-frequency, Raman-active (**a**) and infrared-active (**b**) graphitic intralayer modes in graphite $FeCl_3$ [4.27]

it is more difficult to use IR-mode spectra than Raman-mode spectra to determine the stage index of a GIC.

Pietronnero and *Strassler* [4.28] first appreciated the connection between charge transfer and the frequency of the zone-center graphitic modes in GICs. By applying a model used successively to describe several properties of carbon molecules, they derived the stage dependence of the E_{2gi} component for donor- and acceptor-type GICs, obtaining numerical results for the derivative of the mode frequency with respect to reciprocal stage index ($1/n$). They obtained $[\delta(\Delta\omega/\omega)/\delta(1/n)] = \pm 0{\cdot}007$ for acceptor-type (+) and donor-type (−) GICs, consistent with the trends in the data. Somewhat later, *Chan* et al. [4.29] carried out self-consistent electronic band structure calculations on a simulated stage-1 structure containing point ions centered above the hexagons in an AA stacked graphitic structure. By varying the charge transfer between the ions and C layers, they obtained the dependence of the intralayer C–C bond length d_{CC} on f_C. Furthermore, by introducing two interlayer coupling parameters, they carried out a frozen phonon calculation to obtain the stage dependence of the E_{1u} and E_{2g} zone-center mode frequencies, which was found to be in general

agreement with the trends in the experimental data for acceptor-type and donor-type GICs. Unlike the changes in d_{CC}, which in their calculations are completely determined by f_C, the in-plane phonon frequencies were found to be sensitive to both f_C and the interlayer coupling. For comparison Figs. 4.10a, b and 4.11a, b

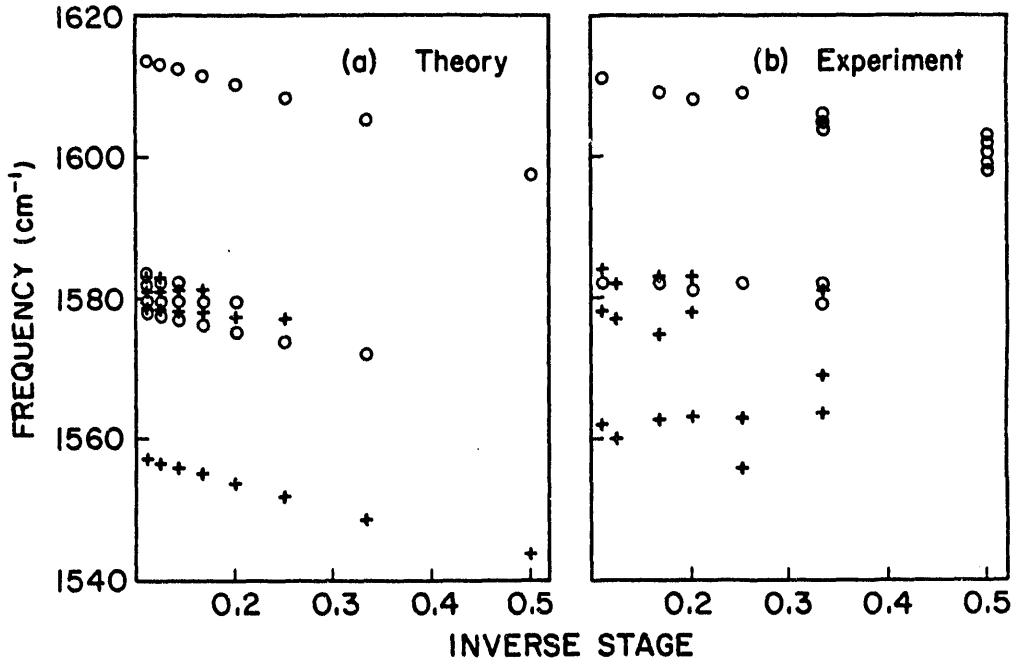

Fig. 4.10. Calculated (**a**) and experimental (**b**) stage dependence of the high-frequency graphitic intralayer mode frequencies for donor-type GICs [4.29]

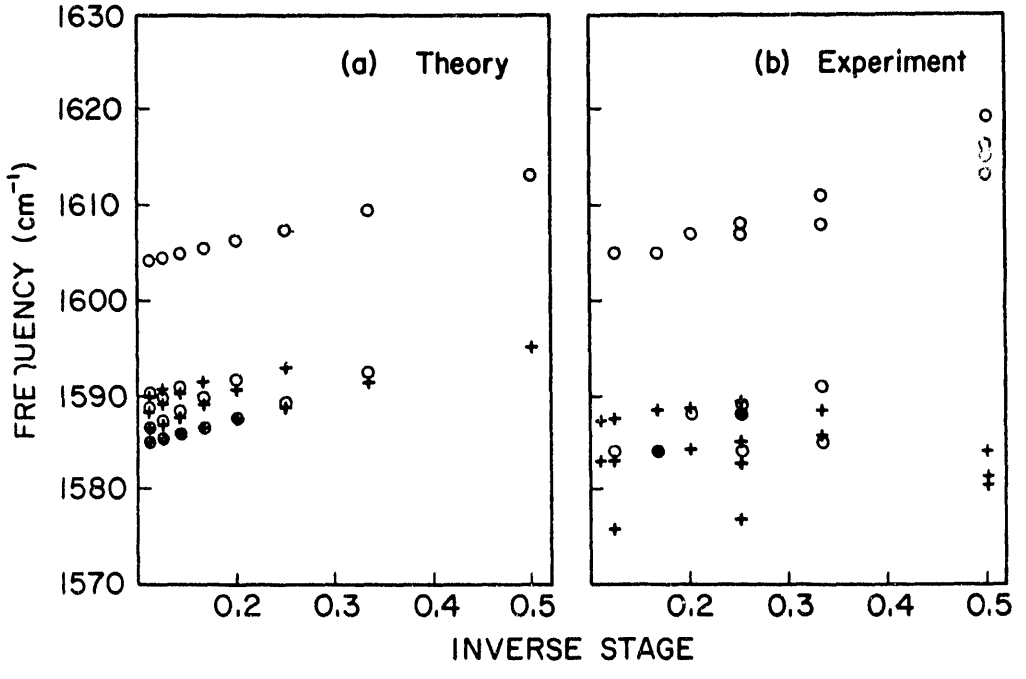

Fig. 4.11. Calculated (**a**) and experimental (**b**) stage dependence of the high-frequency graphitic intralayer mode frequencies for acceptor-type GICs [4.29]

give the model and experimental results, respectively, for donor-type and acceptor-type GICs. Their calculations agree better with the Raman-active mode data than with IR-active mode data. However, the calculations reproduce the salient features (mode stiffening for acceptors and mode softening for donors).

4.3 Experimental Results and Discussion

In this section we review experimental optical studies that have yielded values for the charge transfer and net layer charge distribution in GICs. Other reviews of the optical properties of GICs have appeared recently [4.3, 4]. We endeavor here to consider in some depth the results of a large (but not exhaustive) set of binary and ternary, donor and acceptor GICs. We hope that the progress made in the last ten years in understanding the optical properties of GICs and the effects of charge transfer is apparent.

4.3.1 Donor-Type GICs

(a) Potassium GICs

Binary alkali-metal GICs prepared by the reaction of alkali metals M = K, Rb, or Cs exhibit at stages $n = 1$ and $n > 1$ nominal stoichiometries MC_8 and MC_{12n}, respectively. For $n \geqslant 2$ M GICs, it appears that the charge transfer to the C layers is very nearly 1 electron per M atom [4.1, 2]. However, charge transfer in the stage-1 MC_8 compounds has been somewhat of a controversial issue [4.30–32]. Most experimental effort on the optical properties of binary alkali-metal GICs has focused on K-graphite (stages 1–4), including a pressure-dependent study [4.33] and an in situ electrochemical study [4.34]. Therefore, we have chosen the K-graphite system as the representative binary donor GIC in this review.

KC_8. Over the last 12 years, considerable controversy has developed over the electrical properties of stage-1 MC_8 (M = K, Rb Cs) compounds [4.30–32]. The debate centers around two principal results obtained from two competing band-structure calculations:

(1) the degree of charge transfer $f = 8f_C$ between the K(4s) band and the carbon π band

(2) the s character of a three-dimensional (3D) carrier pocket in the center of the Brillouin zone

Both competing band models place two-dimensional (2D) graphitic π^* carrier pockets at the Brillouin-zone corners. The volume of the occupied π^* states, of

course, determines the value of f; i.e., $f = 1$ means the K 4s states are empty. The central three-dimensional pocket has been identified with hybridized K 4s and graphitic "interlayer" states [4.31, 35, 36], weakly hybridized graphitic states [4.37, 38], or graphitic 3D "interlayer" states [4.32]. *Posternak* et al. [4.39] first proposed the existence of 3D "interlayer" bands in graphitic thin-film systems (e.g., C_6–Li–C_6, C_6–C_6, C_8–K–C_8). The term "interlayer" is derived from the fact that the associated charge density is found between the C and I (or C)layers. Figures 4.12, 13 show for comparison the Fermi surfaces of the two competing band models of *DiVicenzo* and *Rabii* [4.37] and *Ohno* et al. [4.36]. Note that while both calculations result in 2D carriers in the Brillouin-zone corners, only the calculation of *Ohno* et al. [4.36] exhibits a significant population of (zone-center) 3D carriers.

Figure 4.14 shows the c-face reflectances $R(\omega)$ for KC_8 of *Yang* [4.40] (dotted line) and *Fischer* [4.17] (crossed line), which are in good agreement. The inset to the figure, displays the results to *Yang* [4.40] for $\varepsilon_2(\omega)$ plotted as $(\omega\varepsilon_2)^{-1}$ vs. ω^2. In this plot, Drude-like (4.3), free-carrier behavior is linear, and the slope and intercept of the linear portion of the curve determine values for the "effective" plasma frequencies $\omega_p = 4.6$ eV and $\omega_p \tau = 14.5$. We use the term "effective" when more than one set of carriers may contribute to the free-carrier dielectric response. For energies $\omega > 2.9$ eV, the calculated $(\omega\varepsilon_2)^{-1}$ values

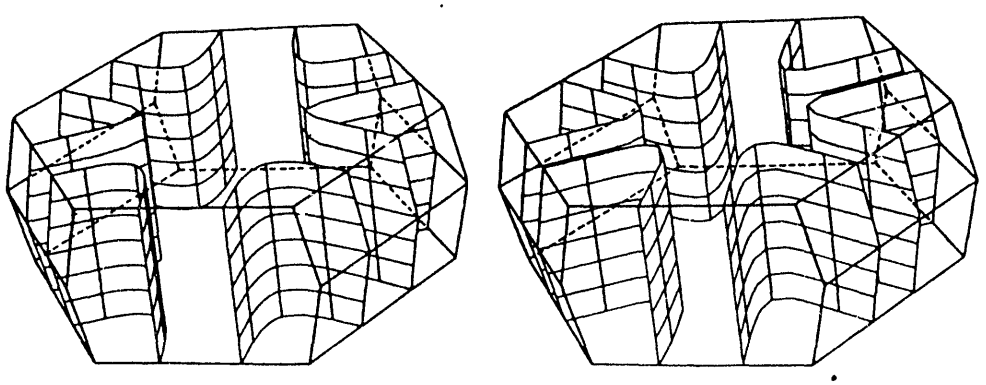

Fig. 4.12. Fermi surface of KC_8 according to the calculations of *DiVicenzo* and *Rabii* [4.37]

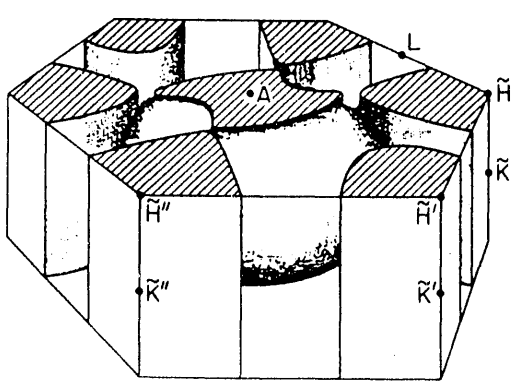

Fig. 4.13. Fermi surface of KC_8 according to the calculations of *Ohno* et al. [4.36]

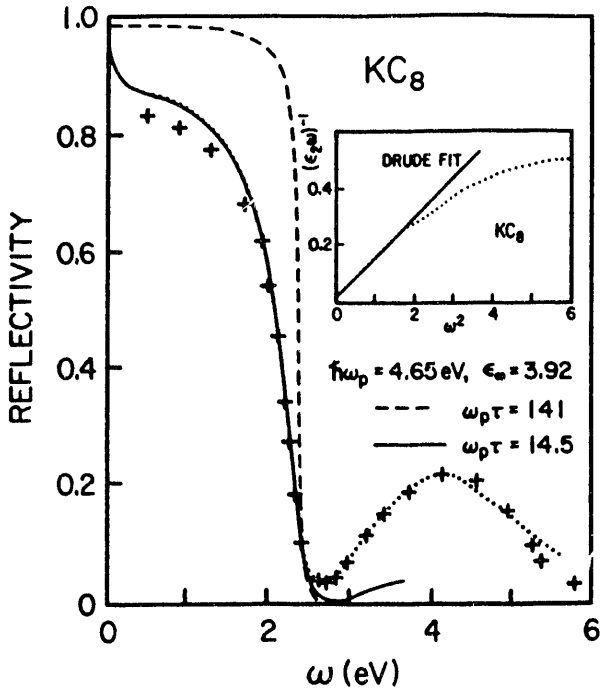

Fig. 4.14. Reflectance ($E \perp c$) of KC_8 in the energy range 0.5–6 eV: dotted line [4.40], crosses [4.17]. The solid [4.40] and dashed [4.17] curves are calculated according to the parameters given in the respective references, and their values are indicated in the figure. The inset is a plot of $1/\omega\varepsilon_2$ versus ω^2; Drude behavior is linear in this plot [4.40]

deviate from the data because of the onset of interband absorption. The solid and dashed lines in Fig. 4.14 represent reflectances calculated according to the Drude model using the same plasma frequency ($\omega_p = 4.6$ eV) and core dielectric constant ($\varepsilon_\infty = 3.9$). However, the dashed curve, which is too steep in the vicinity of the Drude edge, was calculated according to $\tau = 141/\omega_p$ [4.17], indicating this value of τ is too large.

Fischer and coworkers were the first to consider a two-carrier contribution to the plasma frequency of MC_8 compounds [4.41, 42]. They pointed out that the in-plane *dc* conductivity obtained from transport measurements ($\sigma_{dc} \sim 1 \times 10^5$) was significantly greater than the value obtained from a single-carrier Drude analysis, i.e., $\sigma_{opt} = (\omega_{p,\perp}^2 \tau/4\pi) \ll \sigma_{dc}$. They proposed both 2D π^* electrons and a 3D set of electrons as contributors to the effective plasma frequency [4.41, 42].

$$\omega_{p,\perp}^2 = \omega_{p,\pi}^2 + \omega_{p,3D}^2 , \tag{4.13a}$$

$$\omega_{p,\parallel}^2 = \omega_{p,3D}^2 , \tag{4.13b}$$

where $\omega_{p,\perp}$ and $\omega_{p,\parallel}$ refer to the basal plane and c-axis effective plasma frequencies, and $\omega_{p,\pi}$ and $\omega_{p,3D} = 4\pi e^2(N/m^*)_{3D}$ are the plasma frequencies of the 2D π^* and 3D Γ-point carriers, respectively. Using this two-carrier model, *Doll* et al. [4.43] estimated the charge transfer in KC_8 from their experimental value for $\omega_{p,\perp} = 4.5$ eV by assuming values for the 3D carrier mass. Assuming $m^*/m_0 = 2$, they found $f = 8f_C = 0.45 \pm 0.15$; in their work [4.43] the 2D π^* electron contribution was calculated using *Holzwarth's* LCAO model (Sect. 4.2.2b).

Alstrom [4.32] also analyzed charge transfer in the MC_8 compounds using a two-carrier model in which the π^* electrons were described in the BR model approximation, and the 3D carriers were assumed to have an isotropic effective mass. *Alstrom* [4.32] identified these 3D carriers with the "interlayer" states proposed by *Posternak* et al. [4.39]. Fitting his model parameters to specific heat, Fermi-level shift, de Haas–van Alphen (dHvA) data, and the optical results of *Guerard* et al. [4.41], *Alstrom* [4.32] obtained $(m^*/m_0)_{3D} \sim 1.8$, $f = 8f_C = 0.59$, and $\gamma_0 = 2.29$ eV. Note that his value of γ_0 is much lower than most values typically used in analyzing optical results in GICs. For example, we list values of γ_0 used in the analysis of optical data and supported by a second experiment (e.g., dHvA, SdH, electrochemistry): graphite-$SbCl_5$, $\gamma_0 = 2.9$ eV – stages 1 and 2 (Sect. 4.3.2b); graphite-H_2SO_4, $\gamma_0 = 2.62 - 2.93$ – stages 1 and 2 (Sect. 4.3.2a); $KH_{0.8}C_{4n}$, $\gamma_0 = 2.9$ eV – stages 1 and 2 (Sect. 4.3.1b); and KC_{24}, $\gamma_0 = 2.9$ eV yields $f = 1.01$ (Sect. 4.3.1b). The lower value for $\gamma_0 = 2.29$ eV obtained by *Alstrom* [4.32] from his careful analysis of KC_8 data may indicate that significant hybridization between π, π^* and K(4*s*) states has occurred, and/or that the charge transfer into the π^* bands is too high to use the BR model approximation.

Zanini and *Fischer* [4.42] carried out difficult polarized reflectance experiments on the *a* face of KC_8 and CsC_8; they reported $\omega_{p,\parallel} \sim 2$eV for both compounds. Figure 4.15 shows their spectra from the *a* and *c* faces of these compounds. Using their value for $\omega_{p,\parallel}$, the plasma frequency is relatively isotropic, i.e., $\omega_{p,\perp}/\omega_{p,\parallel} = 4.5\,\text{eV}/2.0\,\text{eV} \sim 2.3$. This value favors significant population of 3D states at the zone center. *DiVicenzo* and *Rabii* [4.37] calculated $\omega_{p,\perp} = 4.65$ eV in good agreement with the experimental value 4.5 eV [4.17, 40]. However, they calculate $\omega_{p,\perp}/\omega_{p,\parallel} \sim 15$, much larger than the value obtained from experiment.

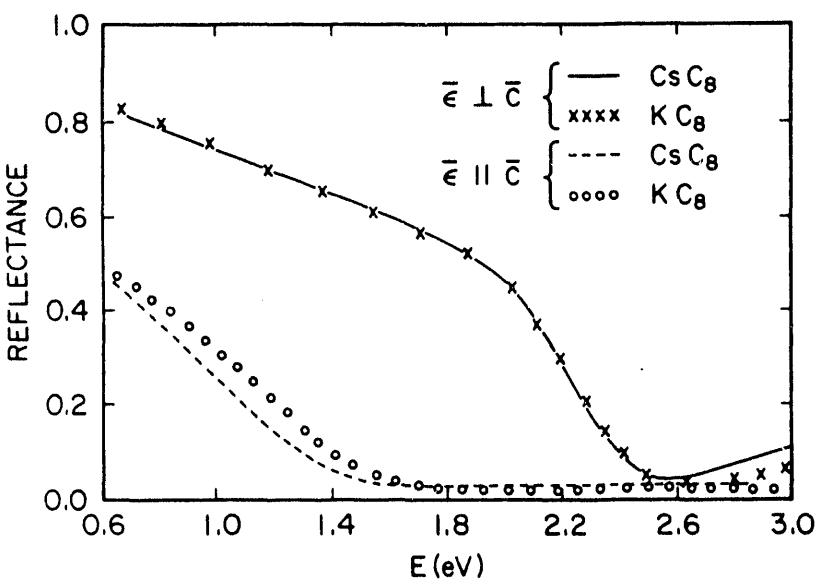

Fig. 4.15. Reflectance of CsC_8 and KC_8 in the vicinity of the Drude edge for $E \perp c$ and $E \parallel c$ [4.10]

In his analysis of KC_8 data, *Alstrom* [4.32] found a set of Drude parameters consistent with both optical and transport results (parallel and perpendicular to the c axis). In the Drude two-carrier model, the zero-frequency optical conductivities parallel and perpendicular to the c axis are given by

$$\sigma_{\mathrm{opt},\parallel} = \omega_{\mathrm{p},3\mathrm{D}}^2 \tau_{3\mathrm{D}}/4\pi \,, \tag{4.14a}$$

$$\sigma_{\mathrm{opt},\perp} = (\omega_{\mathrm{p},3\mathrm{D}}^2 \tau_{3\mathrm{D}} + \omega_{\mathrm{p},\pi}^2 \tau_\pi)/4\pi \,. \tag{4.14b}$$

Setting $\sigma_{\mathrm{opt},\perp} = \sigma_a$ and $\sigma_{\mathrm{opt},\parallel} = \sigma_c$, where σ_a and σ_c are the values obtained from dc transport data, *Alstrom* [4.32] obtained the following values for the Drude parameters: $\omega_{\mathrm{p},3\mathrm{D}}\tau_{3\mathrm{D}} \sim 12.5$, $\omega_{\mathrm{p},3\mathrm{D}} = 1.7$ eV, $\omega_{\mathrm{p},\pi}\tau_\pi = 187$, and $\omega_{\mathrm{p},\pi} = 3.9$ eV.

We conclude that the two-carrier model analysis of the optical data in KC_8 indicates incomplete charge transfer $f = 8f_c \sim 0.5$–0.6, which favors the band structure proposed by *Ohno* et al. [4.36] ($f \sim 0.6$), rather than that proposed by *Rabii* and coworkers [4.37, 38] ($f \sim 1$). Several articles address in detail the controversy about the electronic band structure of KC_8 [4.17, 30, 31, 44].

We turn next to the results of diamond anvil studies of KC_8 (with excess K in the cell) carried out by *Sonnenschien* et al. [4.33]. Using pressures up to 370 they observed sizable shifts in the position of the Drude edge, which they attributed to potassium uptake by the sample. At $p \sim 4$, they observed a discontinuous blue shift of the Drude edge, followed by a weaker, continuous blue shift for increasing pressure up to 70 kbar. Figure 4.16 shows their data for the pressure dependence of ω_p^*, i.e., the zero crossing of $\varepsilon_1(\omega)$ and the approximate position of the Drude edge. The inset to the figure shows the actual shift of the Drude edge

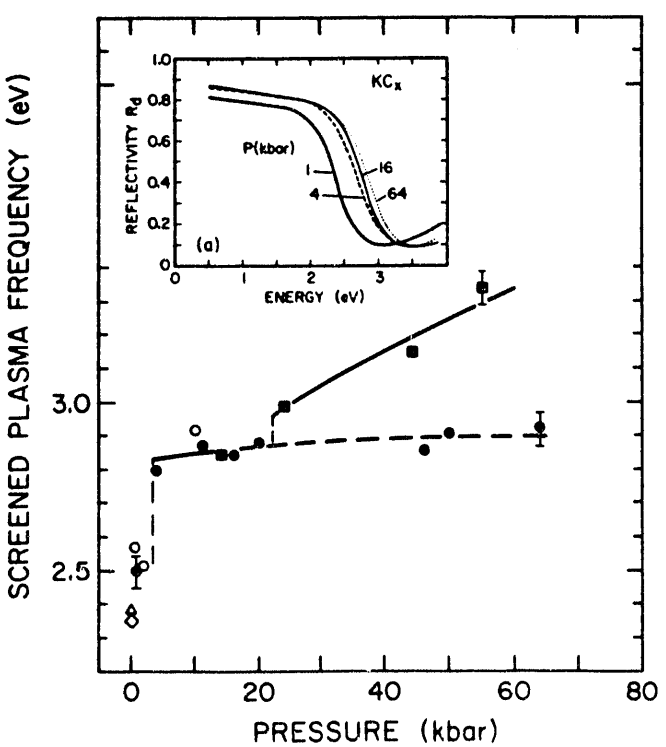

Fig. 4.16. Screened plasma frequency ω_p^* of KC_x as a function of pressure. The inset shows the actual shift of the Drude edge with pressure [4.33]

with pressure. *Sonnenschien* et al. [4.33] found the position of the blue-shifted Drude edge of 4 kbar to be almost identical to the position of the Drude edge in LiC_6 ($f \sim 1$ for LiC_6) [4.17], leading them to interpret the shift as a pressure-driven intralayer densification of potassium resulting in the formation of KC_6, with a charge transfer $f = 6f_C = 1$. If we accept the ambient pressure value $f = 8f_C \sim 0.5$–0.6 discussed above for KC_8, then the pressure and/or the higher K density must raise the K 4*s* band minimum above E_F, leading to $f = 1$ in KC_6. Above 20 kbar, heat-treated samples were found to exhibit a further blue shift in ω_p^* to a maximum value $\omega_p^* = 3.3$ eV (upper branch of ω_p^* versus pressure data in Fig. 8.16), which they similarly identified with further densification leading to a $KC_{4.4}$ compound. Experiments on samples cycled between 1 and 370 showed that the optical effects were reversible.

KC_{12n} Using a small ion-pumped optical cell with a KBr window, *Yang* and *Eklund* [4.24] (YE) measured the *c*-face reflectance of stage $n = 2$–4 KC_{12n} over the range 0.2–6 eV. Figure 4.17a shows their spectra (dots), together with a "modified" Drude fit (solid line) to the data. Here R was calculated according to a Drude-Lorentz form for the dielectric function given by

$$\varepsilon(\omega) = \varepsilon_\infty - \frac{\omega_p^2}{\omega(\omega + i/\tau)} - \sum_j \frac{f_j}{\omega^2 - \omega_j^2 + i\omega\Gamma_j}, \tag{4.15}$$

where the sum is over Lorentz oscillators whose frequencies ω_j correspond to interband transition energies between approximately parallel conduction bands (i.e., $c \to c$ transitions). Kramers-Kronig analyses using density-scaled graphite (Sect. 4.2.1) for the high-energy data extension were carried out to determine the dielectric function.

Yang and *Eklund* [4.24] analyzed the interband contribution to $\varepsilon_2(\omega)$ via the tight-binding π-band model of *Saito* and *Kamimura* (SK) [4.22] (Sect. 4.2.2c). A charge transfer $f = 12nf_C = 1$ was assumed. Figure 8.17b shows their experimental results (crosses) for stages 2–4 interband contributions to $\varepsilon_2(\omega)$ determined by $\varepsilon_{2,\text{inter}} = \varepsilon_2 - \varepsilon_{2,\text{Drude}}$, where the Drude contribution had been determined from fits to both R and $1/\omega\varepsilon_2$. The dashed and solid curves in the figure represent, respectively, the results calculated by *Yang* and *Eklund* [4.24] using the SK band parameters (dashed line) and the YE band parameters (solid line). The interband matrix elements – M_{ss} in (4.4) – were calculated according to a method developed for pristine graphite by *Johnson* and *Dresselhaus* [4.19]. As the figure shows, the energy-band parameter adjustments made by *Yang* and *Eklund* [4.24] to the SK band model significantly improve the fit. Overall, the fits using the YE parameters are fairly good except for the stage-2 and stage-4 compounds at the lowest energy. Below 0.2 eV, both the YE and the SK band parameters predict a sharp peak in $\varepsilon_{2,\text{inter}}$ near 0.15 eV, identified [4.24] with the lowest-energy $c \to c$ transitions. However, the high-energy tails of these low-energy peaks were not observed.

For stage $n > 2$, the distribution of net layer charge between interior (C_i) and bounding (C_b) layers is sensitive to the δ parameter in the SK model. According

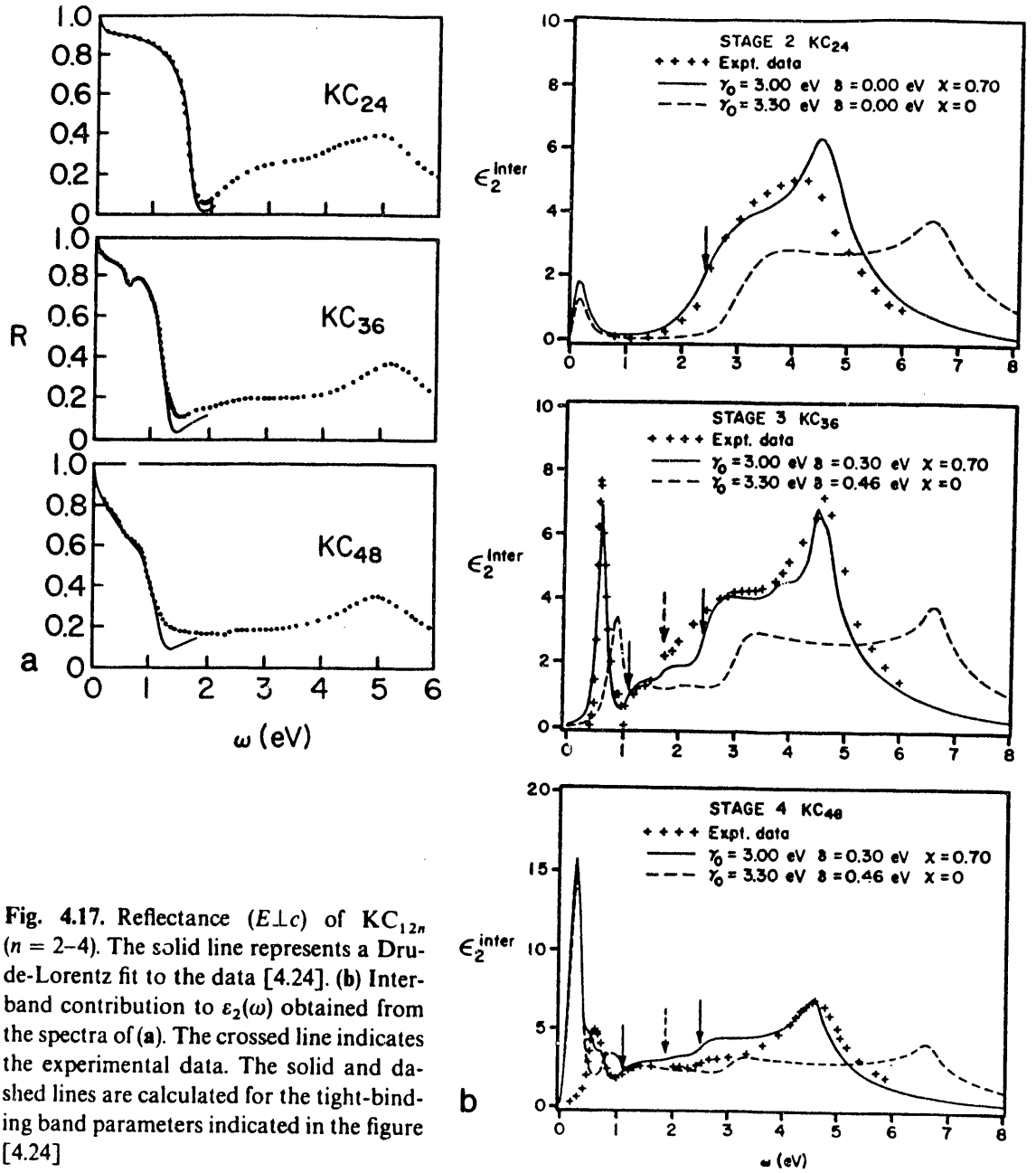

Fig. 4.17. Reflectance ($E \perp c$) of KC_{12n} ($n = 2$–4). The solid line represents a Drude-Lorentz fit to the data [4.24]. (**b**) Interband contribution to $\varepsilon_2(\omega)$ obtained from the spectra of (**a**). The crossed line indicates the experimental data. The solid and dashed lines are calculated for the tight-binding band parameters indicated in the figure [4.24]

to the results of *Yang* and *Eklund* [4.24], strong $c \rightarrow c$ transitions should occur between parallel bounding-layer and interior-layer π^* bands separated in energy by 2δ. These transitions were identified [4.24] with the ~ 0.60 eV peak in the stage-3 and stage-4 data. Thus, the 0.6 eV peak is a direct experimental measure of the electrostatic energy difference between the bounding and interior carbon layers in these compounds. *Yang* and *Eklund* [4.24] compared values for the fractional layer charge in the interior and bounding layers of KC_{12n} obtained from the SK band structure using both the SK and YE band parameters. These values can also be compared with those obtained by *Kume* et al. [4.45] by applying the Koringa relation to the spin-lattice relaxation times they obtained

from their ^{13}C NMR experiments. For example, in stage-3 KC_{36}, the NMR and optical results are in good agreement, with $\sim 90\%$ of the K(4s) electrons transferred to the bounding C_b layers, and 10% to the interior C_i layers. In the SK band structure, the interior layer charge for stage-3 is noticeably lower (1.3%). Unfortunately, there are no NMR results for stage-4. However, the stage-4 optical results (84%, bounding layer; 16%, interior layer) and the stage-6 NMR results (82%, bounding layer; 18%, interior layer) are in good agreement, whereas the values for the interior layer charge in the stage-4 and stage-6 SK band structure are lower (i.e., 3.0%).

Comparing the band-structure electronic density of states at the Fermi energy $D(E_F)$ with that obtained from specific-heat measurements [4.46, 47] $D^*(E_F)$, *Yang* and *Eklund* [4.24] determined values for the electron-phonon coupling constant λ via the relation $D^*(E_F) = D(E_F)(1 + \lambda)$. They found $\lambda = 0.3$, 0.4, and 0.5 for stages 2, 3, and 4, respectively. These values may be compared with the value $\lambda = 0.3$ obtained by *Alexander* et al. [4.48] for the stage-1 MC_8 (M = K, Rb, CC) from the transition temperature T_c to the superconducting state.

Nogami et al. [4.34] performed in situ optical studies on thin films of K-graphite in an electrochemical cell. Poly(*p*-phenylene vinylene) films (5 microns thick) were first graphitized at 2900 °C for 1 hour in high-purity argon. The cell electrolyte was prepared by dissolving $KAsF_6$ in dimethyl sulfoxide (DMSO). A Pt wire was used as the counterelectrode. The films turned green at a cell potential of -3.5 volts. Response times as short as 50 ms were reported for their "color switching" cell.

The Drude edge was observed at 0.8 eV (midpoint) and the Drude minimum occurred at $E_m = \sim 0.9$ eV, compared with the value $E_m = 2.6$ eV found for KC_8 [4.17, 40, 43]. *Nogami* et al. [4.34] analyzed their reflectance data using a modified Drude model, in which the interband transitions were modeled as a complex dielectric constant, similar to that used in early studies of the optical properties of GICs by *Zanini* and *Fischer* [4.42]. From their Drude analysis, they obtained a "bare" plasma frequency for their electrochemically prepared K-graphite of $\omega_p = 2.6$ eV, almost 2 eV lower than obtained [4.17, 40, 43] for chemically prepared KC_8. As a result, *Nogami* et al. concluded [4.34] that only carbon π electrons were generated in eletrochemically prepared KC_x. However, this conclusion appears unfounded, since they made no attempt to measure the K/C stoichiometry or to determine if DMSO solvent molecules may have been co-intercalated. The co-intercalation of NH_3 or tetrahydrafuran (THF) into the K layers of ternary solvent K GICs has been shown to lower the plasma frequency (Sect. 4.3.1c).

(b) Potassium-Hydrogen GICs

Shortly after the report of the synthesis of the alkali-metal graphite compounds by *Nixon* and *Parry* [4.49], hydrogen and hydrogenic gases were found by *Colins* and *Herold* [4.50] to react chemically (i.e., chemisorption) and by

Watanabe et al. [4.51] to react physically (i.e., physisorption) with the binary alkali-metal host.

For the $T \sim 300$ K reaction of H_2 with KC_8, *Enoki* et al. [4.52] determined that the hydrogen molecules dissociated, becoming stabilized as atomic hydrogen. From X-ray studies, *Conard* et al. [4.53] found that the potassium ions were rearranged in the I layer to form a three-layer sandwhich (K-H-K), similar to that found in the ternary $KHgC_{4n}$ (Sect 4.3.1d). As the hydrogen concentration (x) was increased in KH_xC_8, *Enoki* et al. [4.52] found that the material evolved from a stage-1 phase ($x \leqslant 0.10$), to a mixture of stages 1 and 2 ($0.10 = x < 0.67$), and then to a homogeneous (hydrogen-saturated) stage-2 material ($x = 0.67$). In an interesting observation, *Kaneiwa* et al. [4.54] found that as x was changed from 0 to ~ 0.19, the superconducting transition temperature of KH_xC_8 first increased and then disappeared entirely. *Enoki* et al. [4.55] found the introduction of hydrogen to C_8K to reduce the in-plane electrical conductivity by about 50% as x increased from 0 to 0.67, and attributed the decrease to a reduction in the number of carriers in the carbon π bands. Hydrogen was therefore proposed to act as an acceptor ion (H^-), causing the back-donation of electrons from the carbon to the intercalate layers [4.55].

Watanabe et al. [4.56] first proposed that at low temperatures ($T = 77$ K) hydrogenic *molecules* physisorb into the alkali-metal layers of stage $n \geqslant 2$ alkali-metal GICs (MC_{12n}). For the potassium compounds, the low-temperature adsorption of hydrogen is accompanied by a 0.3 Å c-axis lattice expansion [4.56, 57]. The mechanism for adsorption has been recently addressed by *Lee* et al. [4.58]. Despite the earlier proposals of hydrogen physisorption in KC_{24} by *Watanabe* et al. [4.51, 56], *Kondow* et al. [4.59–61] reported the results of several experiments that they interpreted to indicate that 40%–60% of the electrons originally donated by the K 4*s* states to the C layers were back-donated to the intercalate layers. This large amount of electron back-donation was disputed by *Terai* et al. [4.62], who claimed that there was little, if any, back-donation of electrons during hydrogen uptake.

Hydrogen Chemisorption in KC_8. *Doll* et al. [4.43, 63] carried out optical studies of electron back-donation in KH_xC_8. Since the $T = 300$ K reaction rate of hydrogen with KC_8 is prohibitively slow in well-ordered graphite such as HOPG (which is a desirable host material for optical measurements), *Doll* and *Eklund* [4.63] first examined the hydrogen chemisorption in Grafoil-based KC_8, where the absorption kinetics are comparable with graphite powder. However, the surface of Grafoil is not optically smooth. To account for the loss of specularly reflected light from Grafoil-based samples, they determined a wavelength-dependent correction factor for Grafoil and assumed that this correction factor was not appreciably altered by intercalation. To test the validity of this approach to Grafoil-based GICs, they first examined the optical relectance of KC_8 Grafoil. Figure 4.18 shows their data, uncorrected for diffuse scattering loss (dotted line), together with the corrected data (crosses). For comparison, the dashed line is the spectrum of KC_8 HOPG, and the solid line is a Drude fit to

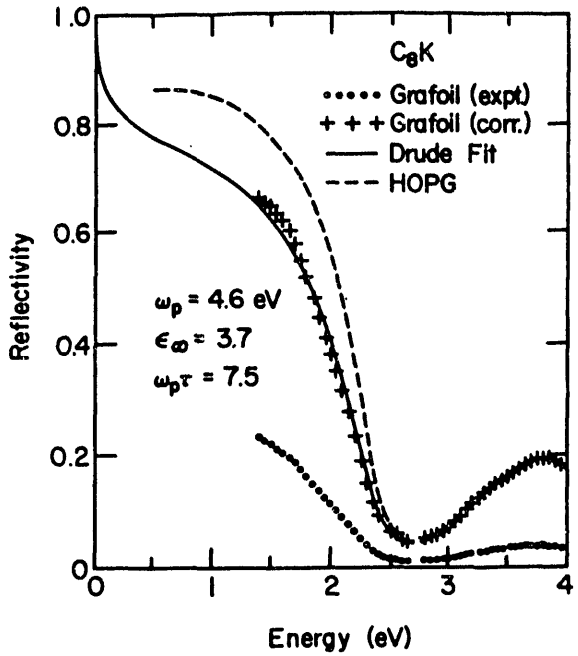

Fig. 4.18. Reflectance ($E \perp c$) of KC_8 Grafoil (dotted line) and KC_8 HOPG (dashed line). The crosses represent the spectrum of KC_8 Grafoil corrected for diffuse scattering loss. The solid curve is a Drude fit to the corrected spectrum for the parameters indicated in the figure [4.63]

the corrected spectrum of KC_8 Grafoil. The figure shows the Drude parameters obtained from the fit, and ω_p and ε_∞ are found to be in excellent agreement with the parameters previously reported for KC_8 HOPG [4.17, 43]. *Doll* and *Eklund* further observed that the free-carrier lifetime in KC_8 Grafoil is $\sim 1/2$ that of the KC_8 HOPG, which they attributed to a larger impurity scattering in the Grafoil-based material [4.63].

Having shown that a surface roughness correction can be successfully applied to Grafoil-based GICs, *Doll* and *Eklund* [4.63] obtained the corrected reflectance spectrum of the stage-2 (hydrogen-saturated) compound $KH_{0.67}C_8$ Grafoil in the same way (Fig. 4.19). The dots show the uncorrected data, and the crosses represent the spectrum corrected for surface roughness. The solid line is a Drude fit to the corrected spectrum; the figure lists the parameters. Converting the plasma frequency to f_C in the framework of the BR model [4.13] (Sect. 4.2.2a), *Doll* and *Eklund* obtained $f_C \sim 0.040 \pm 0.002$. They assumed that the K 4s band is empty and that the contribution to the effective plasma frequency from H 1*s* carriers is negligible in comparison with that from the light and more numerous carbon π^* electrons. *Doll* and *Eklund* [4.63] calculated the population F_H in the hydrogen 1*s* band using $F_H = 1 + (1 - 8f_C)/0.67$, where F_H is therefore in units of electrons per hydrogen atom. They obtained $F_H = 2.01 \pm 0.03$, indicating that the hydrogen band is full or nearly full; i.e., the minimum value of $F_H = 1.98$, or 0.02 holes per H atom. On the basis of later, more sensitive, proton NMR measurements by *Miyajima* et al. [4.64] and ultraviolet photoelectron spectroscopy (UPS) by *Yamamoto* et al. [4.65], a small number of holes were indeed found in the hydrogen band.

Guerard et al. [4.66] later discovered that stage $n = 1$ and $n = 2$ potassium-hydride GICs with stoichiometry $KH_{0.8}C_{4n}$ could be obtained by reacting KH

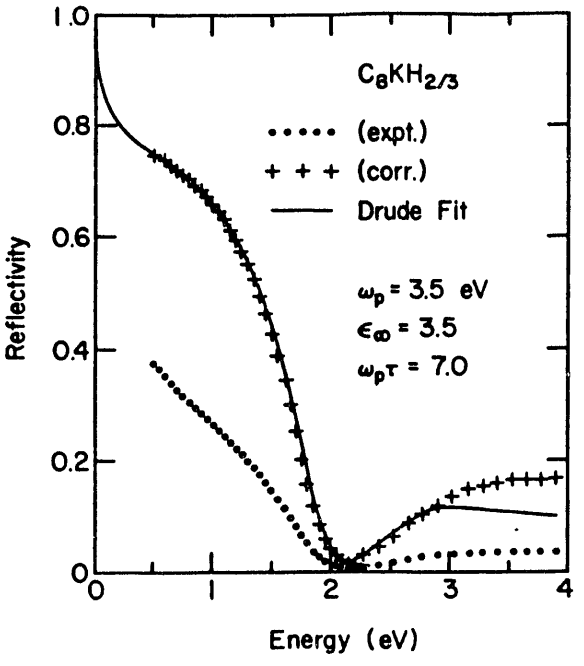

Fig. 4.19. Reflectance of $KH_{0.67}C_8$ Grafoil. The spectrum corrected for diffuse scattering loss is indicated by the crossed line. The solid curve is a Drude fit to the corrected spectrum for the parameters indicated in the figure [4.63]

salt with well-ordered graphite (e.g., HOPG). Charge transfer studies of these compounds were also carried out by *Doll* et al. [4.43] and compared with their binary GIC counterparts KC_8 and KC_{24}. Kramers-Kronig analyses to determine $\varepsilon(\omega)$ were carried out using density-scaled graphite for the high-energy data extension (Sect. 4.2.1). Figures 4.20, 21 show the results of *Doll* et al. [4.43] for $\varepsilon_2(\omega)$. The arrows in the figures show the midpoints of the respective $\pi \rightarrow \pi^*$ thresholds, identified as E_T. *Shung* [4.67] has shown theoretically that the $\pi \rightarrow \pi^*$ interband threshold is broadened about $\hbar\omega \sim 2E_F$ due to electron scattering. The Drude behavior of the free-carrier contribution to $\varepsilon_2(\omega)$ in KC_8, KC_{24}, $KH_{0.8}C_4$, and $KH_{0.8}C_8$ is evident in the data of *Doll* et al. [4.43] (Fig. 4.22), where $1/\omega\varepsilon_2$ is plotted against ω^2. The slope and intercept of the low-energy linear portion of the data were used to deduce values for the Drude parameters (ω_p, τ).

Using the reported stoichiometry KH_xC_{4n} (stage $n = 1, 2$) and charge neutrality, *Doll* et al. [4.43] expressed the relation between the fractional band occupations as

$$(F_K - 1) + x(F_H - 1) + 4nf_C = 0 \,, \tag{4.16}$$

where F_K, F_H, and f_C represent the number of electrons in the respective K 4*s*, H 1*s*, and C π^* bands. Assuming the H 1*s* band is essentially full (i.e., $F_H = 2$) and $x = 0.8$, (4.16) reduces to $f_C = (0.2 - F_K)/4n$. Using this result, *Doll* et al. [4.43] then interpreted the values for the effective plasma frequency in terms of a "two-carrier" model (Sect. 4.3.1a, Eq. 4.13a), with the π^* electrons described according to either the BR model [4.13] (stage 1 and 2) or the H model [4.18] (stage-1 only) (Sects. 4.2.2a, b). The second carrier type was assigned a range of effective mass $m = 1 - 2\,m_0$. Their minimum experimental value for ω_p (i.e.,

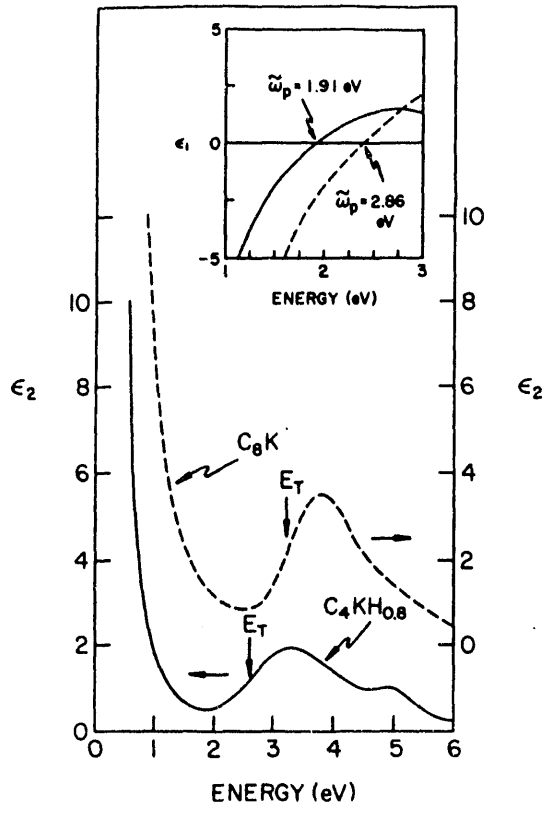

Fig. 4.20. Plot of Kramers-Kronig derived values for $\varepsilon_2(\omega)$ for KC_8 and $KH_{0.8}C_4$. The inset shows the zero-crossing of $\varepsilon_1(\omega)$. The arrows labeled E_T indicate the mid points of the respective inter-π-band threshold [4.63]

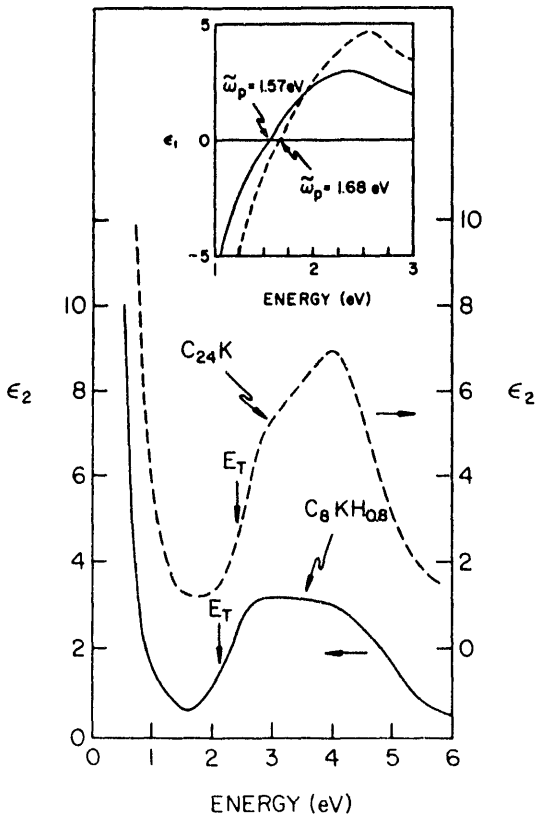

Fig. 4.21. Plot of Kramers-Kronig derived values for $\varepsilon_2(\omega)$ for KC_{24} and $KH_{0.8}C_8$. The inset shows the zero-crossing of $\varepsilon_1(\omega)$. The arrows labeled E_T indicate the midpoints of the respective inter-π-band threshold [4.63]

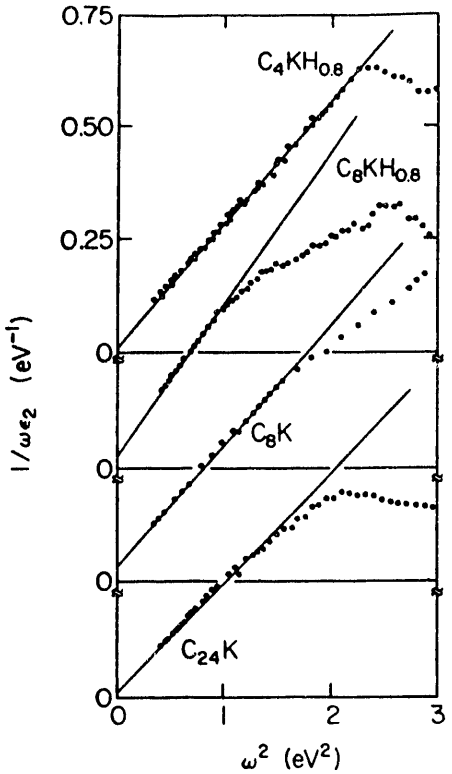

Fig. 4.22. Plot of $1/\omega\varepsilon_2$ versus ω^2 for KC_8, KC_{24}, $KH_{0.8}C_8$, and $KH_{0.8}C_4$. Drude behavior is linear in this plot, and the slope and intercept determine ω_p and τ [4.43]

$\omega_p - \Delta\omega_p$, where ω_p is the value obtained from the Drude analysis, and $\Delta\omega_p = 0.1$ is the experimental uncertainty) was found consistent with $F_K \sim 0.02$ electrons per K atom in the K(4*s*) band (where $\gamma_0 = 3.0$, $m = 1$). Of course, if the K(4*s*) band is empty, and the second carrier type was assigned instead to holes in an H(1*s*) band, their result would indicate 0.025 holes per H atom. The H and BR models ($\gamma_0 = 2.9$–3.0) were found to yield essentially the same values for f_C and E_F for $KH_{0.8}C_4$: $f_C = 0.05$ and $E_F = 1.5$ eV.

For $KH_{0.8}C_4$, the values obtained for E_F from the position ($\sim 2E_F$) of the interband threshold were found to be in good agreement with those obtained from ω_p. The H model and BR model gave slightly different results, and the difference was attributed to the asymmetry of the π and π^* bands obtained only in the H model. In the BR model, the π (valence) and π^* (conduction) bands exhibit mirror symmetry near the K point, and the dominant transitions between these mirror image bands yield an inter-π-band threshold with midpoint $E_T = 2E_F$. In the H model, the small asymmetry in the π and π^* bands near the K point leads to a midpoint $E_T \sim 2E_F - \Delta E$, where the correction factor ΔE increases slowly with increasing E_F($\Delta E \sim 0.1$ eV at $E_F = 1.4$ eV).

Note that in the course of studying the charge transfer in the potassium-hydride GICs, *Doll* et al. [4.43] also carried out a BR-model analysis of the reflectance of stage-2 KC_{24} using $\gamma_0 = 2.9$ eV and $\gamma_1 = 0.375$ eV. From ω_p they obtained the value $f = 1.0 = 24f_C$ for the charge transfer from the K(4*s*) band to the π^* band (i.e., $f_K = 0$). Using the BR model to convert the experimental value of ω_p into E_F, they obtained $2E_F = 2.84$ eV, in excellent agreement with the midpoint ($E_T = 2.80$ eV) of the interband threshold (Fig. 4.21).

The values for f_C and E_F obtained optically by *Doll* et al. [4.43] for the $KH_{0.8}C_{4n}$ compounds can be compared with those obtained from Shubnikov-de Haas (SdH) experiments by *Enoki* et al. [4.68]. Whereas good agreement was obtained between optical and SdH results for the stage-2 hydride (SdH [4.68]: $f_C = 0.033$, $E_F = 1.15$ eV; Opt [4.43]: $f_C = 0.026$, $E_F = 1.13$ eV), a large disagreement arose for the stage-1 compound (SdH [4.68]: $f_C = 0.020$, $E_F = 0.65$ eV; Opt [4.43]: $f_C = 0.05$, $E_F = 1.62$ eV). However, high-frequency SdH oscillations are experimentally difficult to observe. If the observed stage-1 SdH frequencies of *Enoki* et al. [4.68] are reindexed assuming that the highest frequency oscillation was not observed, then the stage-1 values for f_C and E_F obtained from the SdH and optical studies can be brought into good agreement.

Hydrogen physisorption in KC_{24}. *Doll* and *Eklund* [4.69] carried out an optical study of the low-temperature physisorption of H_2 into stage-2 KC_{24} to investigate the controversy regarding the back-donation of electrons from the C layers to the $K(H_2)_x$ layers as a result of the hydrogen uptake. Figure 4.23 shows the reflectance spectra reported by *Doll* and *Eklund* [4.69] for $K(H_2)_x\,C_{22.6}$ before ($x = 0$) and after ($x = 1.6$) the $T = 77$ K physisorption of H_2. The C/K stoichiometry was determined by the change in weight of the HOPG-based sample, and the saturation hydrogen concentration at $p = 1000$ Torr and $T = 77$ K was measured to be $x = 1.6$. The inset shows the energy region near the reflectance minimum (E_m) on a magnified scale. Visual inspection of the sample through the optical dewar window revealed that, during production of the hydrogen-saturated compound, the sample surface had transformed from the specular, steel-blue color of $KC_{22.6}$ to a dull gray surface. *Doll* and *Eklund* concluded that

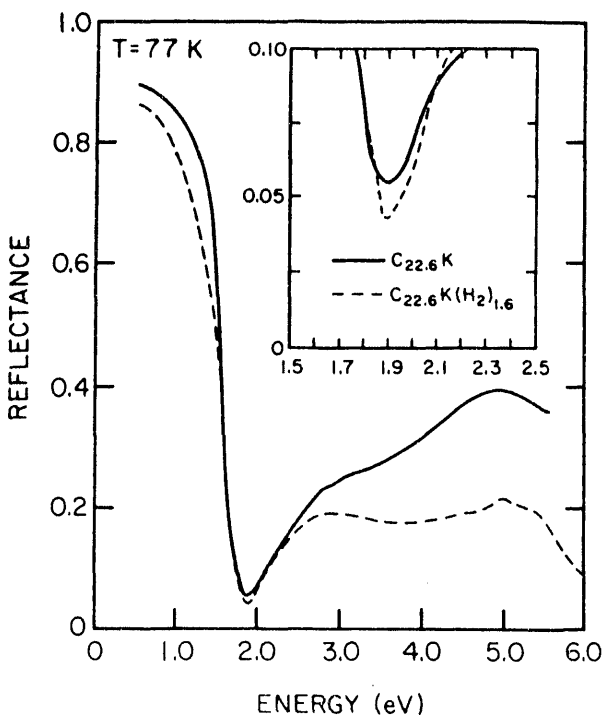

Fig. 4.23. The reflectance ($E \perp c$) spectra of $KC_{22.6}$ (solid line) and $K(H_2)_{1.6}C_{22.6}$ (dashed line). The latter compound is formed by the $T = 77$ K adsorption of H_2. The inset shows the energy region near the reflectance minimum (E_m) [4.43]

this transformation was, in part, due to a surface roughness induced by the intercalation of hydrogen. Unlike the studies in Grafoil-based $KH_{0.67}C_8$, a wavelength-dependent correction factor was not obtained. However, this factor should be a slowly varying function of energy. Therefore, it should not seriously distort a sharp Drude edge or induce an artificial shift in the position of the following reflectance minimum (E_m).

To determine the degree of the electron back-donation $f_B = (1 - 22.6 f_C)$ under these experimental circumstances, *Doll* and *Eklund* used the stage-2 BR-model dielectric function [4.13] to calculate the f_B dependence of the reflectance minimum E_m. The parameter f_B represents the fraction of the K 4*s* electron originally donated to the C layers that is *returned* to the I layers by virtue of the H_2 uptake. Values for E_m were calculated using $\tau = 2.2 \times 10^{-15}$ s, $T_{eff} = 700$ K, i.e., parameters that fit the spectrum of the binary host $KC_{22.2}$ before the physisorption of hydrogen. For small f_B, they obtained $f_B = (1.21\ \mathrm{eV}^{-1})\ \Delta E_m$, where $\Delta E_m = E_{m0} - E_m$, and $E_{m0} = 1.90$ eV is the calculated position of the Drude minimum for $f_B = 0$. Experimentally, they found $E_m = 1.88 \pm 0.01$ eV for $C_{22.6}K(H_2)_{1.6}$, with the uncertainty arising from the point spacing of the $R(\omega)$ data. From the shift $\Delta E_m = 0.02$ eV, they concluded that $f_B = 0.01 \pm 0.01$, or an upper bound for $f_B = 0.02\ e$/K atom or 0.0065 e/H atom. This small value for f_B is consistent with the results of *Terai* et al. [4.62] and *Sano* and *Inokuchi* [4.70], and disagrees sharply with the much larger value $f_B \sim 0.40\ e$/K atom reported by *Kondow* and coworkers [4.59–61]. According to the calculations of *Doll* and *Eklund* [4.69], the value $f_B \sim 0.40$ would have caused a redshift $\Delta E_m \sim 0.5$ eV, much greater than the small shift observed.

(c) Potassium-NH_3 and Potassium-THF GICs

Ternary GICs containing both alkali-metal atoms and solvent molecules (e.g., ammonia NH_3, benzene C_6H_6, and tetrahydrofuran (THF) C_2H_8O) in the intercalate (I) layers can be prepared by a two-step process [4.8, 71, 72]. The first step is the synthesis of an alkali-metal GIC, and the second step is the reaction of this binary GIC with the particular solvent vapors. The intercalation of the large solvent molecules increases considerably the intercalate layer thickness and induces a measurable back-transfer of electrons to the intercalate layers as observed in NMR, X-ray, and optical studies (to be discussed below). The back-transfer is observed optically as a redshift of the Drude edge, consistent with a decrease of the electron population in the carbon π^* bands.

$K(NH_3)_xC_{12n}$. Stage $n = 1$ and $n = 2$ GICs with stoichiometry $K(NH_3)_xC_{12n}$ ($0 \leq x \leq 4.4$) can be prepared, respectively, by the exposure of stage-2 KC_{24} [4.72] and stage-3 KC_{36} [4.73] to the vapors of ammonia (NH_3). The initial binary GIC has an empty K(4*s*) band [4.1, 2], and the subsequent intercalation of NH_3 into KC_{24} results in a back-transfer of electrons from the carbon to the $K(NH_3)_x$ layers, as first reported in X-ray studies by *York* and *Solin* [4.72] At $x \sim 1.4$ a stage $2 \rightarrow 1$ transition occurs, and further NH_3 can be accommodated in the stage-1 compound, up to a maximum value $x = 4.4$ [4.72]. *Huang* et al.

[4.74] first reported the results of in situ optical reflectance studies and electrical transport measurements of the c-axis (ϱ_c) and a-axis (ϱ_a) resistivity experiments in $K(NH_3)_xC_{24}$. At $x \sim 4$, they observed a sudden small drop in ϱ_a, which they identified with a Mott transition in the $K(NH_3)_x$ layers.

According to their model [4.74], as x increases from 1.5 to ~ 4 in the stage-1 compound, electrons continue to be transferred back from the C layers to localized states in the $K(NH_3)_x$ layers. At $x \sim 4$, the density of these electrons is sufficient for the Mott transition to occur and a metallic band is formed. This band then conducts in parallel with the carbon π^* band. Nonmetal-metal transitions had been observed previously in 3D alkali-metal-NH_3 liquids [4.75] and identified with Mott transitions.

Figure 4.24 shows the reflectance spectra reported by *Zhang* et al. [4.76] for the $x = 0$, 1.49, 4.11, 4.38 $K(NH_3)_xC_{24}$ compounds; the spectra are the same as those reported previously by *Huang* et al. [4.74]. The solid and dashed lines represent, respectively, the data and Drude fits to the data. Values for the plasma frequency were obtained from the Drude fits to the $R(\omega)$ data. The experimental values of ω_p obtained by *Zhang* et al. [4.76] are $\omega_p = 4.12$ eV ($x = 0$), 2.04 eV ($x = 1.49$), 3.33 eV ($x = 4.11$), and 3.27 eV ($x = 4.38$). The value of ω_p obtained for the stage-2 KC_{24} host is 0·08 eV, slightly lower than the value $\omega_p = 4.2 \pm 0.1$ eV reported by *Doll* et al. [4.43]. Note that the plasma frequency of the $x = 1.49$ compound has no simple interpretation, since this is a "residue" compound consisting of KC_8 and stage-1 and stage-2 $K(NH_3)_xC_{24}$ [4.72]. Using the H and BR models and assuming an empty K 4s band, *Zhang* et al. [4.76] converted their experimental plasma frequencies for the stage-1 $K(NH_3)$ GICs into values

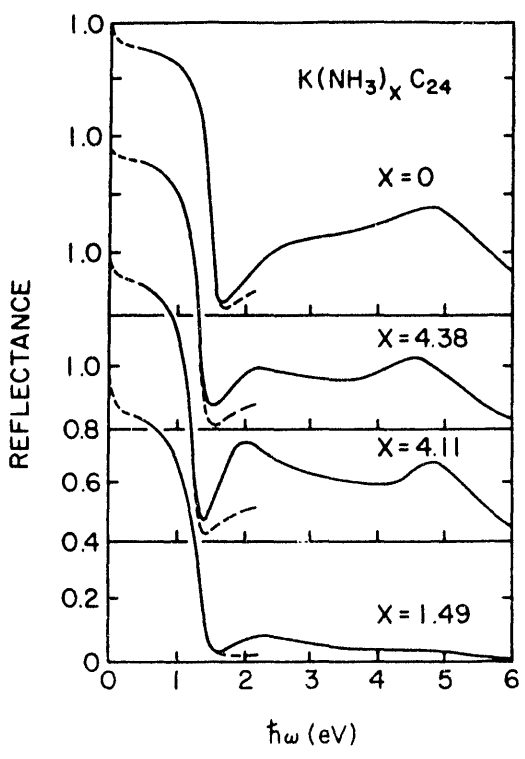

Fig. 4.24. Reflectance ($E \perp c$) of $K(NH_3)_xC_{24}$. The dashed lines represent Drude fits to the data [4.76]

for f_C. This conversion assumed that the contribution to ω_p from the intercalate layer is small enough to be neglected. The degree of back-donation is perhaps easiest to appreciate in terms of $f_K = (24 + \delta) f_C$, i.e., the charge per K atom in the carbon π^* band, where δ is the deviation from the nominal K/C stoichiometry determined by weight uptake measurements. *Zhang* et al. [4.76] obtained the following results: $f_K^{(BR)} = 0.80$ and $f_K^{(H)} = 0.74$ for $x = 4.38$ compound, and $f_K^{(BR)} = 0.85$ and $f_K^{(H)} = 0.78$ for the $x = 4.11$ compound. In other words, about $\sim 20\%$ of the electrons originally obtained from the K layers were back-donated to the intercalate layers during the formation of $x > 4$ compounds. The values obtained from the H model are about 0.07 lower than those obtained from the BR model (using $\gamma_0 = 2.9$ eV). The optical value $f_K \sim 0.80 \pm 0.07$ reported by *Zhang* et al. [4.76] for the $x > 4$ compounds can be compared with other experimental results: $f_K = 0.84$ (NMR) by *Tsang* et al. [4.77], $f_K = 0.88$ (diffuse X-ray scattering) by Quian et al. [4.78], and $f_K = 0.9^{\prime}$ (001 X-ray diffraction studies of c-axis contraction) by *York* and *Solin* [4.72].

Zhang et al. [4.76] carried out Kramers-Kronig analyses using density-scaled graphite for the high-energy data extension (Sect. 4.2.1). Figure 4.25 shows their results for $\varepsilon_2(\omega)$ for the $x = 0$, 1.49, 4.11, and 4.38 compounds. The $\varepsilon_2(\omega)$ data falls as $\sim \omega_p^2/\omega^3$ in the low-energy region, typical of free-carrier absorption, followed first by the threshold for interband absorption, which should contain the $\pi \rightarrow \pi^*$ interband threshold at $\hbar\omega \sim 2E_F$. The broad peak at ~ 4.5 eV is the analog of the M-point peak in graphite at ~ 5 eV, and the strength is reduced in the GIC because of the reduced c-axis density of the carbon layers. In the $x = 1.49$ compound, the M-point peak is further reduced due to surface roughness arising during the removal of the NH_3 from the sample.

The optical evidence cited by *Huang* et al. [4.74] and *Zhang* et al. [4.76] for the transfer of electrons to *localized* states in the $K(NH_3)_x$ layers is the presence in $\varepsilon_2(\omega)$ (Fig. 4.25) of a narrow absorption band at 1.8 eV. This peak is most prominent in the $x = 4.11$ data, where a narrow (~ 0.4 eV) peak (dashed line, modeled as a Lorentzian lineshape) is superposed on the $\pi \rightarrow \pi^*$ threshold (dash-dotted line). In 3D $M(NH_3)_x$ liquids, a band at 0.8eV was observed previously (with the same width) and identified with the $1s \rightarrow 2p$ transition of an electron localized in a "hydrogenic" potential [4.75]. The electron was said to be "solvated" by a cage of NH_3 molecules [4.75]. However, the oscillator strength of the 1.8 eV band found by *Zhang* et al. [4.76] is ~ 4, much larger than found in the 3D metal–NH_3 liquids. They attributed this enhancement of the oscillator strength to a coupling of the "solvated" electrons in the intercalate layers to π^* electrons on adjacent C layers. The oscillator strength of the 1.8 eV band was found to be lower in the $x = 4.38$ compound than in the $x = 4.1$ compound, consistent with the formation of a conduction band from the solvated electron states.

Zhang et al. [4.73] performed a similar in situ optical reflectance study of the ammonia-saturated *stage-2* $K(NH_3)_{4.5}C_{36}$ to see if solvated electrons could also be detected in a *stage-2* $K(NH_3)_x$ GIC. The $K(NH_3)_{4.5}C_{36}$ compound was

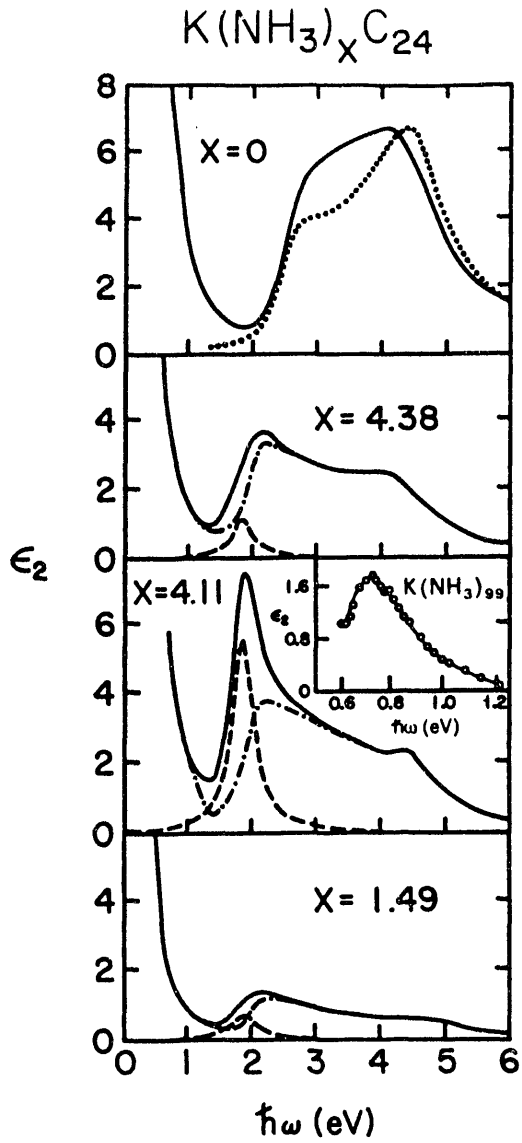

Fig. 4.25. Kramers-Kronig derived $\varepsilon_2(\omega)$ for the $K(NH_3)_xC_{24}$ spectra in Fig. 4.24. The data are shown as the solid lines. The dashed lines represent a Lorentz oscillator, identified with absorption by "solvated" electrons in the $K(NH_3)$ intercalate layers. The dash-dotted line corresponds to the inter-π-band contribution and the data. The dotted line in the upper panel is the calculated inter-π-band contribution [4.24]. The inset to the $x = 4.11$ panel is the absorption band associated with "solvated" electrons in 3D liquid $K(NH_3)_x$ [4.76]

prepared from the reaction of stage-3 KC_{36} with NH_3 at a pressure of ~ 9 atm. The plasma frequencies obtained from a Drude fit to the stage-3 KC_{36} host and stage-2 $K(NH_3)_{4.5}C_{36}$ spectra were found to be $\omega_p = 3.40$ eV and 3.12 eV, respectively, indicating an NH_3-induced redshift $\Delta\omega_p = -0.28$ deV. Using the stage-2 BR model and assuming the K(4*s*) band is empty, *Zhang* et al. [4.73] found that $f_K = (36 + \delta)\, f_C = 0.70 \pm 0.07$, which is somewhat lower than the value $f_K = 0.8$ reported [4.74, 76] for stage-1 $K(NH_3)_{4.1}C_{24}$ and $K(NH_3)_{4.4}C_{24}$ compounds.

Zhang et al. [4.73] also detected a narrow absorption band in the $\varepsilon_2(\omega)$ data for stage-2 $K(NH_3)_{4.5}C_{36}$, which, as in their work in the stage-1 compounds, they correlated with the presence of solvated electrons. Figure 4.26 shows their $\varepsilon_2(\omega)$ data for $K(NH_3)_{4.5}C_{36}$ together with that of the $x = 0$ compound (KC_{36}). For the $x = 4.5$ compound, the figure shows several curves. The solid and dashed curves represent, respectively, the data and the calculated (BR model)

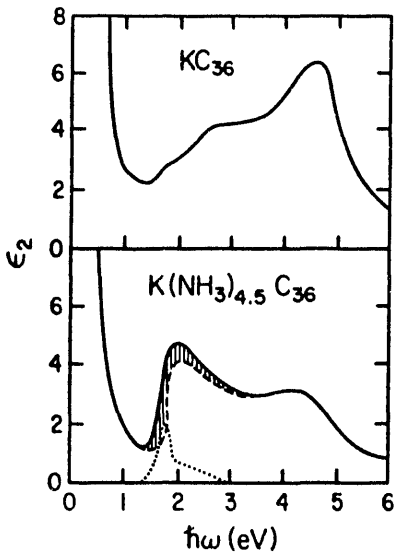

Fig. 4.26. Kramers-Kronig derived $\varepsilon_2(\omega)$ for stage-2 $K(NH_3)_{4.5}C_{36}$ and KC_{36}. The data are shown as the solid lines. The dashed line in the lower panel is the graphitic inter-π-band contribution calculated according to the BR model, and the dotted curve represents the difference between the data and the inter-π-band contribution. The dotted curve peaks at 1.7 eV and is identified with "solvated electrons" in the $K(NH_3)$ layers [4.73]

π, π^* contribution, while the dotted curve represents the difference between these two curves. The dotted curve therefore represents the non-π, π^* contribution. As the figure shows, the non-π, π^* contribution exhibits a narrow, asymmetric peak at 1.7 eV, similar to the peak reported [4.71, 73] at 1.8 eV in the stage-1 $K(NH_3)$ – GICs, suggesting the existence of solvated electrons in the intercalate layers of the stage-2 $K(NH_3)_xC_{36}$ compound.

$K(THF)_xC_{24}$, $x = 1, 2$. *Zhang* and *Eklund* [4.79] also carried out in situ optical studies of stage-1 $K(THF)_xC_{24}$, $x = 1,2$, to investigate the differences in the K(THF) and $K(NH_3)$GICs. Previous studies in the 3D alkali-metal-solvent (MS) liquids have shown NH_3 to be a rather unique solvent [4.80]. The much smaller size and higher dielectric constant of NH_3 (compared with other polar solvents) has been suggested as the origin of the significant differences observed in the physical properties of the 3D MS liquids [4.80]. For example, K readily dissolves in NH_3 to form K^+ ions and solvated electrons, but K does not dissolve in THF. However, *Dye* and coworkers [4.81, 82], used "crown" ethers or "cryptates" as complexing agents to stabilize K^+ in liquid THF and thereby produced solvated electrons, detecting them optically via a narrow absorption band at 0.58 eV.

Stage-1 K(THF) GICs with the nominal stoichiometry $K(THF)_xC_{24}$ (x = 1–3) can be obtained by the reaction of stage-2 KC_{24} with vapors of THF [4.83]. *Zhang* and *Eklund* [4.79] were able to prepare single-stage HOPG-based compounds with $x = 1$ and $x = 2$ for optical study. Figure 4.27 shows their reflectance spectra for $K(THF)_xC_{24}$ ($x = 0, 1, 2$) as solid lines. The dashed lines represent fits to the data calculated according to the stage-1 BR dielectric constant model [4.13] for $\gamma_0 = 2.9$ eV and $\gamma_1 = 0.375$ eV (Sect. 4.2.2a). From the value of the adjustable parameter E_F, *Zhang* and *Eklund* [4.79] determined values for f_K (the charge per K atom in the carbon π^* band) to be $f_K = 0.53 \pm 0.07$ ($x = 1$) and $f_K = 0.49 \pm 0.07$ ($x = 2$). The small difference between the

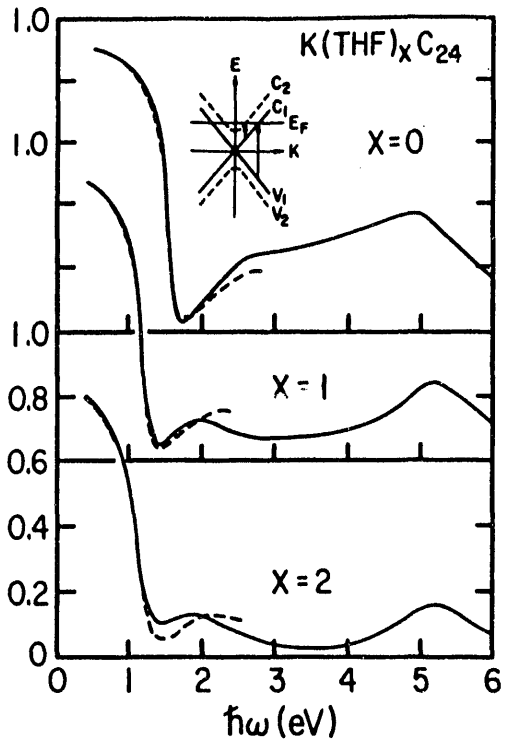

Fig. 4.27. Reflectance ($E \perp c$) for $K(THF)_xC_{24}$. The dashed lines represent BR-model fits to the data [4.79]

values of f_K for the $x = 1$ and $x = 2$ compounds was therefore found to be insignificant. However, the backdonation of electrons $f_B = (1 - f_K)$ to the intercalate layers induced by solvent molecule uptake is larger in the K(THF) GICs than in the $K(NH_3)$ GICs. *Zhang* and *Eklund* [4.79] concluded that this increase in f_B indicated that different chemical mechanisms were responsible for the back-donation in these two GIC systems, and argued that the larger back-donation of electrons to the K(THF) layers was consistent with the insolubility of the K^+ ion in 3D THF liquids.

The values of f_K obtained by *Zhang* and *Eklund* [4.79] for $K(THF)_xC_{24}$ are somewhat lower than values obtained from ^{13}C NMR experiments. Using the NMR chemical shift data of *Quinton* et al. [4.84] and the empirical relation determined by *Tsang* et al. [4.77] that links chemical shift and charge transfer in donor GICs, *Zhang* and *Eklund* [4.79] determined a value for $f_K = 0.81$, similar to the optical values obtained [4.74, 76] for f_K in the stage-1 $K(NH_3)$ GICs. Using their chemical shift data and the BR model for $D(E_F)$, the density of π^* states at the Fermi energy, *Quinton* et al. [4.84] found f_K (ternary) $= 0.72 \pm 0.05$, in better agreement with the optical value.

In contrast to their studies of stage-1 and stage-2 $K(NH_3)C_{24}$ compounds, but consistent with the insolubility of K in THF 3D liquids, *Zhang* and *Eklund* [4.79] found no evidence for the presence of solvated electrons in the $K(THF)_x$ layers; i.e., no narrow absorption band in $\varepsilon_2(\omega)$ was detected.

(d) Cesium-Bismuth and Potassium-Mercury GICs

The $Cs(Bi)_x$ GICs and (KHg) GICs have both been reported to superconduct at temperatures $T > 1$ K. However, several groups have since failed to confirm the

report of superconductivity in the $Cs(Bi)_x$GICs. Both GIC systems exhibit an intercalate layer structure composed of a three-layer sandwich *M-X-M*, where the two outer alkali-metal (*M*) layers are next to the bounding carbon layers. However, the central X = Bi [4.85] or Hg [4.86] layer may be slightly split. Optical reflectance studies of stage-1 and stage-2 $CsBi_x$GICs [4.87] and KHg GICs [4.17, 87–90] have been carried out.

$CsBi_x$-GICs were reported by *Lagrange* et al. [4.91] to superconduct at the following critical temperatures (T_c): stage-1 $CsBi_{0.5}C_4$ (α) (T_c = 4.0 K), stage-1 $CsBi_{1.0}C_4$ (β) (T_c = 2.4 K). However, several groups have failed to observe superconductivity in $CsBi_x$ GICs. [4.88, 92, 93] Even minority phase superconductivity (< 2% volume superconducting) was not detected [4.87] for temperatures $T > 1.5$ K and pressures $p < 7$ kbar, in several stage-1 α- or β-phase samples, although the I_c values agreed to $\pm$ 0.02 Å with those reported by *Lagrange* et al. [4.91]. In the KHg GICs, stage-2 $KHgC_8$ has been reported to superconduct at $T_c \sim 2.0$ K, 1.2 K higher than stage-1 $KHgC_4$, where $T_c \sim 0.8$ K [4.94–96].

Fig. 4.28 shows the optical reflectance data (dotted line) reported by *Yang* et al. [4.86] for the stage-1(α), stage-1(β), and stage-2(β) $CsBi_x$GICs, together with stage-1 and stage-2 (KHg) GICs. The dot-dashed and solid lines in the figure represent, respectively, the high-energy data extension (density-scaled graphite) and the Drude model fit to the data. As can be seen, the Drude fit near the reflectance minimum is well below the data, indicating the presence of low-energy interband transitions near the screened plasma frequency. Above 0.5 eV, the data shown for $KHgC_{4n}$ are in good agreement with the data of *Preil* et al. [4.88, 89] and *Heinz* et al. [4.90]. Below 0.5 eV, *Yang* et al. [4.87] did not

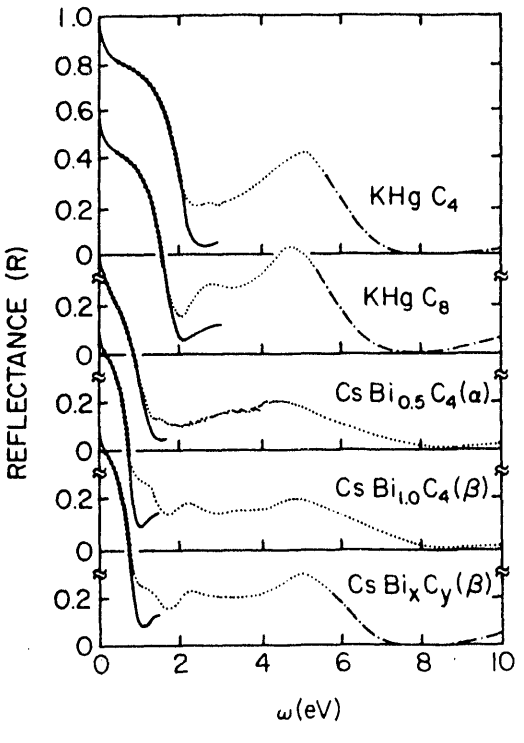

Fig. 4.28. Reflectance ($E \perp c$) for stage-n $KHgC_{4n}$, stage-1 $CsBi_xC_4$ (α and β phases), and stage-2 $CsBi_xC_y$ (β). The solid lines represent Drude fits to the data, and the dash-dotted lines are the data extensions based on density-scaled graphite [4.87]

observe the weak periodic structure reported previously by *Heinz* et al. [4.90]. This periodic structure is likely due to a surface condensate.

Figures 4.29, 30 show the corresponding $\varepsilon_2(\omega)$ data [4.87] obtained by a Kramers-Kronig analysis using density-scaled graphite for the high-energy data extension (Sect. 4.2.1). The $\varepsilon_2(\omega)$ data (dots) are shown together with $\varepsilon_{2,\mathrm{Drude}}$ (solid line) and $\varepsilon_{2,\mathrm{inter}} = \varepsilon_2 - \varepsilon_{2,\mathrm{Drude}}$ (dashed line). *Yang* et al. [4.87] identified the onset of interband absorption in all five compounds with interband transitions involving intercalate states. As they pointed out, the plasma frequencies obtained from Drude analyses of the (KHg) and $CsBi_xGIC$ data are too high for these onsets to be identified with $\pi \rightarrow \pi^*$ transitions. As Fig. 4.29 shows, the onsets for interband absorption in all three $CsBi_xGICs$ occur near $E_{\mathrm{T,i}} = 0.5$ eV (the subscript "i" signifies "intercalate"). For the (KHg) GICs, the onsets are somewhat higher, at $E_{\mathrm{T,i}} = 1.3$ eV. This agrees well with the optical results of

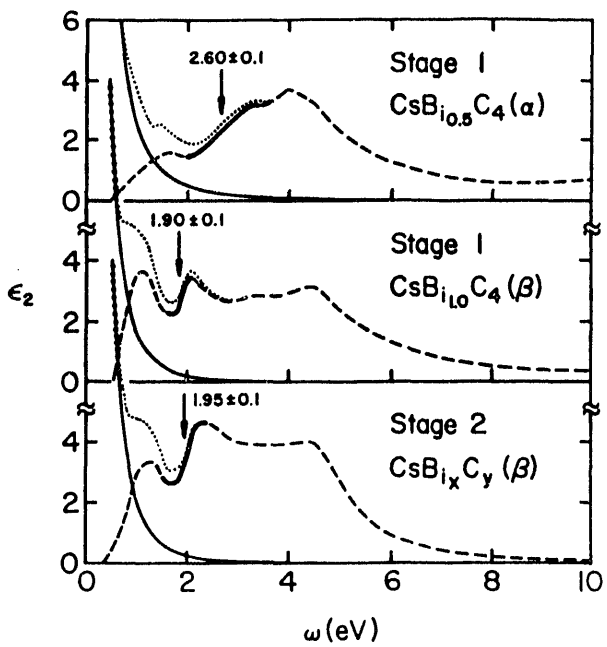

Fig. 4.29. Kramers-Kronig derived $\varepsilon_2(\omega)$ for the CsBi-GIC spectra shown in Fig. 4.28. The dots are the data, the solid line represents the Drude contribution, and the dashed line represents the interband contribution. The inter-π-band thresholds are highlighted with the bold lines, and the arrows indicate their mid points, which are identified with the inter-π-band threshold energy E_{T} [4.87]

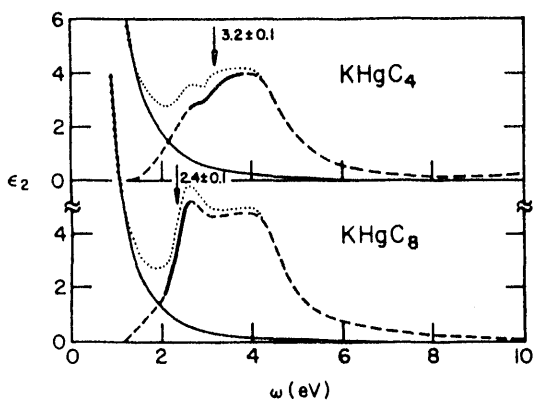

Fig. 4.30. Kramers-Kronig derived $\varepsilon_2(\omega)$ for the KHg-GIC spectra shown in Fig. 4.28. The dots are the data, the solid line represents the Drude contribution, and the dashed line represents the interband contribution. The inter-π-band thresholds are highlighted with the bold lines, and the arrows indicate their mid points, which are identified with the inter-π-band threshold energy E_{T} [4.87]

Preil and *Fischer* [4.89] and *Fischer* et al. [4.17]. The arrows in the figure indicate the midpoint of interband thresholds (highlighted by the bold lines) identified by *Yang* et al. [4.87] with $\pi \rightarrow \pi^*$ interband thresholds. As mentioned earlier, *Shung* [4.67] has shown that these thresholds are broadened about the midpoint $E_T \sim 2E_F$. *Yang* et al. [4.87] interpreted their experimental values for the in-plane plasma frequency ω_p in terms of a two-carrier model, similar to that discussed in Sect. 3.1a for KC_8. Free-carrier contributions to the in-plane plasma frequency were considered from both the carbon π^* ($\omega_{p,\pi}$) and intercalate ($\omega_{p,i}$) bands:

$$\omega_p^2 = \omega_{p,\pi}^2 + \omega_{p,i}^2 = 4\pi e^2[(f_C/\Omega_C m_{opt,\pi}) + (f_i/\Omega_i m_{opt,i})] , \qquad (4.17)$$

where Ω_c and Ω_i refer to the volume per C atom and intercalate unit (i.e., KHg), respectively. The other symbols have their usual meaning (e.g., f_i is the itinerant charge per intercalate unit). For the carbon π^* electrons, *Yang* et al. [4.87] used the BR model to obtain values for $\omega_{p,\pi}$ ($\gamma_0 = 2.9$ eV and $\gamma_1 = 0.375$ eV) from the experimental values for E_F obtained from the midpoints of the inter-π-band thresholds. Then using (4.17) they calculated $\omega_{p,i}$. Finally, by assuming a value for f_i, they calculated $m_{opt,i}$, or vice versa. A significant difference between $CsBi_x$ and KHg GICs emerged from their free-carrier analysis. The intercalate bands in the KHg GICs were found to exhibit a much larger contribution to the free-carrier response than in the $CsBi_x$GICs.

To interpret all their results, *Yang* et al. [4.87] proposed the schematic density of states (DOS) models for the $CsBi_x$ GICs and KHg GICs shown in Figs. 4.31, 32. The interband energies $E_{T,i}$ and $E_{T,\pi}$ are indicated by the arrows in the figures. In the case of the $CsBi_x$ GICs (Fig. 4.31), the Fermi energy E_F is seen to cut through the top of the $CsBi_x$ valence band, as well as the carbon π^* band. For comparison, the inset shows the DOS for $CsBi_{0.33}$ determined from

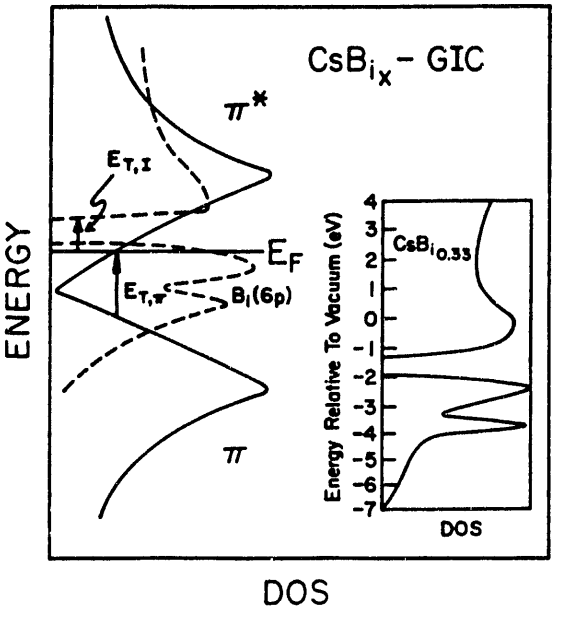

Fig. 4.31. Schematic electronic density of states for CsBi GICs. The inset is from UPS studies of the alloy $CsBi_{0.33}$ [4.87]

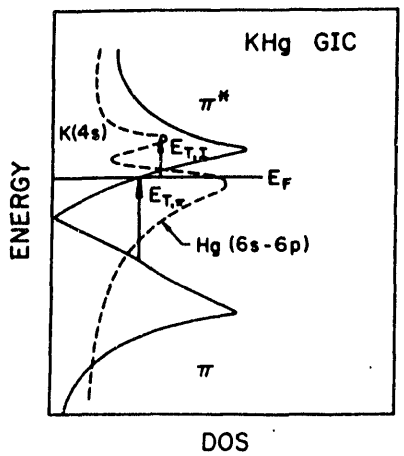

Fig. 4.32. Schematic electronic density of states for KHg GICs [4.87]

photoemission studies by *Spicer* and coworkers [4.97]. The valence bands in $CsBi_{0.33}$ were identified [4.97] as spin-orbit split Bi(6*p*) bands, separated 0.7 eV from a higher lying conduction band.

For the KHg GICs (Fig. 4.32), the schematic DOS model of *Yang* et al. [4.87] has the Fermi energy also cutting both the π^* band and an intercalate band that they have identified as a hybridized Hg(6*s*, 6*p*)–K(4*s*) band. Previous core-level and valence-band photoemission studies of stage-1 and, stage-2 KHg GICs by *DiCenzo* et al. [4.98] reported a greater occupancy of states with K 4*s* character in $KHgC_{4n}$ than in the KC_8 compounds. They also found that the stage-2 $KHgC_8$ compound exhibited a higher occupancy of states with Hg 6*s* character than did stage-1, suggesting that the Hg 6*s* states play an important role in the superconductivity of these compounds.

By assuming that the KHg layer provides 2 (3) electrons per KHg formula unit to fill both the π^* and intercalate conduction band(s), *Yang* et al. [4.87] determined values via (4.17) for the occupation f_i of the intercalate band(s): $f_i = 1.78$ (2.78) for stage-1 and $f_i = 1.75$ (2.75) for stage-2. Therefore, the principal difference between the KHg and $CsBi_x$ GICs obtained from their optical study is that the former compounds have a large fraction of their conduction electrons remaining in the intercalate layers, whereas the latter compounds do not (i.e., $f_i \sim 0.0$–0.15 for the $CsBi_x$ GICs and $f_i \sim 2$–3 for the KHG GICs).

4.3.2 Acceptor-Type GICs

In all cases known to date, the optical properties of acceptor-type GICs are dominated in the 0.5–6 eV range by the dielectric response of the carbon π, π^* bands. The intermolecular coupling does not appear to lead to free carriers in the intercalate layers, and the contribution to the dielectric response from intramolecular or charge transfer absorption has not, in most cases, been found to be significant. The optical determination of charge transfer in acceptor GICs then reduces to measuring the in-plane plasma frequency $\omega_p = \omega_{p,\pi}$ and using an appropriate π-band model to convert $\omega_{p,\pi}$ into f_C. Since most acceptor GICs

have moderately small charge transfer, the rigid-band model of Blinowski-Rigaux [4.13] (and the associated dielectric functions) can be used to determine f_C and E_F in stage-1 and stage-2 compounds. Consistent with this picture, acceptor-type GICs are found to exhibit a much higher electrical and thermal anisotropy than donor-type GICs.

Below we review optical studies of acceptor-type GICs that have resulted in the determination of the charge transfer or the effects of charge transfer on the graphitic intralayer phonons. Some of the results have been summarized recently by *Rigaux* [4.3]. All the optical data discussed below were collected from the *c* face (*ab* plane) of HOPG host material.

(a) Sulfuric Acid GICs

Perhaps the most important optical studies of charge transfer in acceptor-type GICs have been carried out on H_2SO_4 GICs. These compounds can be prepared electrochemically, and the charge flowing in the external circuit can be used to determine the hole population in the carbon π band(s). A low current (10–50 microamps) is passed between a graphite (HOPG) electrode (+) and Pt counter electrode (−) in a cell containing H_2SO_4 to drive the reaction slowly forward. As time progresses, the graphite electrode evolves through a succession of well-staged GICs (. . . $4 \rightarrow 3 \rightarrow 2 \rightarrow 1$). Electrochemical techniques used to prepare other GICs (including donor-type GICs) have recently been reviewed by *Eklund* [4.99].

The electrochemical reaction of graphite with concentrated H_2SO_4 has been proposed by *Aronson* et al. [4.100] and *Bessenhard* et al. [4.101] to lead to the stoichiometry $C_p^+ HSO_4^- (H_2SO_4)_x$ for $p > 21$. A rather unique property of these GICs is the existence of a series of stage-1 ($21 < p < 28$) and stage-2 ($48 < p < 60$) compounds with continuously variable charge transfer. In these ranges of p, charge transfer has been identified [4.101] with the electrochemical conversion of neutral H_2SO_4 into ionized HSO_4^-, i.e., only protons need to be removed from the I layers to increase f_C. According to the electrochemical model for these GICs [4.100, 101], each HSO_4^- molecule in the intercalate layer is linked to both one hole in the carbon layers and to one electron flowing in the external electrochemical circuit. Therefore, f_C can be determined from the net charge Q passed in the electrochemical circuit; i.e., $f_C = 1/p = m_C Q/eM$, where e is the electronic charge, M is the mass of the graphite host, and m_C is the mass of a carbon atom.

The first in situ optical study of $C_p^+ HSO_4^- (H_2SO_4)_x$ was performed by *St. Jean* et al. [4.102]. The sample was only partly immersed in the acid, so that the light was incident on the sample above the acid level. Later, Raman scattering experiments by *Eklund* et al. [4.103] showed that at certain times during the electrochemical intercalation process, even the stage indexes of the sample above and below the acid level were different. However, during the variable p and fixed stage-1 and stage-2 intervals, the Raman studies [4.103] showed that sample surfaces above and below the acid level exhibited the same

spectra. This observation is undoubtedly connected with the high mobility of protons in the intercalate layers. To characterize the stage index of their samples in the optical skin depth, *St. Jean* et al. [4.102] monitored optical structure in the infrared range, which they identified with inter-π-band ($v \rightarrow v$) band transitions. Their assignment of some of the observed infrared structure has been questioned [4.104] and will be discussed below. From their interpretation of the infrared structure, *St. Jean* et al. [4.102] reported that uniform stage-2 and stage-1 phases extended over the charge transfer interval corresponding to $C_{58}^{+} \rightarrow C_{48}$ (stage-2) and $C_{28}^{+} \rightarrow C_{21}^{+}$ (stage-1), in good agreement with the earlier results of *Bessenhard* et al. [4.101]. Recording several reflectance spectra during these variable charge transfer intervals, they observed a continual blueshift in the Drude edge with decreasing p. *St. Jean* et al. [4.102] fit their spectra to the stage-1 and stage-2 dielectric function models of *Blinowski* et al. [4.13] to determine values for E_F as a function of p. These data were used to deduce the first experimental values for the intralayer transfer integral (γ_0). From the BR model (4.9).

$$p = 1/f_C = \gamma_0 \pi \sqrt{3}/E_F^2 \,. \tag{4.18}$$

This behavior was indeed observed in both the stage-1 and stage-2 graphite-H_2SO_4 compounds by *St. Jean* et al. [4.102], and is shown in Fig. 4.33, where the quantities pE_F^2 (crosses) and pE_F (dots) are plotted against $p(p = x$ in their figure). Values for $\gamma_0 = 2.63 \pm 0.03$ eV (stage 1) and $\gamma_0 = 2.81 \pm 0.04$ eV (stage 2) were determined from the data. The stage-1 value appears to be somewhat lower than the typical range of values 2.8–3.0 used in a variety of later optical studies.

As part of a series of studies on the graphite-H_2SO_4 system that included neutron diffraction [4.105, 106] and Raman scattering [4.107, 108], *Zhang* et al. [4.104] also performed in situ optical reflectance measurements on the stage-1

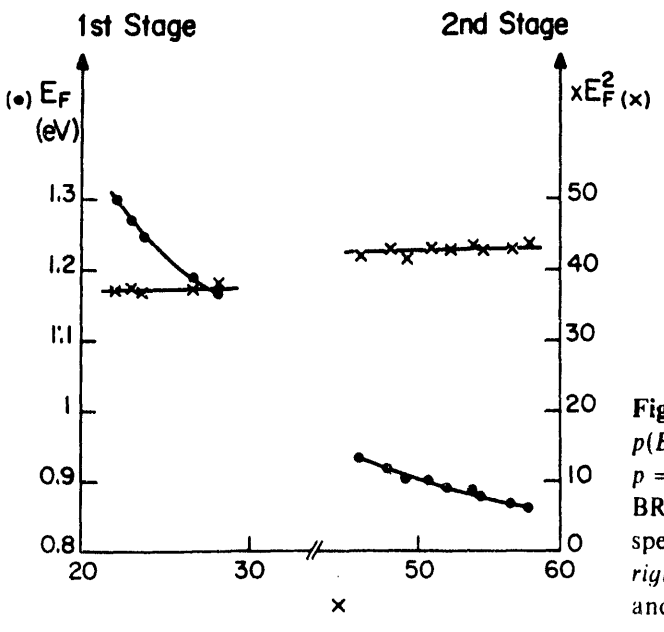

Fig. 4.33. Plot of E_F (dots, left scale) and $p(E_F)^2$ (crosses, right scale) against p, where $p = x = 1/f_C$. The data were obtained from BR-model fits to the reflectance ($E \perp c$) spectra for $C_p^{+}(HSO_4)^{-} \cdot H_2SO_4$. In the *rigid* π-band model, $p(E_F)^2$ is a constant and is proportional to γ_0 [4.102]

sample surface. The dip in $R(\omega)$ in the stage-2 spectra of *St. Jean* et al. [4.102] is $\sim 40\%$, almost a factor of ten larger than the 3–5% dip in the reflectance observed at 0.375 eV by *Hoffman* et al. [4.110] in stage-2 graphite-$SbCl_5$ and by *Smith* and *Eklund* [4.111] in stage-2 graphite-$FeCl_3$.

Zhang et al. [4.104] carried out Drude analyses of their data for the low- and high-charge transfer forms of stage-1 and stage-2 graphite-H_2SO_4 (i.e., C_{28}^+, C_{21}^+, C_{60}^+, and C_{48}^+). They obtained $\omega_p = 3.31, 3.06, 3.10$, and 2.90 eV, respectively, for the $p = 21$, 28, 48, and 60 compounds. As *St. Jean* et al. [4.102] had done previously, *Zhang* et al. [4.104] used the BR model to convert the experimental plasma frequencies into values for γ_0. However, in contrast to the results of *St. Jean* et al. [4.102], they found γ_0 to be nearly stage-independent, reporting an average value for $\gamma_0 = 2.9$ eV.

For comparison with these values obtained for γ_0, Shubnikov-de Haas (SdH) experiments by *Zaleski* et al. [4.112, 113] on stage-1 and stage-2 graphite-$SbCl_5$ found orbit areas in good agreement with the charge transfer values obtained optically by *Hoffman* et al. [4.110] using $\gamma_0 = 2.9$ eV. Furthermore, the H model and the BR model can be brought into good agreement with each other (at low charge transfer), if the value $\gamma_0 = 2.93$ eV is used in the BR model. Also note that a BR-model analysis of the optical reflectance of KC_{24} is consistent with complete charge transfer of the K 4*s* electron to the carbon layers – if the value $\gamma_0 = 2.9$ eV is used in the data analysis [4.57].

Eklund et al. [4.103] examined the charge transfer dependence of the Raman-active E_{2g} graphitic intralayer phonons in the graphite-H_2SO_4 system. Figure 4.35 shows their results for the charge transfer dependence of the mode fre-

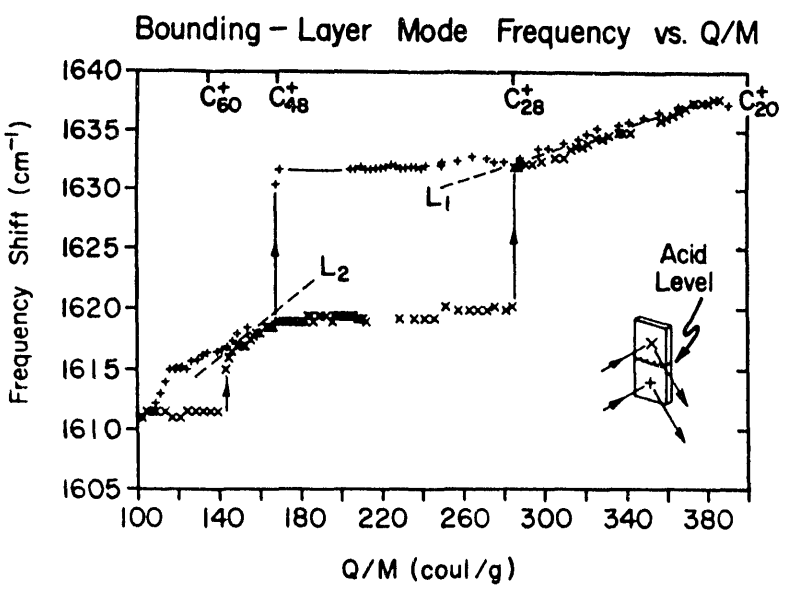

Fig. 4.35. Raman-active E_{2g} graphitic intralayer phonon frequency against Q/M for the stage-1 and stage-2 graphite-H_2SO_4 compounds ($Q/M \propto f_C$). The (×) and (+) symbols represent data taken above and below the acid level, respectively. The lines L1 and L2 determine the charge transfer dependence of the bounding layer mode frequency for the stage-1 and stage-2 compounds [4.105]

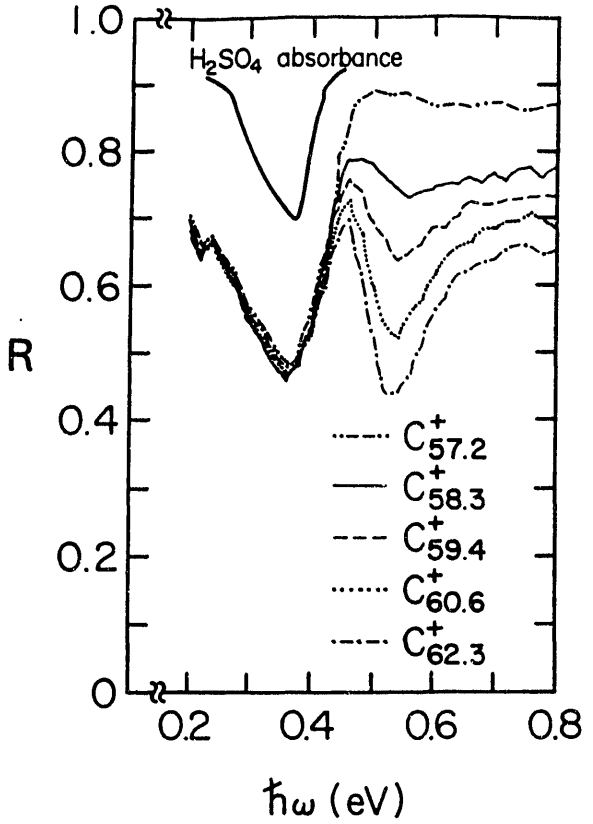

Fig. 4.34. The low-energy reflectance of graphite H_2SO_4 for values of the electrochemical charge near the stage 3 to 2 transition. The feature at 0.57 eV in the GIC spectra is identified with $v \rightarrow v$ interband absorption in the stage-3 GIC. The upper trace is the characteristic absorbance of liquid H_2SO_4. The 0.38 eV feature is identified with absorption in H_2SO_4, which masks the weaker stage-2 $v \rightarrow v$ absorption at 0.375 eV [4.76]

and stage-2 $C_p^+HSO_4^-(H_2SO_4)_x$ compounds in the energy range 0.2–6.0 eV. Figure 4.34 shows the reflectance spectra (reported by *Zhang* et al. [4.104] in the low-energy region ($E < 0.8$ eV) for several spectra near the stage $3 \rightarrow 2$ transition at $p = 60$. A prominent feature in the spectra is at 0.38 eV (which remains unchanged throughout the range of p studied). Another at 0.57 eV disappears near C_{60}^+ compound, in agreement with the previous work of *St. Jean* et al. [4.102]. The top trace in the figure is the absorbance spectrum obtained by *Giguere* and *Savoie* [4.109] of liquid H_2SO_4, which also exhibits structure at 0.38 eV. The 0.57 eV feature, identified previously by *St. Jean* et al. [4.102] with $v \rightarrow v$ interband absorption in the stage-3 compound, is similar in strength and position to the $v \rightarrow v$ structure observed, for example, in graphite-$SbCl_5$ by *Hoffman* et al. [4.110] and in graphite-$FeCl_3$ by *Smith* and *Eklund* [4.111]. In Fig. 4.34, the disappearance of the 0.57 eV feature in the data of *Zhang* et al. [4.104] at $p = 60$ agrees with the previous reflectance studies of *St. Jean* et al. [4.102] and accords with Raman scattering studies [4.103] of the evolution of the graphitic intralayer modes in this GIC system. However, the much stronger 0.38 eV structure in the figure, identified previously by *St. Jean* et al. [4.102] with stage-2 $v \rightarrow v$ interband transitions and reported by them to disappear at the end of the stage-2 interval, was found by *Zhang* et al. [4.104] to remain in the stage-1 spectra, growing in strength. *Zhang* et al. [4.104] were then forced to conclude that this structure should be identified with intramolecular optical absorption in H_2SO_4, either within the intercalate layers or in a thin film on the

quency. The experiments were carried out in situ in the electrochemical cell with the HOPG-based samples half submerged in H_2SO_4, with the upper half in N_2 gas. The data in the figure indicated by (+) and (×) were taken, respectively, with the laser radiation incident on the acid/sample and the N_2 gas/sample interface. As mentioned earlier, the data coincide in the regions of constant stage index and variable charge transfer ($60 < p < 48$, stage-2, and $28 < p < 21$, stage-1). In these fixed-stage regions, the phonon frequency exhibits a linear dependence on $Q/M \propto f_C$. From the slopes of the lines L1 and L2 in the figure, *Eklund* et al. [4.103] obtained $d\omega_{2g}/df_C = 460 \pm 30\ \mathrm{cm}^{-1}$ (stage 1) and $d\omega_{2g}/df_C = 1050 \pm 120\ \mathrm{cm}^{-1}$ (stage 2). Thus the E_{2g} mode frequency dependence on charge transfer is given by

$$\text{Stage 1:}\quad \omega_{2g}(\mathrm{cm}^{-1}) = \omega_{2g0} + (460 \pm 30) f_C\,, \tag{4.19a}$$

$$\text{Stage 2:}\quad \omega_{2g}(\mathrm{cm}^{-1}) = \omega_{2g0} + (1050 \pm 120) f_C\,, \tag{4.19b}$$

where $\omega_0 = 1615$ and $1635\ \mathrm{cm}^{-1}$, for stages 2 and 1, respectively. Note that these values for ω_{2g0} are strictly applicable only for stage-1 and stage-2 graphite H_2SO_4. Other acceptor-type GICs might exhibit a stronger (or weaker) *c*-axis coupling between the C and I layers, which might influence ω_{2g0}. However, the values they obtained for the derivatives ($d\omega_{2g}/df_C$) in H_2SO_4 might be expected to be more generally applicable to other acceptor-type GICs. In this regard, *Ohana* et al. [4.114] have used the derivative values to interpret the effects of charge transfer in metal-fluoride GICs. We discuss this further below.

Finally, we mention briefly the results of in situ studies by *Rao* et al. [4.115] of the infrared-active (E_{1u}) $\sim 1600\ \mathrm{cm}^{-1}$ modes in graphite-H_2SO_4 during electrochemical intercalation ($\infty < p < 24.3$). Although they did not carry out a detailed line-shape analysis for these intralayer graphitic modes, they obtained a few interesting results. First, they noted a clear *upshift* in the E_{1u} mode frequency as the stage index decreased from stage $4 \rightarrow 3$, followed by a clear *downshift* in the E_{1u} mode frequency at the stage $3 \rightarrow 2$ transition. The stage $3 \rightarrow 2$ *downshift* contrasts with the *upshift* reported previously by *Gualberto* et al. [4.116] in graphite-$AlCl_3$, but is consistent with the results of *Eklund* et al. [4.117] in graphite-$SbCl_5$ and *Underhill* et al. [4.27] in graphite $FeCl_3$. *Rao* et al. [4.115] suggested that these results, taken collectively, indicate that both intralayer and interlayer force constants have a significant effect on the frequencies of the infrared- and Raman-active graphitic modes. This point of view is further strengthened by the observation [4.115] that the stage-2 E_{1u}-mode frequency remained constant during the stage-2 $p = 28 \rightarrow 21$ interval, whereas the E_{2g} mode frequency upshifted by $5\ \mathrm{cm}^{-1}$ [4.103, 105]. *Rao* et al. [4.115] therefore concluded that a theory for the charge transfer dependence of the $\sim 1600\ \mathrm{cm}^{-1}$ mode frequencies must also include *c*-axis force constants, i.e., the change in the graphitic intralayer mode frequency is not just a simple consequence of charge-transfer-induced expansion or contraction of the in-plane C–C bond length. This conclusion agrees with the theoretical results of *Chan* et al. [4.29].

(b) Metal-Chloride GICs

$SbCl_5$ and $FeCl_3$ GICs. Because of its stability in air [4.5], graphite-$SbCl_5$ is one of the most heavily studied acceptor-type GICs. The compounds can be prepared by the reaction of the Lewis acid $SbCl_5$ with graphite. By analogy with the disproportionation chemistry suggested for graphite-AsF_5 by *Bartlett* et al. [4.118], the intercalation chemistry of graphite-$SbCl_5$ has been described in terms of the disproportionation of $SbCl_5$ into $SbCl_3$ and $SbCl_6^-$, although various concentrations of reaction products or adducts (e.g., $SbCl_5$, $SbCl_6^-$, $SbCl_3$, $SbCl_4^-$, and $SbCl_5 . SbCl_6^-$) [4.119–122] have been proposed to reside in the intercalate layers, depending on the details of the sample preparation.

High-resolution, scanning transmission electron microscopy studies of stage-4 graphite-$SbCl_5$ by *Hwang* et al. [4.123] found clear evidence for segregated phases of differing Sb/Cl stoichiometry in the intercalate layers. Islands with average stoichiometry $SbCl_{3.2}$ accounted for 11% of the area and were found amidst a sea of $\sqrt{7} + \sqrt{7}\,(R°19.1)$ material with an average stoichiometry $SbCl_{7.2}$. The islands were observed to be 500–1000 Å in diameter and did not exhibit crystalline order. *Hwang* et al. [4.123] suggested that the various species of $SbCl_x (x = 3, 4, 5, 6)$ could be distributed in the I layer to obtain an equal charge per unit area in both the sea and the island regions.

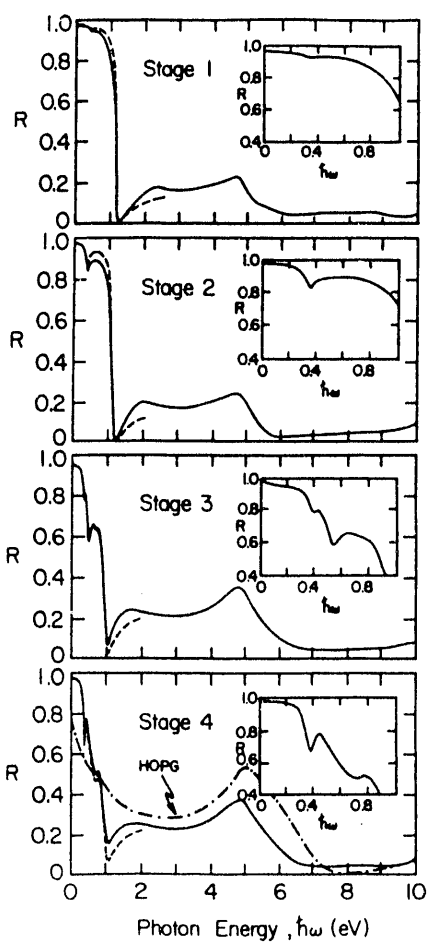

Fig. 4.36. Reflectance ($E \perp c$) for stages 1–4 graphite $SbCl_5$. The dashed lines represent Drude fits to the data. The inset to each figure magnifies the region associated with $v \rightarrow v$ interband absorption. The spectrum of HOPG is also shown in the bottom panel [4.110]

The optical properties of stages 1–4 graphite-$SbCl_5$ were first studied in detail by *Hoffman* et al. [4.110], who measured the optical reflectance over the energy range 0.08–10 eV. Figure 4.36 shows the spectra of stages 1–4 graphite-$SbCl_5$ from their study. The dashed lines represent fits to the respective spectra using a Drude–Lorentz model (4.15), with the Lorentz oscillators representing low energy ($v \rightarrow v$) absorption between nearly parallel valence (π) bands. The spectra in the figure agree well with those reported earlier by *Eklund* et al. [4.124] in the energy range 0.2–2.5 eV. Each spectrum exhibits features characteristic of acceptor-type GICs, including the low-energy ($E < 0.6$ eV) structure associated with $v \rightarrow v$ inter-π-band absorption (except stage 1), a sharp Drude edge located near ~ 1 eV, and the analog of the pristine graphite M-point peak at ~ 5 eV. The weak feature at 0.38 eV in the stage-1 spectrum was attributed by *Hoffman* et al. [4.110] to a small inclusion of stage-2 material in the optical skin depth.

A Kramers-Kronig analysis of the reflectivity using density-scaled graphite (Sect. 4.2.1) was used to obtain ε_1 and ε_2. The reflectance and $(\omega\varepsilon_2)^{-1}$ were both fit to the Drude-Lorentz model to determine the Drude parameters. Figure 4.37 shows the results obtained by *Hoffman* et al. [4.110] for the $v \rightarrow v$ interband contribution to the dielectric function $\varepsilon_{2,\text{bound}} = \varepsilon_{2,\text{inter}} = \varepsilon_2(\omega) - \varepsilon_{2,\text{Drude}}$. The solid lines represent the oscillator fit to the data, and the center frequency of

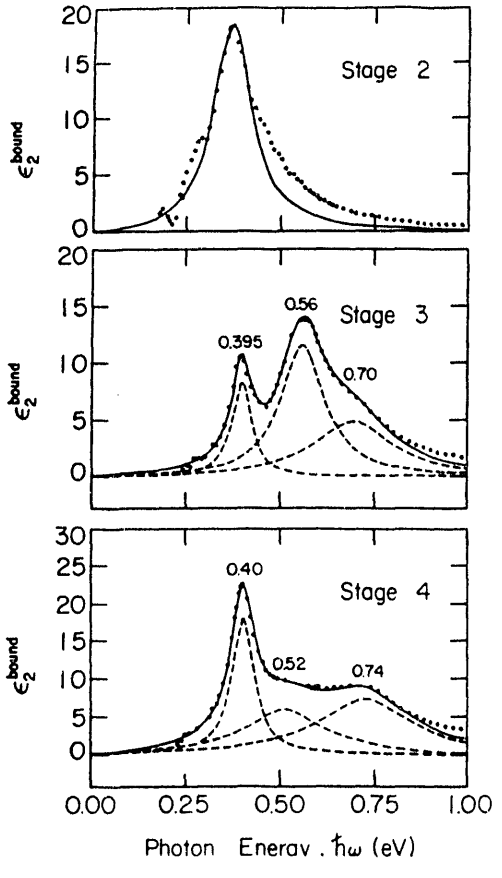

Fig. 4.37. $v \rightarrow v$ inter-π-band absorption for stages 2–4 graphite $SbCl_5$. The data (dots) were obtained from a Kramers-Kronig analysis of the spectra in Fig. 4.36. The solid lines represent Lorentz oscillator fits to the $v \rightarrow v$ structure [4.110]

each oscillator determines the splitting between various valence (π) bands. Without making contact with an energy-band model, such as was done by *Yang* and *Eklund* [4.24] in the KC_{12n} compounds, information regarding the net layer charge distribution in stage-3 and stage-4 graphite-$SbCl_5$ cannot be obtained. However, from the inter-π-band structure at ~ 0.6 eV in both these GIC systems, the electrostatic band parameter 2δ(SK model, Sect. 4.2.2c), which controls the distribution of net layer charge between the interior and bounding layers, appears to have nearly the same value in graphite-$SbCl_5$ and graphite-K.

The systematics of the free-carrier contribution to σ_{opt} in *high-stage* acceptor-type GICs were examined in graphite-$SbCl_5$ and graphite-$FeCl_3$ by *Hoffman* et al. [4.110]. They proposed an independent layer model in which all the charge from the intercalate layer was considered to be transferred to the bounding carbon layers. The interior layers remained graphitic (i.e., they exhibited a plasma frequency $\omega_p = 0.44$ eV equal to that of pristine graphite [4.16]). In their model, the effective plasma frequency ω_p is due to a sum of contributions from the bounding (C_b) and interior (C_i) carbon layers, leading to the expression [4.110]

$$\omega_p^2 = \frac{(n-2)\Omega_i^2 + 2\Omega_b^2}{D/d_C + n}, \tag{4.20}$$

where $l_c = D + nd_C$ is the distance between intercalate layers, d_C and D are the thickness of a carbon and an intercalate layer, and Ω_i and Ω_b are, respectively, the plasma frequency of the C_i and C_b layers. Figure 4.38 shows the fit of the independent layer model of *Hoffman* et al. [4.110] to the data for graphite-$FeCl_3$ [4.111] and graphite-$SbCl_5$. The data are plotted as ω_p^2 vs reciprocal stage index ($1/n$), and the solid lines in the figure were calculated according to (4.20) using stage-independent parameters: $\Omega_i = 0.44$ eV [4.16], $D(FeCl_3) = 6.09$ Å, and $D(SbCl_5) = 6.02$ Å. The values of $\Omega_b(FeCl_3)$ and $\Omega_b(SbCl_5)$ were chosen to fit

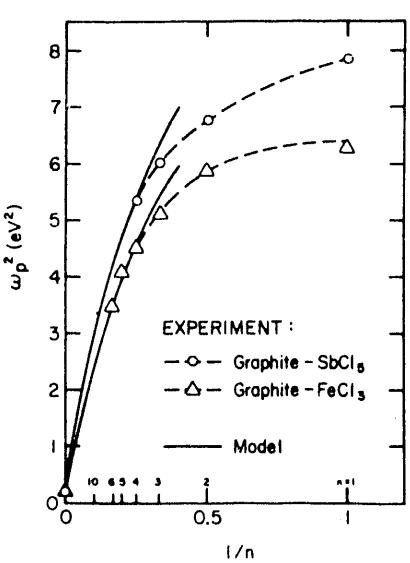

Fig. 4.38. Plot of ω_p^2 against the reciprocal stage index ($1/n$) for graphite $FeCl_3$ and graphite $SbCl_5$. The solid lines are calculated from the independent layer model described in the text. The dashed lines are guides for the eye [4.110]

the $n = 4$ data. As the figure shows, the model performs reasonably well for the intended high stage index region (i.e., stage $n \leqslant 4$), but underestimates the plasma frequency for lower stage index compounds.

Hoffman et al. [4.110] used the BR model to convert the experimental values of the plasma frequency into values for f_C. For the stage-1 $SbCl_5$, they determined $f_C = 0.033 \pm 0.005$ using $\gamma_0 = 3.0 \pm 0.1$ eV holes per C atom. From the reported range of stoichiometry $C_{12-14}SbCl_5$ [4.125, 126], this value of f_C translates into 0.43 ± 0.1 holes per intercalated $SbCl_5$. However, if complete disproportionation occurs ($3SbCl_5 \rightarrow 2SbCl_6^- + SbCl_3$ [4.118]), 2/3 of a π-band hole per intercalated $SbCl_5$ is anticipated. Thus *Hoffman* et al. [4.110] deduced that the disproportionation is 71% complete in the stage-1 compound. Results of Shubnikov-de Haas experiments on stage-1 graphite-$SbCl_5$ reported by *Zaleski* et al. [4.112], which yield the charge transfer directly from the orbit area, found 0.37 holes per intercalated $SbCl_5$, in good agreement with the optical results of *Hoffman* et al. [4.110]. For the stage-2 compound, using a BR-model analysis of their data ($\gamma_0 = 3.0 \pm 0.1$ eV and $\gamma_1 = 0.375$ eV), they obtained $f_C = 0.013 \pm 0.003$, or 0.34 ± 0.1 holes per intercalated $SbCl_5$ – i.e., $\sim 50\%$ disproportionation, where we have corrected their reported value for f_C using (4.9). These stage-2 values for f_C also agree well with the SdH results of *Zaleski* et al. [4.113].

(c) Fluorine and Metal-Fluoride GICs

Fluorine and metal-fluoride GICs have received a great deal of attention recently because the conductivities of some of these compounds rival that of copper. The relationship between the conductivity and the charge transfer in these compounds is therefore of special significance. In this section, we examine the results of several studies that have attempted to deduce optically the charge transfer in fluorine or metal fluoride GICs.

Graphite-AsF_5. Graphite-AsF_5 is the most conductive of the GIC synthetic metals with the electrical conductivity of the stage-2 material comparable to that of copper [4.127]. The compound also exhibits one of the largest electrical anisotropies reported for GICs [4.128], i.e., $\sigma_a/\sigma_c > 10^6$. *Fachini* et al. [4.129] interpreted their NMR data to indicate that the charge transfer in grahite-AsF_5 is a function of temperature, but this result conflicts with optical data presented below.

St. Jean et al. [4.130] preformed optical studies of f_C in the stage-1 and stage-2 $C_{8n}AsF_5$ compounds over the energy range 0.5–2.2 eV, and at temperatures $T = 300$ K, 77 K, and 10 K. The positions of the Drude minimum in the stage-1 and stage-2 compounds (at $T = 300$ K) agree well with those reported previously by *Hanlon* et al. [4.131]. Furthermore, *St. Jean* et al [4.130] found the position of the Drude edge to be *temperature-independent*, direct evidence that f_C does not exhibit significant temperature dependence, and in sharp contrast to the NMR study [4.129] of *Fachini* et al. *St. Jean* et al. [4.130] fit their stage-1 and stage-2 reflectance data at $T = 300$ K using the dielectric function model of

Blinowski et al. [4.13]. They obtained $E_F = 1.28$ eV, $\tau = 5 \times 10^{-14}$s for stage 1, and $E_F = 1.02$ eV, $\tau = 5 \times 10^{-14}$s for stage 2. Using the values of $\gamma_0 = 2.6$ eV (stage 1) and $\gamma_0 = 2.8$ eV (stage 2) obtained from their study of graphite-H_2SO_4 [4.102], they calculated that $f_C = 0.41$ and 0.53 for stages 1 and 2, respectively, agree with the observation σ_a (stage 1) $< \sigma_a$ (stage 2). Furthermore, they found their f_C value for stage 2 to agree with the results of *Weinberger* et al. [4.132], who interpreted their Pauli spin susceptability data within the framework of the BR model. Results for f_C from SdH studies on stage-1 graphite-AsF_5, also interpreted within the BR model [4.13], are in good agreement: *Markiewicz* et al. [4.133] ($f_C = 0.41$) and *Fischer* [4.128] ($f_C = 0.42$).

Graphite-MF_6(M = Os, Mo). The nature of the interaction between the graphite host and the intercalant species has been found to vary with the oxidizing strength of the intercalant species. For instance, weakly oxidizing species display an electrostatic interaction with the C layers in the GIC, leaving itinerant holes in the carbon π bands. *Henning* [4.134] has pointed out that strongly oxidizing intercalant species have a tendancy to bond covalently with the carbon layers, creating a localized charge at the site of the covalent bond.

Two stage-1 metal-fluoride GICs that have similar stoichiometries, but stem from intercalants with much different oxidizing strengths, are stage-1 $C_x(Os)F_6$ and stage-1 $C_x(Mo)F_6$, where $8 < x < 11$. The charge transfer in these compounds was examined by *Ohana* et al. [4.114] and *Vaknin* et al. [4.135]. They carried out a series of experiments sensitive to the free holes in the C layers (optical reflectance) [4.114] as well as the localized charge in the intercalate layers (electron-spin resonance and magnetic susceptibility) [4.135].

The reflectance spectra of C_xMoF_6 and C_xOsF_6 were collected by *Ohana* et al. [4.114] at room temperature over the energy range 0.8–3.0 eV. The data were fit with the BR model with $\gamma_0 = 3.0 \pm 0.3$. For C_xOsF_6, they found $f_C = 0.035 \pm 0.003$ with $\tau = 1.8\,\text{eV}^{-1}$ (7.44×10^{-15}s), while the C_xMoF_6, $f_C = 0.029 \pm 0.003$ and $\tau = 4\,\text{eV}^{-1}$ (1.65×10^{-14}s). *Vaknin* et al. [4.135], using ESR and magnetic-susceptibility measurements to determine the charge on the molecular species in the intercalate layer, reported that in stage-1 C_xOsF_6 there is a charge of nearly one electron residing on each intercalate molecule (i.e., $f_M = 1$). On the other hand, in stage-1 C_xMoF_6 they found $f_M = 0.2$ electrons per molecule, much lower than found for the C_xOsF_6 compound. These values of $f_M = (1 - xf_C)$ can be compared with the optical values of *Ohana* et al. [4.114], who assumed that $x = 9$: $f_M = 0.261$ (C_9MoF_6) and 0.315 (C_9OsF_6). Thus, for C_xMoF_6, the optical, ESR, and magnetic-susceptibility results are in apparent agreement for f_M. However, there is noteworthy disagreement between the f_M values obtained by these experimental techniques for C_xOsF_6 (i.e., $\Delta f_M \sim 0.7$). This was attributed [4.114] to the formation of covalent bonds, so that the electrons transferred to the I layers did not leave itinerant holes behind in the C layers, but rather electrons localized in covalent bonds. While this explanation seems plausible, the size of the discrepancy is quite large, suggesting that C_xOsF_6 might exhibit significant covalent bonding between the C and I

layers – so that the BR model might not be a good description under these circumstances.

Note that in both C_xMoF_6 and C_xOsF_6, the free-carrier lifetimes τ observed by *Ohana* et al. [4.114] are quite short for GICs (i.e., $\tau = 1.8 - 4\,\mathrm{eV}^{-1}$), consistent with the formation of a significant density of covalent C–I bonds. These bonds, of course, introduce in-plane disorder in the C layers, which is known [4.2] to "turn on" the disorder-induced Raman scattering feature at $1360\,\mathrm{cm}^{-1}$, as observed by *Ohana* et al. [4.114] for the C_xOsF_6 compound.

Ohana et al. [4.114] also made a determination for f_C via the frequency of the Raman-active E_{2g} phonon frequency. Using the result expressed in eq. 17a, obtained by *Eklund* et al. [4.105] for stage-1 graphite-H_2SO_4, they obtained a value for the difference Δf_C in charge transfer between C_xOsF_6 and C_xMoF_6 in agreement with their optical results. However, this approach assumes that ω_{2g0} is the same for both compounds, an assumption that should be questioned because the two materials appear to have quite different c-axis coupling between the C and I layers.

Fluorine and BF_3GICs. The onset of covalent bond formation in carbon-fluoride compounds was studied optically by *Ohana* et al. [4.7] by examining the optical reflectance spectra of a series of compounds with increasing fluorine concentration. A series of air-stable compounds C_xF with $3.3 < x < 9.0$ were produced by the reaction of graphite (HOPG) with dilute HF + F_2 gas (1:1). *Ohana* et al. reported that stage-2 C_xF compounds with variable charge transfer can be obtained over a wide range of x, i.e., $4 < x < 8$. Thus this situation is similar to the stage-2 graphite-H_2SO_4 compounds, where a particularly simple electrochemical model allows the direct determination of the charge transfer from the charge passed in the reaction (Sect. 4.3.2a). The mixtures stage-1/stage-2 and stage-2/stage-3 were obtained, respectively, for $x < 4$ and for $x > 8$.

Ohana et al. [4.7] recorded optical reflectance spectra for the C_xF compounds over the energy range 0.8–3.2 eV, and carried out Drude analyses to determine the plasma frequency as a function of fluorine concentration ($1/x$). In the single-phase, stage-2 region, the data were analyzed using the BR model ($\gamma_0 = 3.0$ eV and $\gamma_1 = 0.375$ eV) to obtain values for E_F and f_C. The plasma frequency in the stage-2 region exhibited a maximum value for $1/x \sim 0.16$ (Fig. 4.39) near the middle of the concentration range. The Fermi energy E_F also exhibited unusual behavior in this range of concentration, first falling slightly and then rising with increasing ($1/x$).

This unusual behavior was fit [4.7] to a two-acceptor-state model. For $x > 6$ *Ohana* et al. proposed the existence of one acceptor level with energy $E_1 = -1.034$ eV. For $x < 6$ they proposed the existence of two acceptor levels, one at the previous energy, and a second at $E_2 = -0.84$ eV. The model appears to fit the $1/x$ dependence of f_C reasonably well (Fig. 4.40). Of course, the proper application of the BR model to these particular stage-2 compounds presumes that a significant number of covalent bonds have not been formed between the

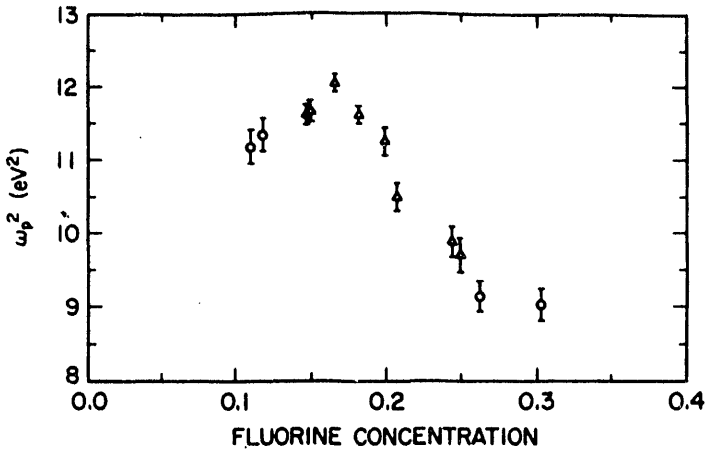

Fig. 4.39. Plot of ω_p^2 against fluorine concentration $(1/x)$ in the stage-2 CF_x compounds. The unusual behavior was interpreted in terms of an x-dependent, two-level acceptor stage model [4.7]

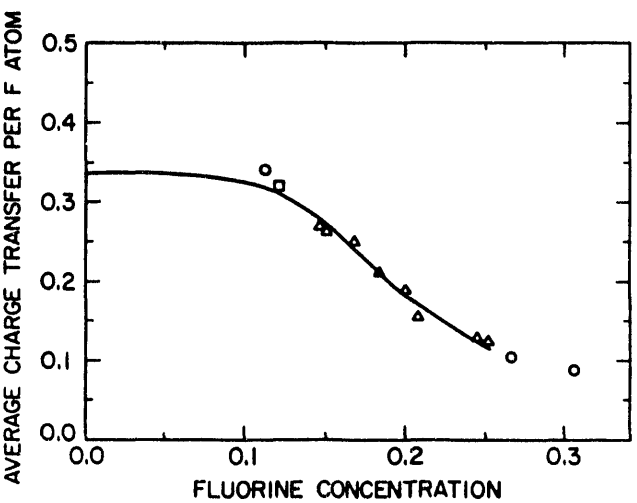

Fig. 4.40. Plot of the charge transfer f_F against $(1/x)$ for stage-2 CF_x, where f_F is the charge transferred to the π band per F atom. The solid line was calculated according to a two-level acceptor state model [4.7]

intercalate and carbon layers. On the basis of a sudden decline in σ_a for decreasing x below $x = 4$, *Ohana* et al. conclude that covalent bonds begin to form first in the stage-1 region.

Brusilovsky et al. [4.136] carried out electrical conductivity (σ_a and σ_c) and optical reflectance studies of the charge transfer in $C_{7-9}BF_x$ (stage 1), $C_{12}BF_x$ (stage 2), and $C_{24}BF_x$ (stage 3), where the B/F ratio is unknown, but presumed to be close to 4. The materials were prepared by the reaction of graphite (HOPG) with a 1:1 mixture of BF_3 and F_2 gas. The reflectance spectra of stage-1 and stage-2 samples were measured over the energy range 0.8–3.2 eV, and the data for the stage-1 and stage-2 compounds were fit to the BR-model dielectric functions to determine values for f_C using $\gamma_0 = 2.9$ eV and $\gamma_1 = 0.38$ eV. From the fits of the BR-model dielectric functions to their data, they obtained the following results: $f_C = 0.032 \pm 0.002$ for $C_{7.3}BF_x$ (stage 1), $f_C = 0.028 \pm 0.220$ for

C_9BF_x (stage 1), and $f_C = 0.027 \pm 0.002$ for $C_{14}BF_x$ (stage 2). Assuming that the only intercalate species is BF_4^-, the charge per intercalate molecule was then determined to be $f_M = 0.23$, 0.25, and 0.39 for the respective compounds. However, later NMR studies by *Davydov* and *Selig* [4.137] reported that this assumption was incorrect. The reported value for the room-temperature in-plane resistivity of the stage-3 compound is $\varrho_a = 4\ \mu\Omega\,\mathrm{cm}$; this suggests that no significant covalent bonding is taking place. However, for stage 1, $\varrho_a = 100\ \mu\Omega\,\mathrm{cm}$, which is quite high, suggesting the formation of a considerable number of covalent bonds.

4.4 Summary and Conclusions

The results reviewed in this chapter indicate clearly that optical methods can be used to study charge transfer in acceptor- and donor-type GICs. We have reviewed both Raman scattering and optical reflectance studies of charge transfer.

In the case of Raman scattering, it has been demonstrated clearly in graphite H_2SO_4 that the frequency of the $\sim 1600\,\mathrm{cm}^{-1}$ graphitic intralayer mode is sensitive to the net charge in the bounding C layers. This result is perhaps expected, since it is known that the in-plane C–C bond length undergoes contraction (expansion) with the removal (addition) of charge from (to) the graphitic carbon layers. However, the mode frequency is also sensitive to the nature of the *c*-axis coupling between the layers of the GIC, and this interlayer coupling is expected to vary from one compound to another.

For graphite-H_2SO_4, the $\sim 1600\,\mathrm{cm}^{-1}$ bounding layer mode upshifts linearly with charge transfer for both stage-1 and stage-2 compounds. However, the results for the rate of change of the mode frequency with increasing charge transfer are stage-dependent – again suggesting that *c*-axis coupling is important. Similar conclusions about charge transfer and mode frequency can be made from the limited data on the infrared-active graphitic intralayer modes. These observations also accord with results from lattice dynamics calculations discussed here.

Of course, it can be argued that a phenomenological correlation between the Raman-active mode frequency $\omega(E_{2gb})$ and charge transfer f_C should nevertheless be attempted. We have considered this correlation – for seven stage-1 acceptor-type GICs: graphite-AsF_5, -$SbCl_5$,-$FeCl_3$,-OsF_6,-MoF_6,-H_2SO_4 ($p = 21, 28$). All the f_C values came from the in-plane plasma frequency using a BR-model analysis with the same value for γ_0. No correlation could be discerned. However, this may in part be due to the small size of the shift in mode frequency, coupled with the experimental uncertainty in the charge transfer $\Delta f_C \sim 10\%$. However, the lack of a correlation may simply indicate the importance of the interlayer coupling on the mode frequency. At the time of writing, it still appears that more theoretical and experimental work is needed before the

graphitic intralayer mode frequencies can be used to obtain reliable values for the charge transfer.

On the other hand, it does seem that reasonable success has been achieved in using optical reflectance and the associated dielectric function to obtain values for the charge transfer. For stage 1, both the H and BR models have been shown to provide a means to obtain f_C from the plasma frequency and the midpoint E_T of the inter-π-band absorption threshold. For stage-2 compounds, the BR model has also been used extensively to obtain f_C from ω_p and E_T.

There still appears to be some uncertainty ($\sim$ 10%) about the appropriate value on the principal tight-binding parameter γ_0 to be used in the BR model, which should be addressed in future work. Most recent work in both donor- and acceptor-type GICs has used values for γ_0 in the range $2.9 < \gamma_0 < 3.0$. For γ_0 in this range, the H model (stage 1) will give answers for f_C similar to the BR model, as long as the charge transfer is not too high. As we have discussed (Sect. 4.3.2a), values for γ_0 can be obtained directly from the experimental plasma frequency in graphite-H_2SO_4, since the charge transfer is known from the electrochemical charge. However, two experimental groups have obtained somewhat different values for γ_0 in the stage-1 compounds – i.e., $\gamma_0 = 2.6$ and 2.9 eV, or a 10% discrepancy. For the case of stage-2 graphite-H_2SO_4, the disagreement in acceptable – i.e., $\gamma_0 = 2.8$ and 2.9 eV, or a 3% discrepancy. The universality of γ_0 should be investigated in several simple donor and acceptor GICs by performing *on the same sample* optical reflectance and at least one other experiment sensitive to charge transfer (i.e., Shubnikov–de Haas, de Haas–van Alphen).

A few optical studies (e.g., of KC_{12n}) have demonstrated that optical structure in the interband contribution to the dielectric function can be used to determine important higher-order band-structure parameters. Further work of this nature might be carried out to determine indirectly, for example, the distribution of net layer charge along the c-axis. Since some of the most conductive GICs are stage $n \geqslant 3$ acceptor compounds, it is both technologically and fundamentally important to develop quantitative band models for these GICs.

Finally, it has been demonstrated that a two-carrier model can be used successfully in understanding the free-carrier optical response in donor GICs. The inter-π-band absorption thresholds seems to provide, via the linking of E_T with f_C, a self-consistent check of the π-electron contribution to the plasma frequency. Further donor GIC optical studies should also strive to collect data from the a face to learn more about the anisotropy of the Fermi surface.

Acknowledgements. It is a pleasure to acknowledge the support of our GIC research at the University of Kentucky by the United States Department of Energy under grant # DE-FGO5-84 ER45151. One of us (P.C.E.) would like to express his sincere appreciation for the many contributions from former students and postdoctoral researchers which have led to his better appreciation of the fundamental issues in the optical properties of GICs. Explicit thanks are therefore due to J.M. Zhang, M.H. Yang, C.H. Olk, D.S. Smith, D.M. Hoffman, and V.R.K. Murthy.

References

4.1 For general recent reviews of the properties of GICs published prior to this two volume series *see* M.S. Dresselhaus, G. Dresselhaus: Adv. Phys. **30**, 139 (1981); S.A. Solin: Adv. Chem. Phys. **49**, 445 (1982)

4.2 S.A. Solin: In *Graphite Intercalation Compounds I*, Topics Curr. Phys., ed. by H. Zabel, S.A. Solin, (Springer, Berlin, Heidelberg 1989); P.C. Eklund: In *Intercalation in Layered Materials*, ed. by M.S. Dresselhaus (Plenum, New York 1986) p. 323; M.S. Dresselhaus, G. Dresselhaus: in *Light Scattering in Solids III*, ed. by M. Cardona, G. Guntherodt (Springer, Berlin, Heidelberg 1982) Chap. 2

4.3 C. Rigaux: In *Intercalation in Layered Materials*, ed. by M.S. Dresselhaus (Plenum, New York 1987) p. 235

4.4 P.C. Eklund, M.H. Yang, G.L. Doll: In *Intercalation in Layered Materials*, ed. by M.S. Dresselhaus (Plenum, New York 1987) p. 257

4.5 V.R.K. Murthy, D.S. Smith, P.C. Eklund: Mater. Sci. Eng. **45**, 77 (1980)

4.6 M.H. Yang, P.A. Charron, R.E. Heinz, P.C. Eklund: Phys. Rev. B **37**, 1711 (1987)

4.7 I. Ohana, I. Palchan, Y. Yacoby, D. Davidov: Phys. Rev. B **38**, 12627 (1988)

4.8 A. Herold: In *Physics and Chemistry of Materials with Layered Structures*, Vol. 6., ed. by F. Levy (Reidel, Dordrecht 1979) p. 323; P.C. Eklund: In *Intercalation in Layered Materials*, ed. by M.S. Dresselhaus (Plenum, New York 1986) p. 163

4.9 A.W. Moore: In *Physics and Chemistry of Carbon*, Vol. 11, ed. by P.L. Walker, P.S. Thrower (Dekker, New York 1973) p. 69

4.10 M. Zanini, J.E. Fisher: Mater. Sci. Eng. **31**, 169 (1977)

4.11 I. Ohana, Y. Yacoby: Phys. Rev. Lett. **57**, 2572 (1986)

4.12 F. Wooten: *Optical Properties of Solids* (Academic, New York 1972)

4.13 J. Blinowski, N.H. Hau, C. Rigaux, J.P. Viren, R. LeToullec, G. Furdin, A. Herold, J. Melin: J. de Phys. **41**, 47 (1980)

4.14 F. Gervais: In *Infrared and Millimeter Waves*, ed. by K.J. Button (Academic, New York 1983) Vol. 8, p. 306

4.15 see p. 244 of Ref. [4.12]

4.16 E.A. Taft, H.R. Phillip: Phys. Rev. **138**, A 197 (1965)

4.17 J.E. Fischer, J.M. Bloch, C.C. Shieh, M.E. Preil, K. Jelley: Phys. Rev. B **31**, 4773 (1985)

4.18 N.A.W. Holzwarth: Phys. Rev B **21**, 3665 (1980)

4.19 L. Johnson, G. Dresselhaus: Phys. Rev. B **7**, 2275 (1973)

4.20 J.M. Zhang, D.M. Hoffman, P.C. Eklund: Phys. Rev. B **34**, 4316 (1986)

4.21 J.M. Zhang, P.C. Eklund, Y.B. Fan, S.A. Solin: Phys. Rev. B **37**, 6226 (1988)

4.22 R. Saito, H. Kamimura: Synth. Met. **12**, 295 (1985); R. Saito: Ph.D. thesis, University of Tokyo (1984)

4.23 T. Ohno, H. Kamimura: J. Phys. Soc. Jpn. **52**, 223 (1983)

4.24 M.H. Yang, P.C. Eklund: Phys. Rev. B **38**, 3505 (1988)

4.25 H. Zabel: In *Graphite Intercalation Intercalaton Compounds I*, ed. by H. Zabel, S.A. Solin, Topics Curr. Phys. (Springer, Berlin, Heidleberg 1989)

4.26 L.J. Brillson, E. Burstein, A.A. Maradudin, T. Stark: In *Physics of Semimetals and Narrow gap Semiconductors*, ed. by D.L. Carter, R.T. Bates (Pergamon, Oxford 1971) p. 187

4.27 C. Underhill, S.Y. Leung, G. Dresselhaus, M.S. Dresselhaus: Solid State Commun: **29**, 769 (1979)

4.28 L. Pietronero, S. Strassler: In *Physics of Intercalation Compounds*, ed. by L. Pietronero, E. Tossati (1981) p. 23.

4.29 C.T. Chan, K.M. Ho, W.A. Kamitakahara: Phys. Rev. B **36**, 3499 (1987)

4.30 J.E. Fischer: In *Graphite Intercalation Compounds- Proc. of Symp. I*, ed. by P.C. Eklund, M.S. Dresselhaus, G. Dresselhaus (Mater. Res. Soc., Pittsburgh 1984) p. 33

4.31 H. Kamimura: In *Graphite Intercalation Compounds- Proc. of Symp. I*, ed. by P.C. Eklund, M.S. Dresselhaus, G. Dresselhaus (Mater Res. Soc., Pittsburgh 1984) p. 36; H. Kamimura: Annales de Phys. **11**, 39 (1986)
4.32 P. Alstrom: Synth. Met. **15**, 311 (1986)
4.33 R. Sonnenschien, M. Hanfland, K. Syassen: Phys. Rev. B **38**, 3152 (1988)
4.34 K. Nogami, H. Ueno, K. Yoshino: J. Appl. Phys. **64**, 6460 (1988)
4.35 T. Inoshito, K. Nakao, H. Kamimura: J. Phys. Soc. Jpn. **43**, 1237 (1977)
4.36 T. Ohno, K. Nakao, H. Kamimura: J. Phys. Soc. Jpn. **47**, 1125 (1979)
4.37 D.D. DiVicenzo, S. Rabii: Phys. Rev B **25**, 4110 (1982)
4.38 T.C. Tatar: Ph.D. thesis, University of Pennsylvania (1985); R.C. Tatar, S. Rabii: in *Graphite Intercalation Compounds- Proc. of Symp. I*, ed. by P.C. Eklund, M.S. Dresselhaus, G. Dresselhaus (Mater. Res. Soc., Pittsburgh 1984) p. 71
4.39 M. Posternak, A. Baldereschi, A.J. Freeman, E. Wimmer, M. Weinert: Phys. Rev. Lett. **50**, 761 (1983)
4.40 M.H. Yang: Ph.D. Thesis, University of Kentucky (1988)
4.41 D. Guerard, G.M.T. Foley, M. Zanini, J.E. Fischer: Nuovo Cimento **38B**, 410 (1977)
4.42 M. Zanini, J.E. Fischer: Mater Sci. Eng. **31**, 169 (1977)
4.43 G.L. Doll, M.H. Yang, P.C. Eklund: Phys. Rev. B **18**, 9790 (1987)
4.44 A. Koma, K. Miki, H. Suematsu, T. Ohno, H. Kamimura: Phys. Rev. B **34** 2434 (1986)
4.45 K. Kume, K. Nomura, Y. Hioryama: Synth. Met. **12**, 307 (1985)
4.46 U. Mizutani, T. Kondow, M. Suganuma: Phys. Rev. B **17**, 3165 (1978)
4.47 M. Suganuma, T. Kondow, U. Mizutani: Phys. Rev. B **23**, 706 (1981)
4.48 M.G. Alexander, D.P. Goshorn, D. Guerard, P. Lagrange, M. El Makrini, D.G. Onn: Solid State Commun. **38**, 103 (1981)
4.49 D.E. Nixon, G.S. Parry: J. Phys. D 201 (1968)
4.50 M. Colin, A. Herold: C.R. Acad. C 269 (1969)
4.51 K. Watanabe, T. Kondow, M. Soma, T. Onishi, K. Tamura: Nature **233**, 160 (1971)
4.52 T. Enoki, H. Inokuchi, M. Sano: Chem. Phys. Lett. **86**, 285 (1982)
4.53 J. Conard, H. Estrade-Szwarckopf, P. Laugins, M. El Makrini, P. Lagrange, D. Guerard: Physica B **105**, 290 (1981)
4.54 S. Kaneiwa, M. Kobayashi, I. Tsuijikawa: J. Phys. Soc. Jpn. **51**, 2375 (1982)
4.55 T. Enoki, M. Sano, H. Inokuchi: Synth. Met. **12**, 207 (1985)
4.56 K. Watanabe, T. Kondow, M. Soma, T. Onishi, K. Tamaru: Proc. R. Soc. London A **333**, 51 (1973)
4.57 G.L. Doll, P.C. Eklund, G. Senatore: In *Intercalation in Layered Materials*, ed. by M.S. Dresselhaus (Plenum, New York 1986) p. 309
4.58 S. Lee, H. Miyazaki, S.D. Mahanti, S.A. Solin: Phys. Rev. Lett. **62**, 3066 (1989)
4.59 T. Kondow, K. Ando, Y. Tomono: In *Physics of Intercalation Compounds*, ed. by L. Pietronero, E. Tosatti (1981) p. 315
4.60 T. Kondow, U. Mizutani: Synth. Met. **6**, 141 (1983)
4.61 T. Kondow, M. Sagawa, T. Takeyama, Y. Tomono, K. Ando, U. Mizutani Synth. Met. **12**, 213 (1985)
4.62 T. Terai, Y. Nonaka, M. Ohira, Y. Takahashi: Synth. Met. **12**, 219 (1985)
4.63 G.L. Doll, P.C. Eklund: J. Mater. Res. **2**, 638 (1987)
4.64 S. Miyajima, T. Chiba, T. Enoki, H. Inokuchi, M. Sano: Phys. Rev. B **37**, 3246 (1988)
4.65 H. Yamamoto, K. Seki, T. Enoki, H. Inokuchi: Solid State Commun. **69**, 425 (1989)
4.66 D. Guerard, C. Takoudjou, F. Rousseaux: Synth. Met. **7**, 43 (1983)
4.67 K.W.-K Shung: Phys. Rev. B **34**, 1264 (1986)
4.68 T. Enoki, N.C. Yeh, S.T. Chen, M.S. Dresselhaus: Phys. Rev. B **33**, 1292 (1986)
4.69 G.L. Doll, P.C. Eklund: Phys. Rev. B **36**, 9191 (1987)
4.70 M. Sano, H. Inokuchi: Chem. Lett., • 4405 (1979)
4.71 F. Beguin, R. Setton, L. Fachini, A.P. Legrend, G. Merle, C. Mai: Synth. Met. **2**, 161 (1980) and references therein
4.72 B.R. York, S.A. Solin: Phys. Rev. B **31** 8206 (1985)

4.73 J.M. Zhang, P.C. Eklund, Y.B. Fan S.A. Solin: Phys. Rev. B. **38**, 10878 (1988)
4.74 H.H. Huang, Y.B. Fan, S.A. Solin, J.M. Zhang, P.C. Eklund, J. Heremans, G.G. Tibbetts: Solid state Commun. **64**, 443 (1987)
4.75 For a general review, see J.C. Thompson: *Electrons in Liquid Ammonia* (Clarendon, Oxford 1976)
4.76 J.M. Zhang, P.C. Eklund, Y.B. Fan, S.A. Solin: Phys. Rev. B **37**, 6226 (1988)
4.77 T. Tsang, R.M. Fronco, H.A. Resing, X.W. Qian, S.A. Solin: Solid State Commun. **62**, 117 (1987)
4.78 X.W. Qian, D.R. Stump, S.A. Solin: Phys. Rev. B **33**, 5756 (1986)
4.79 J.M. Zhang, P.C. Eklund: Synth. Metals **26**, 357 (1988)
4.80 For a general review, see *Electrons in Fluids*, ed. by J. Jortner, N.R. Kestner (Springer, New York 1972)
4.81 M.T. Lok, F.J. Tehan, J.L. Dye: J. Phys. Chem. **76**, 2975 (1972)
4.82 J.L. Dye: In *Electrons in Fluids*, ed. by J. Jortner, N.R. Kestner (Springer, New York 1972) p. 77
4.83 F. Beguin, R. Setton, A. Hamwi, P. Touzain: Mater Sci. Eng. **40**, 167 (1979)
4.84 M.F. Quinton, A.P. Legrand, L. Facchini, F. Beguin: Synth. Met. **14**, 179 (1988)
4.85 M.H. Yang, P.C. Eklund: J. Mater. Res. **1**, 827 (1987)
4.86 M.H. Yang, W.A. Kamitakahara, P.C. Eklund: In *Graphite Intercalation Compounds- Proc. of Symp. I*, ed. by P.C. Eklund, M.S. Dresselhaus, G. Dresse lhaus (Mater. Res. Soc., Pittsburgh 1984) p. 125
4.87 M.H. Yang, P.A. Charron, R.E. Heinz, P.C. Eklund: Phys. Rev. B **37**, 1711 (1988)
4.88 M.E. Preil, J.E. Fischer, P. Lagrange: Solid State Commun. **44**, 357 (1982)
4.89 M.E. Preil, J.E. Fischer: Synth. Metals **8**, 149 (1983)
4.90 R.E. Heinz, P.C. Eklund: Mat. Res. Soc. Symp. Proc. **20** (1983) p. 81
4.91 P. Lagrange, A. Bendriss-Rerhrhaye, J.F. Mareche, E. McRae: Synth. Met. **12**, 201 (1985)
4.92 A. Chaiken: Ph.D. Thesis, Massachusetts Institute of Technology (1986); A. Chaiken, N.C. Yeh, G. Dresselhaus, P. Tedrow: In *Graphite Intercalation Compounds- Proc. of Symp. K*, ed. by M.S. Dresselhaus, G. Dresselhaus, S.A. Solin (Mater. Res. Soc., Pittsburgh 1986) p. 158
4.93 I. Stang, K. Lüders, Z. Geiser, H.J. Güntherodt: Syn. Met. **23** (1988) p. 371
4.94 M.G. Alexander, D. Goshorn, D. Guerard, P. Lagrange, M. El Makrini, D. Onn: Solid State Commun. **38**, 103 (1981)
4.95 Y. Iye, S. Tanuma: Phys. Rev. B **25**, 4583 (1982)
4.96 L.E. DeLong, P.C. Eklund: Synth. Met. **5**, 291 (1983)
4.97 W.E. Spicer: Phys. Rev. Lett. **11**, 243 (1963); F. Wotten, J.P. Hernandez, W.E. Spicer: Appl. Phys. **44**, 1112 (1973)
4.98 S.B. DiCenzo, P.A. Rosenthal, H.J. Kim, J.E. Fischer: Phys. Rev. B **34**, 3620 (1986)
4.99 P.C. Eklund: In *Intercalation in Layered Materials*, ed. by M.S. Dresselhaus (Plenum, New York 1986) p. 337
4.100 S. Aronson, S. Lemont, J. Weiner: Inorg. Chem. **10**, 1296 (1971)
4.101 J.O. Bessenhard, E. Wudy, H. Moewald, J.J. Nickl, W. Biberacher, W. Foag: Synth. Met. **7**, 185 (1983)
4.102 M. St. Jean, M. Menant, N. Hy Hau, C. Rigaux, A. Metrot: Synth. Met. **8**, 189 (1983)
4.103 P.C. Eklund, C.H. Olk, F.J. Holler, J.G. Spolar, E.T. Arakawa: J. Mater . Res. **1**, 361 (1986)
4.104 J.M. Zhang, D.M. Hoffman, P.C. Eklund: Phys. Rev. B **34**, 4316 (1986)
4.105 P.C. Eklund, E.T. Arakawa, J.L. Zarestky, W.A. Kamitakahara, G.D. Mahan: Synth. Met. **12**, 97 (1985)
4.106 W. Kamitakahara, J.L. Zarestky, P.C. Eklund: Synth. Met. **12**, 301 (1985)
4.107 P.C. Eklund, G.D. Mahan, J.G. Spolar, E.T. Arakawa, J.M. Zhang, D.M.Hoffman: Solid. State Commun. **57**, 567 (1986)
4.108 P.C. Eklund, G.D. Mahan, J.G. Spolar, J.M. Zhang, E.T. Arakawa, D.M. Hoffman: Phys. Rev. B **37**, 691 (1988)
4.109 P.A. Giguere, R. Savoie: Can. J. Chem. **38**, 2467 (1960)
4.110 D.M. Hoffman, R.E. Heinz, G.L. Doll, P.C. Eklund: Phys. Rev. B **32**, 1278 (1985)

4.111 D.S. Smith, P.C. Eklund: In *Intercalated Graphite*, Vol. 20 of Symposia Proceedings, ed. by M.S. Dresselhaus, G. Dresselhaus, J.E. Fischer and M.J. Moran (Mater. Res. Soc., Boston 1983) p. 99
4.112 H. Zaleski, P.K. Ummat, W.R. Datars: J. Phys. C **17**, 3167 (1986)
4.113 H. Zaleski, P.K. Ummat, W.R. Datars: Phys. Rev. B **35**, 2958 (1987)
4.114 I. Ohana, D. Vaknin, H. Selig, Y. Yacoby, D. Davidov: Phys. Rev. B **35**, 4522 (1987)
4.115 A.M. Rao, J.M. Zhang, G.W. Lehman, P.C. Eklund: In *Graphite Intercalation Compounds-Proc. of Symp. K*, ed. by M.S. Dresselhaus, G. Dresselhaus, S.A. Solin (Mater. Res. Soc., Pittsburgh 1986) p. 158
4.116 G.M. Gualberto, C. Underhill, S. Y. Leung, G. Dresselhaus: Phys. Rev B **21**, 862 (1980)
4.117 P.C. Eklund, D.S. Smith, V.R.K. Murthy, S.Y. Leung: Synth. Met. 2,99 (1980)
4.118 N. Bartlett, R.N. Biagioni, B.W. McQuillan, A.S. Robertson, A.C. Thompson: J. Chem. Soc., Chem. Commun. **200** (1978)
4.119 L.B. Ebert, D.R. Mills, J.C. Scanlon: Mater. Res. Bull. **18**, 1505, (1983)
4.120 P. Boolchand, W.J. Bresser, D. McDaniel, K. Sisson, V. Yeh, P.C. Eklund: Solid State Commun. **40**, 1049 (1981)
4.121 D. McDaniel, P. Boolchand, W.J. Bresser, P.C. Eklund: In *Intercalated Graphite*, ed. by M.S. Dresselhaus, G. Dresselhaus, J.E. Fisher, M.J. Moran (Elsevier, New York 1983) p. 377
4.122 M.J. Moran, G.R. Miller, R.A. DeMarco, H.A. Resing: J. Phys. Chem. **88**, 1473 (1984)
4.123 D.M. Hwang, X.W. Qian, S.A. Solin: Phys. Rev. Lett. **53**, 1473 (1984)
4.124 P.C. Eklund, D.S. Smith, V.R.K. Murthy: Synth. Met **3**, 111 (1981)
4.125 J. Melin, A. Herold: C. R. Acad. Sci. **269**, 877 (1969)
4.126 M.H. Boca, M.L. Saylors, D.S. Smith, P.C. Eklund: Synth. Met. **6**, 39 (1983)
4.127 G.M.T. Foley, C. Zeller, E.R. Falardeau, F. Vogel: Solid State Commun. **24**, 371 (1977)
4.128 J.E. Fischer: In *Physics and chemistry of Materials with Layered Structures*, ed. by F. Levy, Vol. 6 (Reidel, Dordrecht 1981) p. 481
4.129 L. Fachini, J. Bouat, H. Sfihi, A.P. Legrand, G. Furdin, J. Melin, R. Vangelisti: Synth. Met. **5**, 11 (1982)
4.130 M. St. Jean, N.H. Hau, C. Rigaux, G. Furdin: Solid State Commun. **46**, 55 (1983)
4.131 L.R. Hanlon, E.R. Falardeau, J.E. Fischer: Solid State Commun. 24, 377 (1977)
4.132 B.R. Weinberger, J. Kaufer, A.J. Heeger, J.E. Fischer, M. Moran, N.A. Holzwarth: Phys. Rev. Lett. **41**, 1417 (1978)
4.133 R.M. Markiewicz, H.R. Hart, J.L.V. Interrante, J.S. Kasper: Synth. Met. **2**, 331 (1980)
4.134 G.R. Henning: Prog. Inorg. Chem. **1**, 125 (1959)
4.135 D. Vaknin, D. Davidov, H. Selig, Y. Yeshurun: J. Chem. Phys. **83**, 3859 (1985); D. Vaknin, D. Davidov, H. Selig, V. Zevin, I. Felner, Y. Yeshurun: Phys. Rev. B **31**, 3212 (1985)
4.136 D. Brusilovsky, H. Selig, D. Vaknin, I Ohana, D. Davidov: Synth. Met. **23**, 377 (1988)
4.137 D. Davydov, H. Selig: In *Intercalation in Layered Materials*, ed. by M.S. Dresselhaus (Plenum, New York 1986) p. 433

END

DATE FILMED

12 / 1 / 92